The empact CVT : dynamics and control of an electromechanically actuated CVT

The Empact CVT

Dynamics and Control of an
Electromechanically Actuated CVT

A catalogue record is available from the Library Eindhoven University of Technology

ISBN: 978-90-386-0939-3

This thesis was prepared using the LaTeX documentation system.

Cover design by B. Bonsen.

Printed by Universiteitsdrukkerij, Technische Universiteit Eindhoven.

The Empact CVT

Dynamics and Control of an Electromechanically Actuated CVT

PROEFSCHRIFT

ter verkrijging van de graad van doctor
aan de Technische Universiteit Eindhoven,
op gezag van de Rector Magnificus, prof.dr.ir. C.J. van Duijn,
voor een commissie aangewezen door het College voor Promoties
in het openbaar te verdedigen op
donderdag 12 april 2007 om 16.00 uur

door

Tim Willem Gerard Leo Klaassen

geboren te Nieuw-Bergen

Dit proefschrift is goedgekeurd door de promotor:

prof.dr.ir. M. Steinbuch

Copromotor:

dr.ir. B.G. Vroemen

Preface

The development of the Empact CVT is set in the framework of the SenterNovem BTS (Bedrijfs Technologische Samenwerking) agreement. The aim of the project is to stimulate economic developments in the future by cooperation of companies and universities. This project is a cooperation of the Technische Universiteit (TU/e), Van Doorne's Transmissie (VDT) and the University of Twente (UT). The main goals are the optimization of efficiency, durability and torque transmission capacity of metal V-belt type CVTs. To achieve these goals, the project initially focussed on the optimization of the pushbelt and the variator. Preliminary studies, however, showed that the actuation system of the variator has significant impact on the total efficiency of the CVT. Therefore, this subject was subsequently added to the project. The focus points and research topics of the project are

1. to maximize efficiency and durability of the variator by applying variator slip measurement and control techniques (TU/e)

2. to optimize maximal transmittable torque and durability of the pushbelt by developing and using new materials that combine high yield strength with good fatigue resistance (VDT)

3. to optimize durability of the variator and pushbelt by developing a failure mode model and wear prediction model for the boundary lubrication contact (UT)

4. to maximize efficiency of the variator by developing an alternative actuation system (TU/e)

The work in this thesis is mainly part of the fourth topic, but combines this with and contributes to the development of slip control techniques (topic 1).
The project is carried out by three ph.d. students, ir. K.G.O. van de Meerakker, dr.ir. B. Bonsen, who received his ph.d. dissertation "Efficiency optimization of the push-belt CVT by variator slip control" in December 2006 and ir. T.W.G.L.

Klaassen, under supervision of prof.dr.ir. M. Steinbuch, dr. P.A. Veenhuizen and dr.ir. B.G. Vroemen.

Contents

Preface **v**

1 Introduction **1**
1.1 CVT drivelines . . . 1
1.2 CVT efficiency . . . 6
1.3 CVT driveline control . . . 9
1.4 Problem description and main contributions . . . 13
1.5 Outline of the thesis . . . 14

2 The Empact CVT **15**
2.1 System description . . . 15
2.2 Potential of the Empact CVT . . . 18
2.2.1 Actuation power . . . 18
2.2.2 Efficiency . . . 23

3 Modeling **27**
3.1 Test rig components . . . 27
3.1.1 Torque converter . . . 28
3.1.2 DNR set . . . 28
3.1.3 Final drive reduction . . . 29
3.1.4 Shafts and couplings . . . 29
3.2 Variator . . . 29
3.2.1 Geometry and definitions . . . 30
3.2.2 Clamping force model . . . 31
3.2.3 Torque transmission . . . 35
3.2.4 Transient variator model . . . 37
3.3 Empact actuation system . . . 38
3.3.1 Kinematics . . . 40
3.4 Friction models . . . 41

3.5 Validation results 42

4 Control problem formulation **47**
4.1 System description 48
4.2 Performance specification and system requirements 49
4.3 Control architecture 52
4.4 Design limitations 54

5 Control oriented identification **55**
5.1 Identification experiment design 56
5.2 Approximate realization using pulse responses 58
5.3 Closed loop identification procedure 62
5.4 Closed loop identification results 63
5.4.1 $1^{\mathbf{st}}$ identification step results 64
5.4.2 $2^{\mathbf{nd}}$ identification step results 70
5.4.3 $3^{\mathbf{rd}}$ identification step results 73
5.5 Interaction analysis 75

6 Control design and evaluation **81**
6.1 Control designs 82
6.1.1 Manually loop-shaped decentralized controller 82
6.1.2 $\mathcal{H}_\infty$ loop-shaped decentralized controller 82
6.1.3 $\mathcal{H}_\infty$ MIMO controller 84
6.2 Gain scheduling 86
6.3 Controller switching strategy 87
6.4 Closed loop performance evaluation 90
6.4.1 Simulation evaluation 90
6.4.2 Experimental evaluation 93

7 Experimental performance evaluation **101**
7.1 Ratio reference 102
7.2 Slip reference 103
7.3 Empact FTP72 cycle performance 105
7.4 Audi A3 implementation and performance 107

8 Conclusions and recommendations **113**
8.1 Conclusions 114
8.2 Recommendations 117

A Measurement setup **119**
A.1 Empact prototypes 119
A.2 Test rig measurement setup 123
A.3 Audi A3 and chassis dyno measurement setup 124

B Capita selecta **127**
B.1 Pulley thrust ratio 127
B.2 Slip dynamics 128
B.3 Inverse response of slip during ratio changes 128
B.4 Linear system analysis 129

Nomenclature **143**

Summary **147**

Samenvatting **151**

Dankwoord **155**

Curriculum Vitae **157**

Chapter 1

Introduction

The main objective of the research described in this thesis is to achieve optimal operation of an electromechanically actuated metal V-belt type CVT. This system is referred to as the ElectroMechanical Pulley Actuation (EMPAct) Continuously Variable Transmission (CVT). The electromechanical actuation system replaces the conventional hydraulic actuation system used in nowadays metal V-belt type CVTs. The system aims for a fuel saving of 10 [%] compared to hydraulic actuation systems. The mechanical design of the Empact CVT is covered by Van de Meerakker [99]. The focus of the present thesis is the modeling, dynamical analysis, control design and experimental evaluation – on a test rig as well as in a test vehicle – of the Empact CVT.
This chapter first gives an overview of CVT drivelines in Section 1.1. Section 1.2 presents the driveline and CVT efficiency in more detail. An overview of driveline and CVT control is given in Section 1.3. This more general introduction forms a basis for the problem description in Section 1.4. The outline of this thesis is presented in Section 1.5.

1.1 CVT drivelines

CVTs are increasingly used in automotive applications. Their advantages over classical automatic and manual transmissions are their large ratio coverage and the absence of comfort issues related to shifting events as occur in automatic transmissions. Because the engine speed can be chosen independently of the vehicle speed, efficient operating points of the internal combustion engine can be used that are unreachable with a manual or a stepped automatic transmission. The large ratio coverage further enables the engine to operate at more fuel economic operating points, making the vehicle potentially more fuel efficient. Unfortunately, because the energy dissipation of the CVT itself is higher than that of a manual transmission,

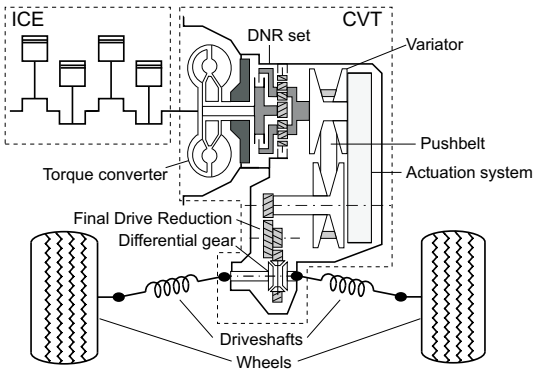

Figure 1.1: Driveline Components

this efficiency improvement is partly lost. Before going into detail on these power losses and on how to improve the efficiency (Section 1.2), an overview of the CVT driveline components is given. The CVT will be discussed in the form in which it is used the most, *i.e.* transversely mounted in a front wheel driven car. The driveline, schematically depicted in Figure 1.1, basically contains an internal combustion engine (ICE), a CVT, driveshafts and wheels. At the input or engine side, the transmission is loaded by the engine torque. In a medium-size car, the maximum engine torque is typically between 150 and 250 [Nm]. Engine torque changes can be highly dynamic, from no load to maximum torque in half a crankshaft rotation. At the output side, the transmission is loaded by the torque in the driveshafts. Apart from the reaction torque up to 2500 [Nm] that is generated by the final drive, this torque also incorporates disturbances from the interaction between the tires and the road, such as torque peaks resulting from driving up a curbstone, abruptly braking or spinning the wheels (μ-split events) or other events occurring in the road-wheel contact. The ICE, driveshafts and wheels are beyond the scope of this thesis and will not be further described here. The CVT itself, described in the next subsections, consists of a variator including a V-belt, an actuation system, a launching device, a drive-neutral-reverse set and a final drive reduction.

Variator

The variator forms the heart of the CVT and consists of a segmented steel V-belt and two shafts with conical pulleys. The belt is clamped between two pairs of conical sheaves. In the variator, the transmission ratio is determined by simultaneous adjustment of the running radii of the belt on the pulleys. On each shaft, there is one fixed and one axially moveable sheave. Axial movement of the moveable sheave adjusts the gap between the sheaves and thereby the belt running radius. The input shaft of the variator is called the primary shaft, the output shaft is the secondary shaft. In Figure 1.2 the working principle of the variator is illustrated. In this figure the shifting process from the low ratio to the overdrive ratio is shown.

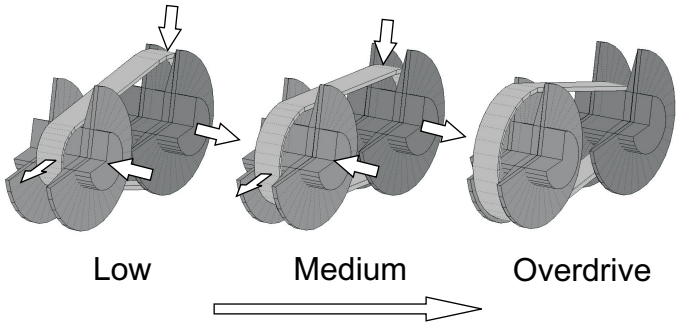

Figure 1.2: The working principle of the V-belt type variator illustrated by the shifting process from low ratio to overdrive ratio.

Launching device

A CVT needs a separate device for launching. Often a torque converter (TC) with lock-up clutch is used for this purpose. After vehicle launch, the TC can be locked by engaging the lock-up clutch. It then forms a fixed connection between the engine and the input shaft of the transmission. These components and their models are described in more detail by Serrarens [87], Lechner *et al.* [58] and Bertsche *et al.* [7].

Drive-Neutral-Reverse set

To enable forward or reverse driving or to set the driveline in neutral, the CVT contains a Drive-Neutral-Reverse (DNR) set. The input shaft of the DNR set is connected to the output shaft of the TC, whereas the output shaft of the DNR set is directly connected to the primary pulley of the CVT. The DNR consists of a planetary gear set and two wet plate clutches. The clutches can either couple the planet carrier to the transmission housing (Reverse) or the ring gear to the planet carrier (Drive). If none of the clutches is engaged, the transmission is in neutral.

Final drive reduction

The secondary shaft of the variator is connected to the differential gear via a final reduction gear and an intermediate shaft. The differential gear distributes the torque between the two driveshafts and decouples their speeds. The reduction gear on the secondary shaft of the CVT, the intermediate shaft and the differential gear together form the Final Drive Reduction (FDR).

Actuation system

To adjust the transmission ratio and to be able to transmit torque in the variator, one sheave of each pulley is actuated axially. Early CVTs used a mechanical actuation system [24], with a passive control of clamping force and ratio. Since the driveability and efficiency were very poor, hydraulic systems were developed. The advantages of

Figure 1.3: Dry belt CVT as produced by Aichi Kikai [95]

hydraulic actuation systems are a high power density and the possibility to actively control the variator. In these systems, the speed ratio can be chosen independent of the vehicle speed. In most CVTs, such as the Jatco CK2 [1], the oil pump used to provide the hydraulic power is directly coupled to the crankshaft of the ICE. For a hybrid vehicle application, a CVT with electro-hydraulic actuation was developed [15]. Since the ICE is occasionally shut down in hybrid vehicles, it can not be used to continuously provide the required hydraulic power, hence an electric motor is required to drive the oil pump. Recently, attention has been given to electromechanical systems. Aichi Kikai [95], [116] developed such a system for dry belts. The Empact CVT is an electromechanically actuated CVT for pulley type CVTs [100].

Belt types

The development of the V-belt type CVT began with rubber V-belts [24]. Despite the fact that rubber V-belt CVTs are not well suited for automotive applications because of their limited torque capacity, there are some interesting concepts on the market. An example of a dry rubber belt CVT is the Bando Avance system [95], depicted in Figure 1.3. Dry rubber belts are of interest because a much higher friction coefficient is established between belt and pulleys than in lubricated variants. A dry belt CVT therefore needs less clamping force and can be much smaller and lighter. This is interesting for low power applications, such as motorcycles and small cars.
For increasing torque capacities, Van Doorne Transmissie [108] developed a metal V-belt, also referred to as the pushbelt. This type of belt consists of blocks and bands as shown in Figure 1.4(a). The blocks can transmit torque when they are under compression, hence the name pushbelt. The bands, normally two sets of between nine and twelve bands each, hold the blocks together. The bending stiffness of the bands is very small and may be neglected, such that only a tension force will be present in the bands. The compressive forces in the blocks can never exceed

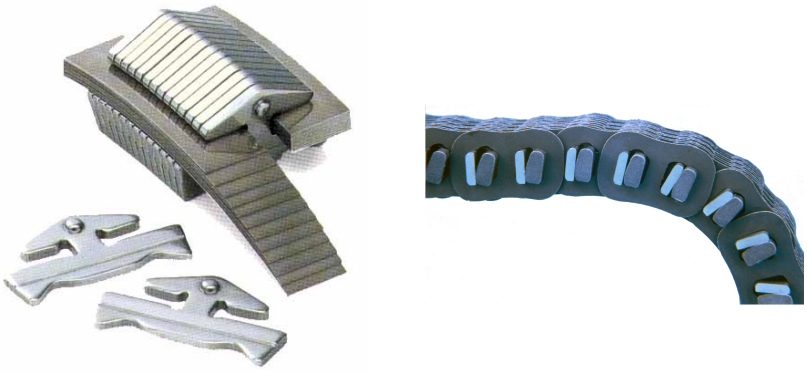

(a) A VDT metal pushing V-belt

(b) A GCI CVT chain

Figure 1.4: Lubricated belt types

the tension forces in the bands, since otherwise buckling of the pushbelt would occur. Because the bands and the blocks do not run exactly at the same radius, a speed difference is present between the blocks and the bands. This results in friction losses in the pushbelt, which lowers the efficiency. Because of the continuous bending and stretching of the bands, fatigue issues are important. Fatigue resistance specifications limit the maximum forces in the pushbelt, resulting in a limitation of the torque capacity of the variator.

A third type of element used to transmit power in a variator is the chain. CVT chains as developed by LuK [64] or GCI [107] consist of pins and segments. The pins are typically curved to enhance the chain-pulley contact. Figure 1.4(b) gives a picture of the GCI CVT chain. Like the LuK chain, this chain uses two sets of pins per link. This enables the chain to transmit the tension force by rolling and static contacts only, *i.e.* no sliding occurs within the chain. The pins need to rotate in order to change the shape of the chain. When compressed between the pulley sheaves, this will cause a counteracting friction between the pulley and the pins. The GCI chain minimizes this friction by slightly shortening one pin. Compared to pushbelts, these chains have very little internal friction, thereby increasing the efficiency, especially for low input torques. Due to the relatively small number of pins that continuously run into the pulley, chains produce typically more noise than pushbelts. LuK partly overcomes this problem by varying the length of the links, such that the noise power is spread over a wider frequency band, thereby reducing the amplitude [41]. GCI claims that their chain causes less noise than the LuK chain, because of the eliminated rotation of the pins under load. Due to the relatively small number of pins compared to the number of blocks in a pushbelt, the forces acting on the pins are relatively large, causing the pins to wear more easily.

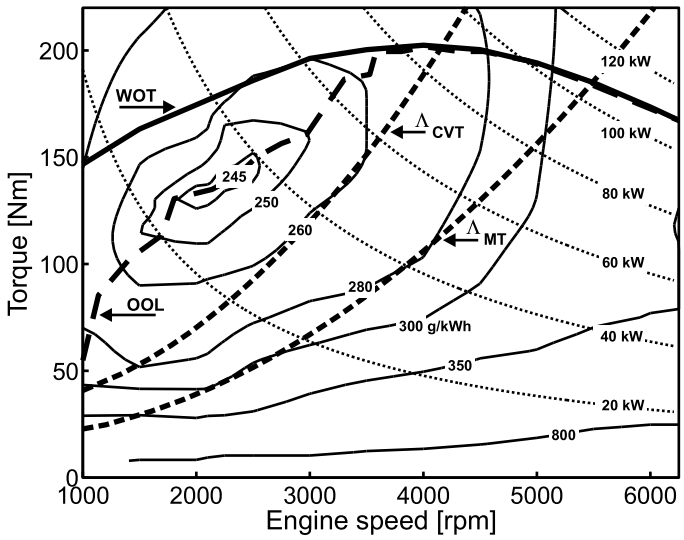

Figure 1.5: Fuel consumption map of an Audi A3 2.0 FSI engine, Wide Open Throttle (WOT) line (—), Optimal Operating Line (OOL) (– –), maximum gear ratio stationary driving resistance curves Λ_{CVT} and Λ_{MT} (- -) and power curves (:)

1.2 CVT efficiency

The large ratio coverage of a CVT and the possibility to choose the engine speed independently of the vehicle speed enables the ICE to operate at more fuel economic operating points, making the vehicle potentially more fuel efficient. Figure 1.5 shows the fuel consumption map of an Audi A3 2.0 FSI engine [4]. In this figure the Wide Open Throttle (WOT) and the Optimal Operating Line (OOL) are shown. The OOL connects the most fuel efficient operating points of the ICE for each engine speed and is also referred to as the E-line. Furthermore, the curves Λ_{CVT} and Λ_{MT} represent stationary driving under normal vehicle load, *i.e* tire rolling resistance and air drag, using the maximum transmission gear for a CVT based driveline and a manual transmission (MT) based driveline respectively. These lines indicate the limit of the fuel efficiency for stationary driving [79]. As can be seen, due to the larger ratio coverage, the ICE operates closer to the OOL for a CVT than for a MT based driveline. During transient behavior, the ICE can be operated even closer to the OOL using a CVT, thereby optimizing the driveline efficiency.
Figure 1.6 shows the energy flow for a typical car driving at 120 [km/h] for a CVT and a MT based driveline. The useable power output to the wheels in the CVT driveline does not differ very much from the output of the manual transmission driveline [75]. The distribution of power losses is nevertheless different. In the CVT driveline, the engine will have an efficiency of approximately 38 [%], whereas in the MT driveline this efficiency is close to 30 [%]. Unfortunately, because the energy dissipation of the CVT (≈11 [%]) itself is higher than that of a manual transmission (≈3 [%]), this efficiency improvement is lost. The main reason for the low efficiency

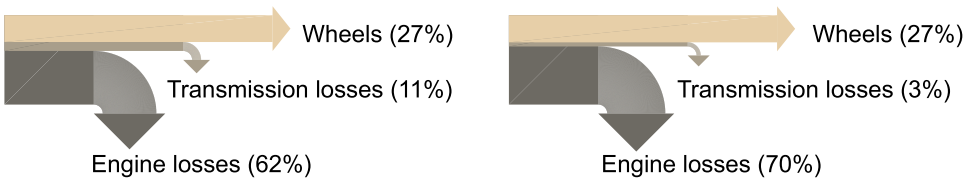

(a) Energy flow in a CVT Driveline (b) Energy flow in a MT Driveline

Figure 1.6: Typical energy flows in different drivelines for a typical car at 120 [km/h]

of these CVTs is the high clamping force applied to transfer the engine torque. To prevent belt slip at all times, the clamping forces in modern production CVTs are usually much higher (at least 30 [%] or more) than required for normal operation, *i.e.* without disturbances. Higher clamping forces result in higher losses in both the hydraulic and the mechanical system, *i.e.* increased pump losses and increased friction losses because of the extra mechanical load that is applied on all variator parts.

Excessive clamping forces also reduce the durability of the belt since the force is larger than strictly needed for the transfer of the engine power. Also the contact pressure between V-belt and sheaves is higher than strictly needed, leading to increased wear. Furthermore, this excessive loading leads to heavier components, thereby compromising power density.

To improve the fuel economy of CVT equipped vehicles, the optimization of the CVT efficiency shows to have the largest potential. The main losses in the CVT are the mechanical and actuation system losses. In Figure 1.7(a) the flow of engine output power in a typical CVT is shown when driving at constant moderate speed. It can be seen that the main losses are due to the variator and the hydraulic actuation system [39]. Other losses are due to the TC, DNR set and FDR. In this analysis, the TC lock-up clutch is assumed to be closed. Unlocked torque converters have in general a very limited efficiency. The TC lock-up clutch as well as the clutches in the DNR set are usually of the wet-plate type.

In [10] and [103] it is shown that it is possible to reduce the actuation losses by means of controlling the slip in the variator. Using a slip control strategy, the clamping forces are reduced to minimal values, directly reducing the power losses of the hydraulic system. Furthermore, the losses in the variator are reduced [71]. Efficiency gains of more than 10 [%] can be reached compared to conventional clamping force strategies. This efficiency optimization is shown in Figure 1.7(b). However, the hydraulic actuation system still requires a significant amount of power. To reduce these hydraulic losses, Bradley and Frank [15], [90] present an alternative hydraulic system with servo-pumps for ratio and clamping force control. This system achieves approximately 5 [%] fuel consumption reduction compared to a conventional hy-

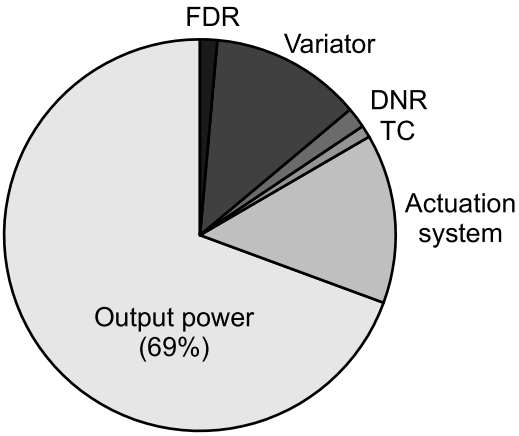

(a) Conventional hydraulically actuated metal V-belt CVT

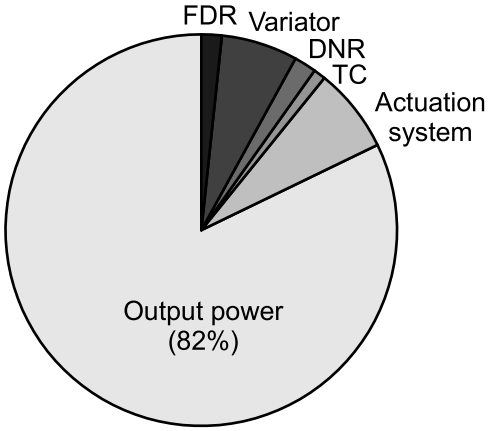

(b) Metal V-belt CVT with minimal clamping forces

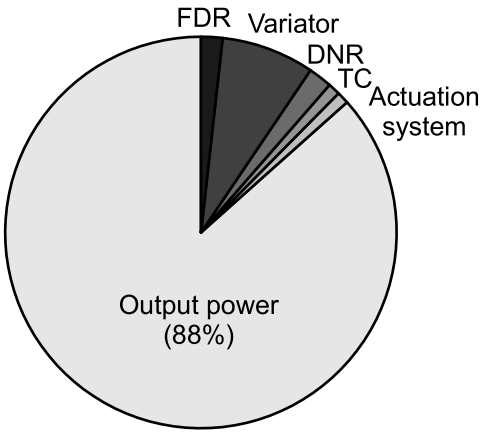

(c) Metal V-belt CVT with minimal clamping forces and optimized actuation system

Figure 1.7: Flow of engine output power in a CVT at partial load

draulic system. Also Faust *et al.* [25] show that it is possible to achieve significant fuel savings based on an optimized hydraulic system. A major disadvantage of these hydraulic actuation systems is that the compressibility of the oil increases with decreasing pressure. As a consequence, the required bandwidth for both ratio and clamping force control can not be realized. Especially, slip control at low pressures requires a stiff actuation system to prevent excessive slip in the variator.
Yuki *et al.* [116] developed an electromechanical actuation system to reduce the actuation losses. Although this leads to a relatively stiff system, the system has the disadvantage that the clamping force is supported by a thrust bearing between the rotating shaft and the transmission housing, which leads to large power losses in these bearings. This limits the use of this system to low power applications, with low clamping forces. The Empact CVT (Figure 2.1 and Figure 2.2), as proposed by Van de Meerakker *et al.* [101], uses a double epicyclic gear at each shaft with thrust bearings between the two sun gears to support the clamping force. The speeds of these sun gears only differ during ratio changes. In this way, the power losses in the thrust bearings are reduced significantly and the clamping device can be used for high power applications. Because of the high stiffness of the actuation system, even at low clamping forces, the Empact CVT is very suitable for slip control. In this way the power losses during steady state can be reduced to a minimum by applying minimal clamping forces. Figure 1.7(c) shows the resulting power chart when an optimized actuation system is used. The efficiency can be increased with more than 15 [%] compared to the conventional hydraulically actuated CVT.

1.3 CVT driveline control

The control and/or steering strategies for engine and transmission are mostly referred to as *coordinated* driveline control or *integrated* driveline control [87]. The objective for coordinated driveline control is often an weighted optimum of fuel economy and driveability. The control of local components, *e.g.* the ICE and the CVT, is referred to as driveline *component* control [111]. The objective for component control is to optimally control the component and track the references trajectories prescribed by the coordinated controller. Additional requirements can be imposed on the component controllers, *e.g.* actuator power limitations and damage or fail-safe control.

Coordinated driveline control

In Figure 1.8 the total system hierarchy is depicted. The driver tries to control the vehicle speed by manipulating the drive pedal and brake. The power strategy translates the pedal position into a desired engine power. The tuning of this strategy depends on the desired driveability, comfort and performance of the vehicle. In modern CVT based vehicles, often two or three pre-tuned strategies can be selected

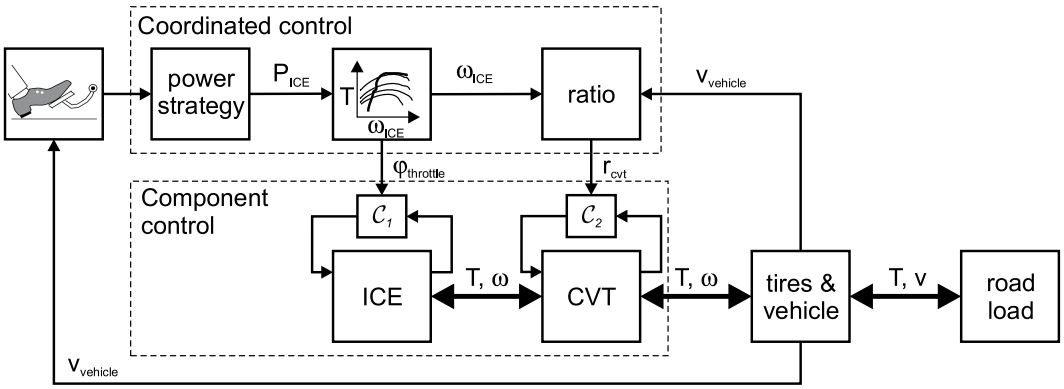

Figure 1.8: Driveline control

by the driver, *e.g.* economic and sportive driving. The desired engine power is translated into a desired throttle position and engine speed. Using the actual vehicle speed, the ratio reference is determined. The mapping from throttle position to ratio reference is often referred to as the variogram. Several approaches to realize an optimal operating strategy are discussed in literature [87], [19], [23], [13], [98], [62], three of them are introduced below.

To achieve optimal ICE efficiency, the *single track strategy* [19], for which the operating points are all located on the Optimal Operation Line (OOL) (see Figure 1.5), can be used. For most modern combustion engines the OOL is at relatively low engine speeds and high engine torques. An increase of power can only be realized by increasing the engine speed, since the engine torque is near its maximum. This has a negative effect on the driveability.

A second strategy is the *speed envelope strategy* [23], in which for a fixed vehicle speed, the engine speed is chosen almost linear to the driver input. In transient conditions, the engine torque is addressed for immediate response, followed quickly by a CVT ratio change that generates the engine acceleration corresponding to the driver input. The available torque reserve improves the driveability compared to the single track strategy. Once the driver input reaches a certain level, a seemingly steady state engine torque is reached and maintained by continuous engine speed modulation. A modification of the speed envelope strategy is presented by Bonsen *et al.* [13]. For an increase of driveability, they introduce a velocity dependent engine setpoint.

In the *off the beaten track strategy* [98], the driver input is correlated with the demand for engine power. Here, the engine and transmission control cooperate to find an optimal throttle position and CVT ratio, such that the engine operation is close to the OOL. Although with this control strategy a certain torque reserve can be addressed for immediate response, driveability could be effected, because the engine response is not directly related to the drivers input.

Driveability

A driveability study is not part of this thesis. However, for deriving the control objectives it is briefly investigated. More details can be found in [73] and [87].
Driveability is partly coupled to the chosen operating strategy, however it depends on many additional variables. Driveability is a subjective parameter, but can be correlated with objective variables. A definition for driveability is given by [84]: *"The term driveability describes the drivers complex subjective perception of the interactions between the driver and vehicle."*
The expectations for driveability vary from person to person. Perception varies with gender, age and cultural background [84]. An example is the perception of driveability according to American, European and Japanese drivers:

- for American drivers cruise and comfort are important,
- for European drivers perception is based on tip in, acceleration and gear shift,
- for Japanese drivers vibrations when idling or at other frequencies are important

The perception also varies with time and with technological possibilities. Before electronic controllers were introduced in automotive vehicles the driveability was determined by ignition, fueling and gear ratio. Nowadays, the driveability can be influenced by the engine and transmission controllers.
A more objective definition of driveability is given by [112]: *"Driveability is related to the perception of the vehicle's longitudinal response to a change in demand by the driver during transient vehicle operation."*
Several criteria have been defined to objectively describe driveability, such as acceleration, pedal response, pedal to torque relation, precise gear shift, consistent starts, uniformity of rotation, noise, hesitations, jerks, kicks, stumble, oscillations, surge, overshoot, undershoot, torque vibrations, etcetera. Criteria that are most important for the shift quality of automatic transmissions are [29], [86]:

- vehicle acceleration,
- noise,
- vehicle response,
- shifting frequency,
- peak to peak acceleration amplitude,
- peak to peak jerk variation,
- maximum average power,
- the 10-14 Hz frequency content of the longitudinal acceleration after a step input at the accelerator pedal.

For CVTs, 'shifting frequency' is only of importance when a stepped transmission is simulated. Experimentally achieved subjective driveability aspects for CVTs are given by [22]:

- the vehicle response to a pedal movement has to occur immediately after the driver has actuated the accelerator pedal,
- the vehicle acceleration should be a function of the vehicle speed,
- a correlation between the engine speed and the vehicle speed should be established and this correlation should vary for different manoeuvres,
- drivers do not wish the vehicle to creep when stopped.

CVT component control

The objective of the CVT control is to track the ratio reference, prescribed by the coordinated driveline controller. An additional requirement for the CVT component controller is to prevent the belt from slipping excessively.
Early hydraulically actuated metal V-belt CVTs used a mechanical feedback control system [81]. In these systems, the ratio control was carried out by controlling the oil flow to and from the primary pulley using feedback of the CVT speed ratio. Belt-pulley slippage was prevented in a passive manner by restricting the exhaust oil flow, such that a residual pressure was maintained. These systems had limited flexibility and the ratio strategy was mainly based on the performance limitations of this system.
Most modern hydraulically actuated CVTs use a pressure control system. The desired speed ratio is obtained by controlling the ratio between the pressure at the secondary pulley and the pressure at the primary pulley. For this purpose mechanical feedback devices are used, *e.g.* in the Jatco CK2 CVT [1], as well as electronically controlled devices. The clamping force, necessary to prevent belt-pulley slippage, is actively controlled using the magnitude of the hydraulic pressure. Mostly the pressure at the secondary pulley is controlled, because the clamping force at this pulley is lower than the clamping force at the primary pulley for most operating points where slip might occur [9] and is therefore most critical. In most control systems, the minimally required pressure to transmit a certain engine torque is estimated using a steady-state variator model. A certain safety margin is then added to the pressure to prevent belt slippage. A commonly used safety strategy is to multiply the minimally required pressure by a safety factor, which is typically between 1.3 and 1.5. For low input torques an absolute safety margin is used, large enough to suppress torque disturbances up to 30 or 50 [Nm].
A disadvantage of this safety strategy is that higher clamping forces decrease the variator efficiency and increase the required actuation power (see Section 1.2). As fuel economy becomes more and more important, the development of optimized control strategies such as slip control [9] and the robustness of the variator under macro slip conditions [103] have recently been given much attention. The aim of these strategies is to control the pressure with a safety margin close to zero, or to directly control the slip in the CVT.

1.4 Problem description and main contributions

The main goal of the project carried out at the TU/e is the optimization of the efficiency of pulley type CVTs. The main sources of power loss in conventional hydraulically actuated V-belt type CVTs are the actuation system and the variator. The actuation system losses are mainly caused by the excess oil flow from the hydraulic unit and the oil leakage from the hydraulic cylinders in the variator, even during steady-state operation of the CVT. The development of the Empact CVT aims at minimizing these steady-state losses by replacing the hydraulic system by an electromechanical system. This system however, introduces additional mechanical power losses due to friction and electrical power losses due to operation of the electric motors. These losses all depend on the forces required to operate the system, *i.e.* the clamping forces necessary to prevent the belt slippage. The power losses in the variator are also mainly caused by the clamping forces used to prevent slip between the belt and the pulleys at all times. From this problem description, the basic hypothesis of this thesis can be formulated as:

> **Electromechanical actuation systems can increase the efficiency of metal V-belt CVTs, while maintaining functionality specifications.**

To evaluate this hypothesis, the performance of the Empact CVT is compared to the performance of a reference transmission. The chosen reference transmission is the Jatco CK2 transmission. Both steady-state and transient performance are important in this evaluation. The mechanical design of the Empact CVT, covered by Van de Meerakker [99], focusses on the optimization of the systems efficiency, while maintaining the same functionality specification as the CK2. The main objectives of the research presented in this thesis are to

- gain insight in the behavior of the Empact CVT by developing simulation models and by performing experiments,
- achieve optimal efficiency of the Empact CVT for steady-state and transient operation,
- track the CVT ratio reference signal, prescribed by the coordinated driveline controller,
- prevent the pushbelt from slipping excessively under all driving conditions,
- experimentally validate the above objectives.

This thesis aims to contribute to the research and development of fuel economic drivelines. It will be shown that electromechanical pulley actuation increases the efficiency of the CVT significantly. Therefore, insight in the efficiency of hydraulically and electromechanically actuated CVTs is developed and it is shown how to benefit from the efficiency potential of electromechanical actuation systems. The thesis furthermore contributes to the development of models for CVTs and CVT drivelines,

which combine steady-state and transient operation. A significant contribution to variator slip control research and development is made, since this control approach is relatively new. This thesis also aims to contribute to the field of control and identification, by combining identification results from complex, nonlinear models and experimentally obtained data into simple control-oriented models that describe the relevant local dynamic behavior in order to design low order controllers for both the nonlinear model and experimental setup.

1.5 Outline of the thesis

Chapter 2 first gives a functional description of the Empact CVT. The potential of this system compared to the CK2 reference transmission is then studied, using models and measurements of the efficiency during steady-state operation and power consumption during transient behavior.
In Chapter 3, a dynamical model of the Empact CVT and the test rig is made. The model incorporates a dynamical description of all major components of the test setup, including an extensive model of the variator and of the friction losses in the Empact CVT. This model is validated using experimentally obtained data.
Chapter 4 presents the control problem formulation. A description of the system from a control point of view is given. Furthermore, the control performance specification and additional requirements for the control system are discussed. This leads to a choice for the control architecture. Also, limitations for closed loop performance are discussed.
Chapter 5 introduces a method to obtain suitable models for control design. This method is applied to the nonlinear model as presented in Chapter 3. The identification is carried out in a closed loop environment. The control oriented models are validated using experimentally obtained data. Finally, it is shown that the choice for control architecture as presented in Chapter 4 is justified.
Chapter 6 deals with the design of the controller, including switching strategies. The tracking performance and disturbance rejection will be evaluated using simulation and experimental results.
Chapter 7 presents the experimental evaluation of the Empact CVT at the test rig and implemented in an Audi A3 2.0 FSI with respect to power losses and efficiency.
Finally, in Chapter 8 conclusions are drawn and directions for further research are given.

Chapter 2

The Empact CVT

The Empact CVT is based on the Jatco CK2 transmission [1]. The redesign of this transmission is restricted to the actuation system, variator shafts and transmission housing. The torque converter, DNR set, final reduction, intermediate shaft and differential gear are not modified. Also typical variator dimensions, such as pulley wedge angle, minimum and maximum pulley radius and the center distance between the input and output shaft, are unchanged.
Section 2.1 gives a functional description of the actuation system and of the experimental setup used to test the system. A more detailed description of the mechanics is given in [99], [100] and [101]. In Section 2.2 the potential of the Empact CVT regarding efficiency and performance is investigated using measurement results from this test setup.

2.1 System description

The Empact CVT uses two servomotors to actuate the moveable pulley sheaves. To decouple the rotation of the input and output shaft from the servomotor rotations, a double epicyclic set is used at each shaft. An important characteristic of these double sets is that the carriers at each shaft are combined and that the dimensions of all four epicyclic sets are equal. Figure 2.1 shows a concept drawing of the Empact CVT, whereas Figure 2.2 gives a more schematic representation.
At the primary (input) shaft, one sun gear is fixed to the pulley shaft. The other sun gear can rotate around the centerline of the shaft. This latter sun gear is connected to the planetary spindle nut. The concentric spindle bush is integrated with the moveable pulley sheave. This pulley sheave can translate axially, but not rotate with respect to the fixed pulley sheave. The planet gears of both the epicyclic gear sets are supported on needle bearings on a common carrier. One ring gear of the double epicyclic set is fixed to the transmission housing to prevent its rotation. The

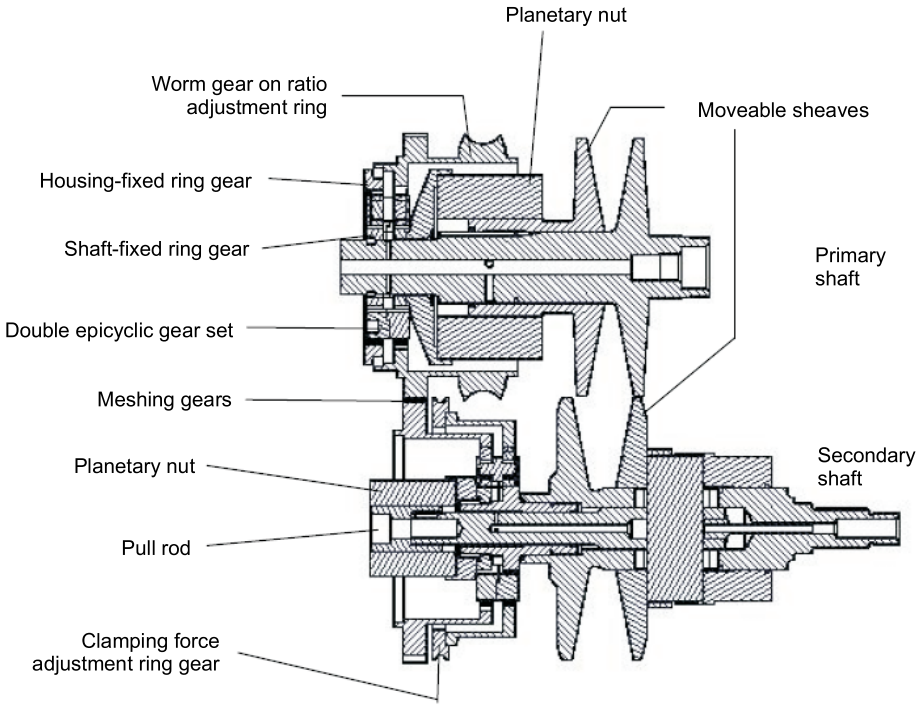

Figure 2.1: Concept drawing of the Empact CVT

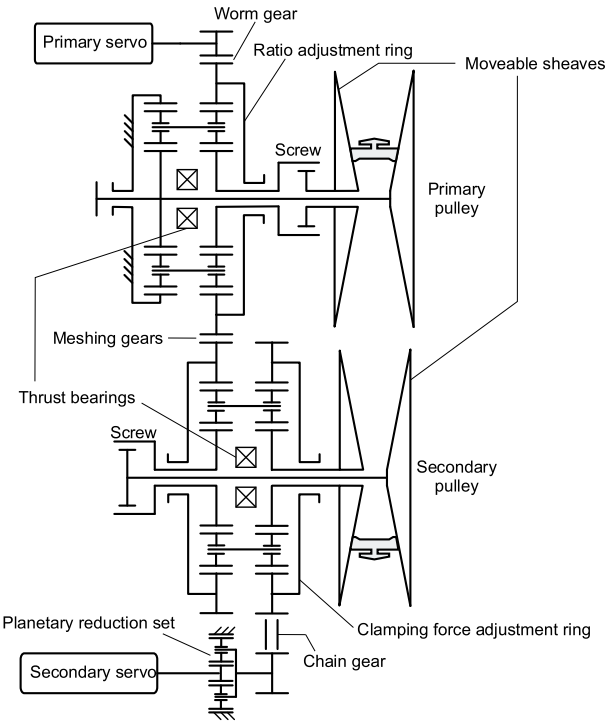

Figure 2.2: Schematic representation of Empact CVT

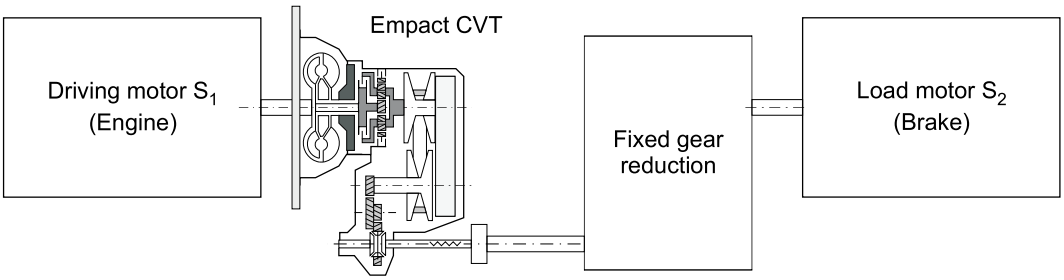

Figure 2.3: Empact test setup (schematic)

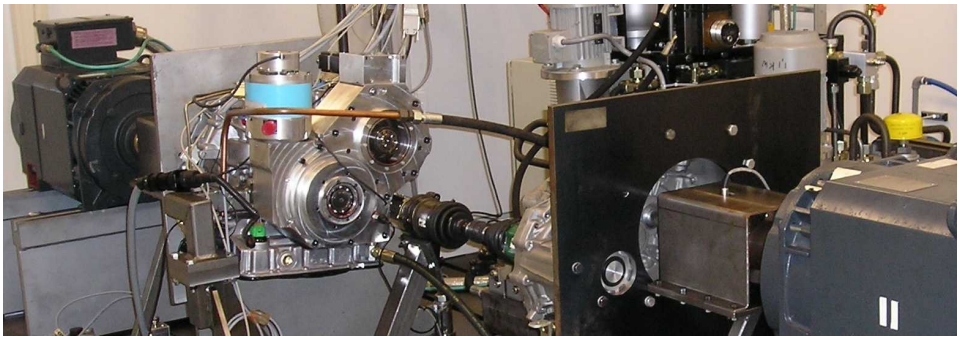

Figure 2.4: Empact test rig

other ring gear, the so-called ratio adjustment ring, is actuated by the primary servo M_p. This servo is connected by a worm to the worm gear on the ratio adjustment ring. If the adjustment ring gear is not rotating, the shaft-fixed sun gear and the sun gear at the planetary nut have the same speed, thereby maintaining the pulley position. If the adjustment ring gear is rotated relative to the transmission housing, a rotation difference between the sun gears is established and the spindle axially moves the moveable pulley sheave.

At the secondary (output) shaft, a similar mechanism is used to adjust the secondary moveable sheave position. One ring gear of the double epicyclic set at this shaft directly meshes with the primary ratio adjustment ring. As a result, by rotating the primary servo M_p, both moveable sheaves will make the same translation, resulting in a CVT ratio change. However, as will be explained in Chapter 3, due to different wrapped angles of the belt at the primary and secondary pulley, the axial displacement of the opposite moveable sheaves is in the same direction, but not of exactly the same magnitude. Therefore, the second ring gear at the secondary shaft is not fixed to the transmission housing, but is connected to the secondary servomotor M_s by a chain transmission and an additional planetary reduction. By applying a torque by the secondary servo, the ring gear will rotate slightly during ratio change and will thereby compensate for the moveable sheave translation difference. Furthermore, the clamping forces in the variator can be controlled by adjusting the torque delivered by the secondary servomotor.

The double epicyclic sets enable the clamping force to be supported by a thrust

bearing between the two sun gears at each shaft. Because the velocities of these sun gears only differ during ratio changes, no power is lost in steady state operation. Furthermore, due to the meshing of the ring gear at the primary with the one at the secondary shaft, energy can be transferred from the primary moveable pulley sheave to the secondary moveable pulley sheave, and vice versa. This energy exchange significantly reduces the required actuation power of the primary and secondary servomotor.

For functional testing of the Empact CVT, a prototype (P1) is built with two (oversized) high voltage brushless DC servomotors. Based on the results, obtained with this prototype, a second, optimized prototype (P2) is built, which will be implemented in a car. In this prototype, the primary actuator M_p is a brushed type DC servo, whereas the secondary actuator M_s is a brushless type servo. Both servomotors operate at 56 [V]. The transmission ratio of the planetary reduction at the secondary actuator is different for both prototypes. Details of both systems are given in Appendix A. The results shown in the next section are obtained with the first prototype.

The test setup, shown in Figure 2.3 and Figure 2.4, consists of a driving motor S_1, a torque converter (TC), the Empact CVT including final drive reduction (FDR), a fixed gear reduction (GB) and a load motor S_2. The output shaft of the CVT is connected to the fixed gear reduction by a single driveshaft. The differential gear of the CVT is mechanically locked, so all power can be directed to this driveshaft. The fixed gear reduction is used to match the load motor characteristics to the driving motor characteristics. A complete description of the measurement setup is given in Appendix A.

2.2 Potential of the Empact CVT

To reduce the overall power losses, the Empact CVT addresses two loss sources in the CVT, being the power losses in the actuation system and the power losses in the variator, *i.e.* in the pushbelt and in the bearings of the input and output shaft. Without going into the details of the required advanced control system, this section shows the potential of the Empact CVT regarding the reduction of these losses. The controller for the Empact is described in Chapter 5. The control specifications of the CK2 transmission are thoroughly described in [9].

2.2.1 Actuation power

This section gives a comparison between the actuation power in the original CK2 transmission and the Empact CVT. The minimally required mechanical power to move the pulley sheaves in the CK2 and in the Empact CVT is given by

$$P_{act,min} = F_{act,p}\dot{x}_p - F_{act,s}\dot{x}_s \tag{2.1}$$

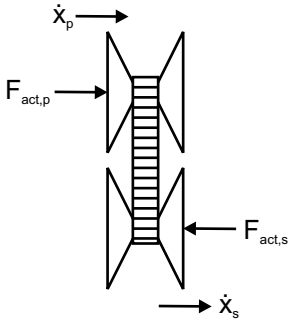

Figure 2.5: Sign convention of clamping forces and velocities in the variator

where $F_{act,p}$ and $F_{act,s}$ are the primary and secondary actuation forces and $\dot{x}_p$ and $\dot{x}_s$ are the speeds of the primary and secondary moveable sheaves. Sign conventions as shown in Figure 2.5 are used. In the CK2 with the hydraulic actuation system, the actuation forces can be calculated directly from the pressures in the primary and secondary cylinder, p_p and p_s, corrected for centrifugal forces [111], [9].
The relation for the actual power used in the actuation system of both transmissions, *i.e.* the consumed power including all actuation losses, are derived below.

Empact

The actuation power in the Empact CVT, delivered by the primary and secondary servo, is given by

$$P_{act,Empact} = P_{mp} + P_{ms} \tag{2.2}$$

where P_{mp} and P_{ms} are the powers delivered by the primary and secondary servo respectively. This servo power can be separated into a mechanical and electrical part, according to

$$P_{mp} = P_{mp,mech} + P_{mp,elec} = \omega_{mp} T_{mp} + \left(\frac{T_{mp}}{k_{mp}}\right)^2 R_{mp} \tag{2.3}$$

$$P_{ms} = P_{ms,mech} + P_{ms,elec} = \omega_{ms} T_{ms} + \left(\frac{T_{ms}}{k_{ms}}\right)^2 R_{ms} \tag{2.4}$$

where ω_{mp} and ω_{ms} are the angular velocities of the primary and secondary servo, T_{mp} and T_{ms} are the output torques of the primary and secondary servo, k_{mp} and k_{ms} are the servo torque constants and R_{mp} and R_{ms} are the servo terminal resistances. $P_{mp,mech}$ and $P_{ms,mech}$ are the mechanical powers delivered by the servos to actuate the system, whereas $P_{mp,elec}$ and $P_{ms,elec}$ are the electrical power losses in the servos. This electrical power losses is influenced by the choice of servomotors. The servo amplifiers dissipate an additional 25 [W], which has to be taken into account.
To operate the accessories that require hydraulic power, *i.e.* the torque converter, DNR clutches and lubrication circuit, an external electrohydraulic oil pump is used in the Empact CVT. The power P_{acc} consumed by this pump can be estimated from

the torque and velocity, using a similar relationship as given in (2.3). Measurements show that a constant power of 120 [W] is sufficient, for all operating modes of the torque converter. A battery efficiency of 90 [%] is taken into account in this estimation.
The choice of the servomotors influence the total power consumed in the Empact CVT. From (2.3) and (2.4) it can be seen that the lower the torque constant of the servo, the higher the dissipated energy in the servo windings.

CK2

In the CK2 transmission, the clamping forces are realized by a hydraulic system. The oil pump, which provides the required flow and pressure, is directly connected to the crankshaft of the internal combustion engine. This constant volume internal gear type pump has an output flow of 16 [cc/rev]. The line pressure is controlled by a valve, actuated by a linear solenoid. The pressure ranges between 6 and 42 [bar]. The accessories that use hydraulic power operate at 6 [bar]. Oil flow, not needed for actuation of the pulleys or the accessories, is led directly to the sump. Hence, even in stationary situations, there is a constant power loss in the actuation system. The total power consumed in the actuation system of the CK2, including losses, can be expressed as

$$P_{act,CK2} \quad = \quad \omega_e \; p_{line,CK2} \; c_{pump,CK2} - P_{acc} \tag{2.5}$$

where ω_e is the engine velocity, $p_{line,CK2}$ is the line pressure, $c_{pump,CK2}$ is the flow per rotation constant and P_{acc} is the power required to operate the accessories equal to P_{acc} measured at the Empact.
The test setup used for experimental evaluation of the CK2 is described in Appendix A.

Results

Figure 2.6 shows results from shifting experiments from low (LOW) to overdrive (OD) for different constant references for the primary sheave speed $\dot{x}_p$. Experiments were performed at a secondary clamping force $F_{act,p}$ of approximately 10 [kN] and a primary shaft speed ω_p of 150 [rad/s]. Figure 2.6(a) shows the Empact CVT servo power P_{mp} and P_{ms} in the two lower plots. It can be seen that in stationary situations, *i.e.* where no shifting occurs, both actuators require very little power.
Figure 2.6(b) shows $P_{act,CK2}$ in the middle plot. Here it can be noticed that even in stationary situation over 250 [W] is consumed. Note that this stationary power loss increases approximately linearly with clamping forces (see 2.5). The minimal required actuation power $P_{act,min}$ during this experiment is shown in the lower plot. As the reference for $\dot{x}_p$ is constant, it can be concluded that the ratio controller of the Empact system performs significantly better than that of the CK2. This is

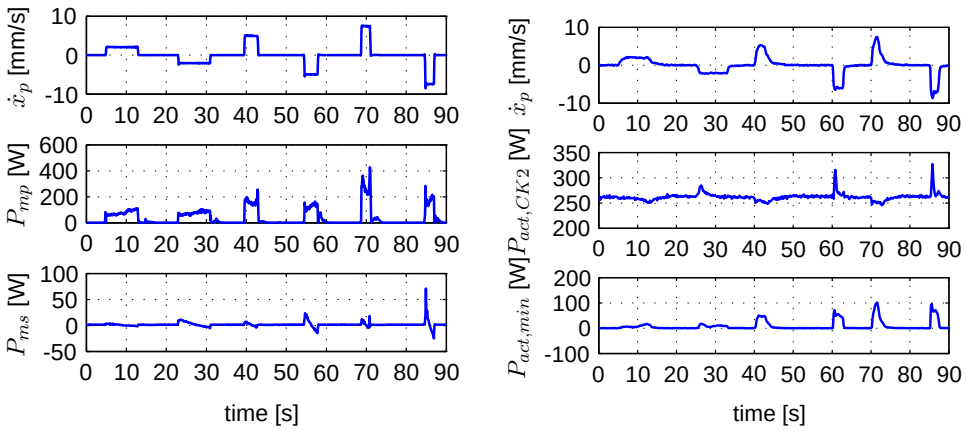

(a) Empact (b) CK2

Figure 2.6: Up- and downshifting experiment from LOW to OD ratio

mainly due to the low stiffness of the CK2 actuation system at low line pressures. Figure 2.7(a) shows the results for $\dot{x}_p$ ranging from -9 to 9 [mm/s]. Pulley speeds measured at the CK2 do not exceed 7.5 [mm/s], which is the maximum for the applied line pressure. Higher maximum pulley speeds require higher line pressures, resulting in higher $P_{act,CK2}$. It can be seen that $P_{act,Empact}$ increases approximately linearly with pulley speed and is about twice the minimal required power, which indicates an overall actuation system efficiency of ± 50 [%].

Figure 2.7(b) shows that the primary actuator delivers the largest part of the power. The secondary actuator power is even negative in some situations, which indicates that this servo generates energy. This generator effect only occurs when shifting from medium (MED) towards LOW or overdrive (OD). Here, the secondary actuator velocity $\dot{x}_s$ is negative and a positive T_{ms} must be applied to obtain the required clamping force in the system. With the current electrical system layout, the servomotors can not be used as generators and the possible recovered power must therefore be neglected.

Figure 2.7(c) shows that the electric power loss P_{elec} is relatively small compared to the mechanically useful power P_{mech}. To illustrate the additional losses when servomotors with lower torque constants are used, Figure 2.7(d) shows $P_{act,Empact}$ for both prototypes P1 and P2. It can be seen that the extra electrical power, needed for prototype P2, is less than 75 [W].

It is furthermore mentioned, that practical values of $\dot{x}_p$ for comfortable shifting of the CVT are between -5 [mm/s] and 5 [mm/s] for normal driving. Especially in this region, the Empact CVT outperforms the CK2 CVT.

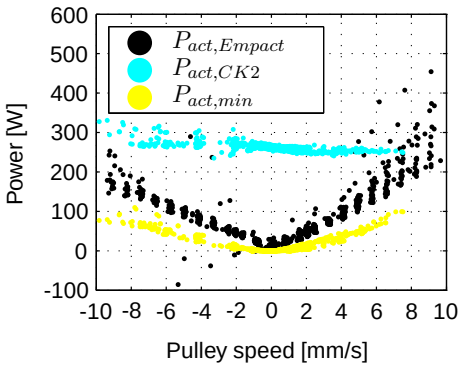

(a) Empact vs. CK2

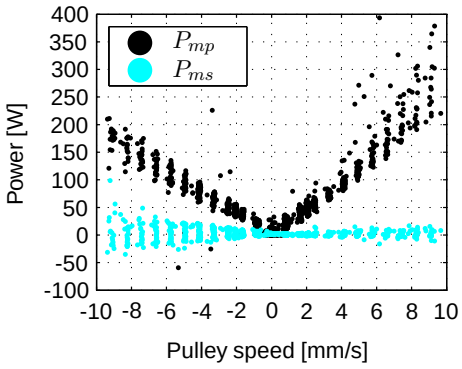

(b) Primary vs. Secondary

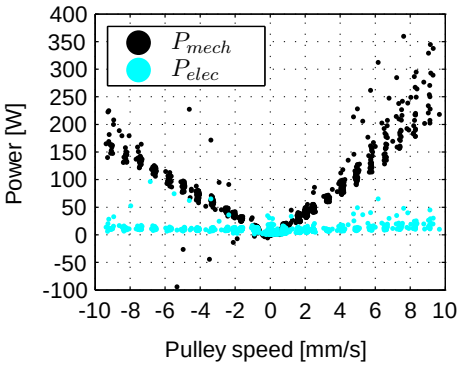

(c) Mechanical vs. Electrical

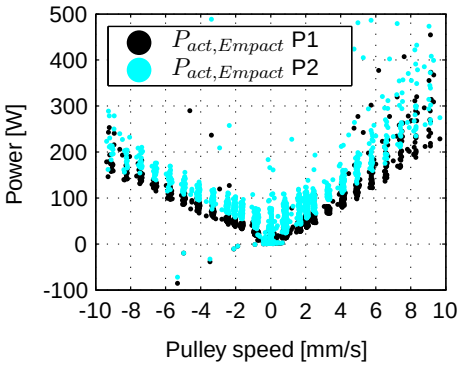

(d) P1 vs. P2

Figure 2.7: Actuation power

2.2.2 Efficiency

To be able to compare the efficiency of the CK2 transmission and of the Empact (P1), both systems are measured at the same test rig, with an identical measurement equipment (see Appendix A). At this test rig, the transmission input power P_{in} and output power P_{out} can be estimated using measurements of the primary shaft speed ω_p, the secondary shaft speed ω_s, the input torque T_p and the driveshaft torque T_d, according to

$$P_{in} = T_p\ \omega_p \tag{2.6}$$

$$P_{out} = T_d\ \omega_s i_{FDR} \tag{2.7}$$

where i_{FDR} is the final drive reduction ratio. Note that the power losses of the TC, DNR and FDR are incorporated here. Because these components are identical in both transmissions, this does not affect the comparison.

Empact

With the input and output power and the power losses described in the previous subsection, the efficiency of the Empact η_{Empact} can be estimated using

$$\eta_{Empact} = \frac{P_{out}}{P_{in}\ + P_{act,Empact} + P_{acc}} \tag{2.8}$$

CK2

In the CK2 transmission, the actuation power and the power required for the accessories are delivered by the driving motor. Hence, measurement of the input and output power directly results in the CK2 efficiency η_{CK2}, according to

$$\eta_{CK2} = \frac{P_{out}}{P_{in}} \tag{2.9}$$

Results

The efficiency of a CVT is a function of the CVT ratio, the input torque T_p and the clamping forces. Optimal efficiency is achieved around the maximum torque $T_{p,max}$ that can be transferred at a given clamping force. Bonsen [9] shows that by controlling the slip in the variator, this optimal efficiency can be approached.
Figure 2.8 shows the efficiency for both transmissions, measured in LOW, MED and OD. The left figures show the results from measurements at a constant force $F_s \approx 10$ [kN], which is the minimum secondary clamping force in the CK2. This clamping force can not be measured directly in the Empact. Therefore, the torque T_{ms} of the secondary servo is adjusted until this 10 [kN] is justified by applying T_{ms} such that the maximum input torque equals the $T_{p,max}$ of the CK2 at $F_s = 10$ [kN], obviously at the same ratio. It can be seen that in this case the Empact system performs

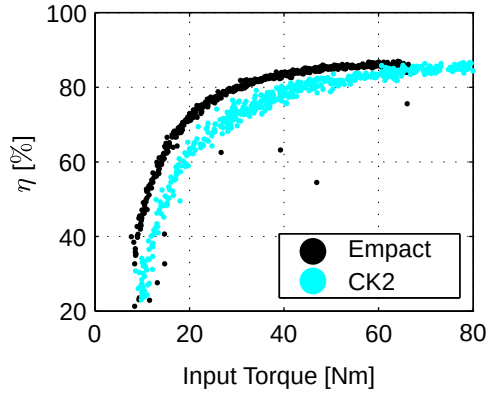

(a) LOW at $F_s = 10$ kN

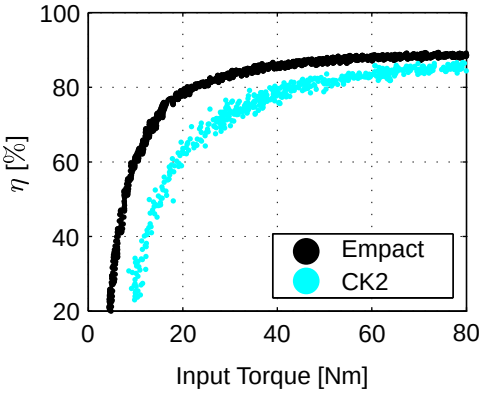

(b) LOW with slip control

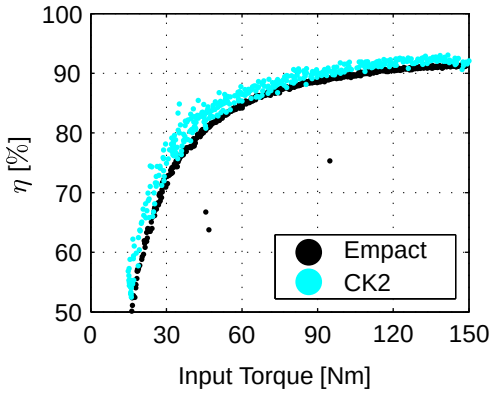

(c) MED at $F_s = 10$ kN

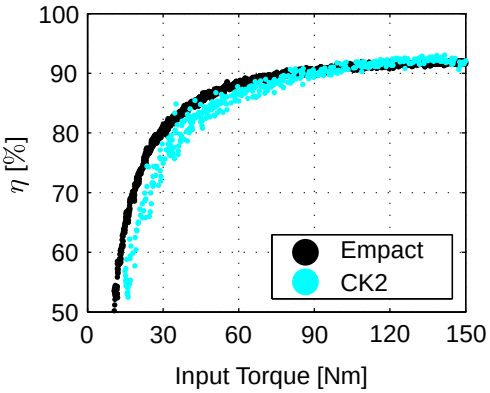

(d) MED with slip control

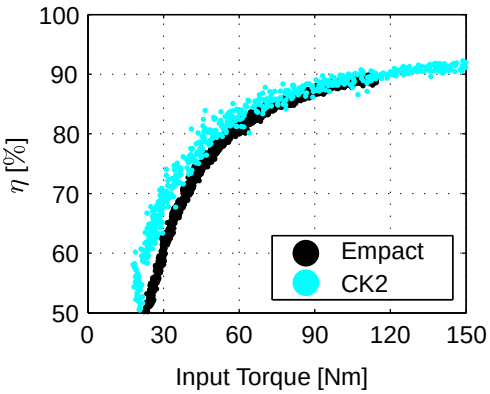

(e) OD at $F_s = 10$ kN

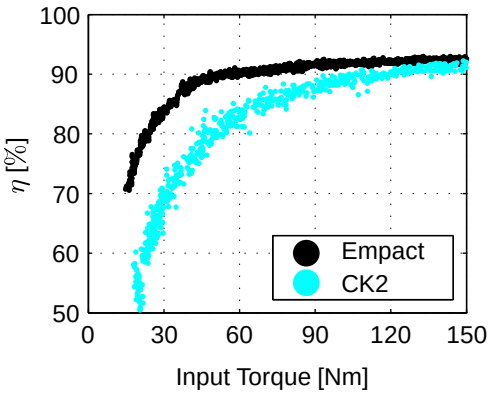

(f) OD with slip control

Figure 2.8: Efficiency of the Empact and CK2 transmission

slightly better than the CK2 in LOW and that the efficiency is similar in MED and lower in OD. This effect is most likely caused by the friction at the secondary shaft of the Empact CVT, specifically in the epicyclic sets. It is emphasized that the efficiency in at $F_s = 10$ [kN] is the optimal efficiency that can be achieved with a CK2 transmission.

The strength of the Empact system is that the clamping forces can be reduced to minimal values while maintaining a high actuation stiffness and, hence, a good controllability of ratio and slip. The right figures in Figure 2.8 show the measured efficiency when the slip in the variator is controlled, such that optimal efficiency is reached. It can be seen that then the Empact outperforms the CK2 in all ratios. In overdrive at input torques up to 80 [Nm], which is the case for over 75 [%] in the FTP72 cycle and for over 90 [%] in the NEDC cycle, an efficiency gain of up to 15 [%] can be reached. This higher efficiency could also be reached with a different hydraulic actuation system which allows lower pressures (like presented in [90]). However, these hydraulic systems have the inherent property that the oil compressibility increases with decreasing pressure, thereby reducing controllability of both ratio and slip in the CVT.

Chapter 3

Modeling

This chapter describes the model of the Empact CVT and the test rig to validate this model. In the construction development phase, the Empact CVT model was used to specify the layout of the actuation system, to analyze the forces and torques in the system and to evaluate its performance [52], [53]. The purpose of the model in this thesis, however, is to provide a basis for control design and to yield a realistic description of the closed loop system. Therefore, the model incorporates a dynamical description of all major components of the test setup, including an extensive model of the friction losses in the Empact CVT [50], [48].
The variator and the actuation system are thoroughly described in Section 3.2 and 3.3 respectively. Section 3.1 first presents an overview of all other driveline components. Friction models are described in Section 3.4. Finally, Section 3.5 gives experimental validation results.
As will be shown in Chapter 4, the desired ratio and slip control bandwidth is 10 [Hz]. To incorporate all behavior, significant for control design, the dynamics are described up to 100 [Hz]. Natural frequencies above this frequency are not relevant for the control design model

3.1 Test rig components

The test rig is schematically shown in Figure 3.1. The core of the test rig is the Empact CVT, which comprises the electromechanical actuation system, the variator, the torque converter, the DNR set, the final reduction and the differential gear. The output shaft of the CVT is connected to a gearbox (GB), which is necessary to match the driving motor characteristics to the load motor characteristics.

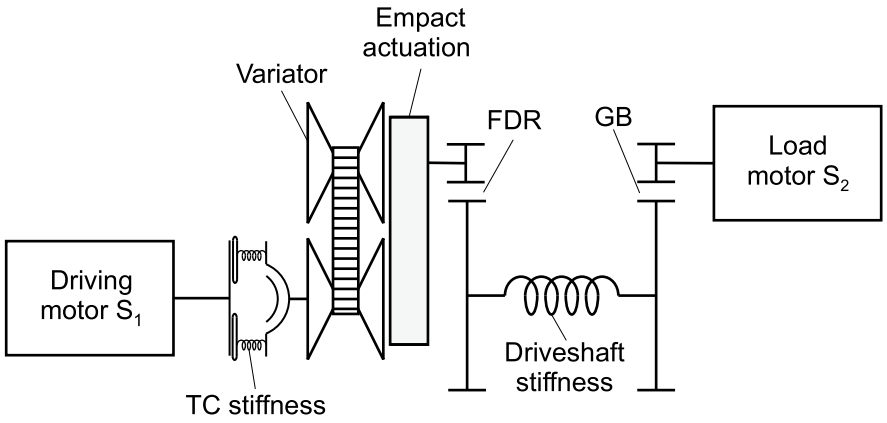

Figure 3.1: Empact test rig model

3.1.1 Torque converter

The Empact CVT uses a torque converter (TC) as launching device. This device decouples the combustion engine from the transmission at low vehicle speeds. At higher speeds, a lockup clutch can be engaged, such that the input of the TC is mechanically connected to the output. The efficiency of the TC is increased significantly if the lockup clutch is closed.
When the lockup clutch of the TC is opened, the output torque $T_{tc,out}$ is given by

$$T_{tc,out} = \alpha_{tc}(r_{tc}) b_{tc}(r_{tc}) \omega_{tc,in}^2 \quad ; \quad r_{tc} = \frac{\omega_{tc,out}}{\omega_{tc,in}} \tag{3.1}$$

where α_{tc} is the torque amplification factor, b_{tc} is the torque capacity factor, r_{tc} is the TC speed ratio and $\omega_{tc,in}$ and $\omega_{tc,out}$ the TC input and output speeds.
Isolator springs with total stiffness k_{tc} are embodied in the lockup clutch to smoothen torque peaks that might occur during lockup engagement. In the lockup mode this device can be modeled as a parallel combination of a torsional spring with stiffness k_{tc} and a linear viscous torsional damper with damper constant c_{tc} [97], [94], [87]. The damping constant c_{tc} can be derived from torque amplification characteristics of the TC for small perturbations around the locked position. Inertia effects of the torque converter can be partly incorporated in the ICE inertia and partly in the primary shaft of the CVT.
In the experimental setup an electric motor is used to propel the driveline and no decoupling is necessary. Therefore, during the experiments and simulations, the torque converter is used in lockup mode only.

3.1.2 DNR set

In the experimental setup the DNR set is exclusively used in Drive mode, meaning that the input and output shaft are mechanically connected by the drive clutch. The slip in this clutch may be neglected, therefore only the inertias of this set are incorporated in the simulation model.

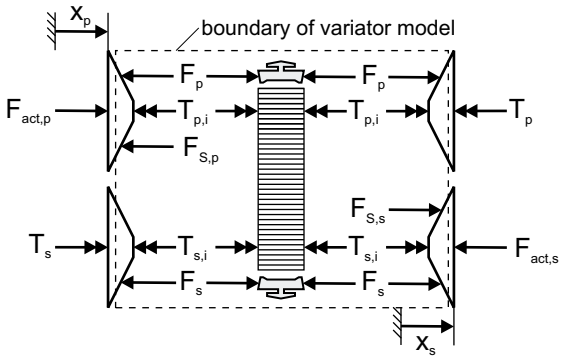

Figure 3.2: Schematic representation of the variator model

3.1.3 Final drive reduction

In the experimental setup the differential gear is mechanically locked in order to transmit the power to a single driveshaft. The FDR can then be modeled as a single reduction with ratio i_{FDR}. The inertia of the FDR is taken into account.

3.1.4 Shafts and couplings

The torque sensor between the driving motor and the TC and the torque sensor between the GB and the load motor S_2 are connected to the shafts using backlash free, torsionally stiff steel lamina couplings ($k > 5 \cdot 10^5$ [Nm/rad]). The combined stiffness of these shafts and couplings at both sides are relatively high compared to the TC and driveshaft stiffness. Therefore, the connection between the driving motor and the TC, as well as the connection between the gearbox and the load motor are considered to be rigid.
Finally, the driveshaft between the FDR and the GB is relatively flexible and is therefore modeled as a torsional spring with stiffness constant k_d.

3.2 Variator

The variator consists of two pairs of conical sheaves and a pushbelt. The purpose of the variator model in the overall model is to describe the coupling between the primary and the secondary variator shaft by means of the transmitted belt torque, to estimate the clamping forces in the variator and to model the transient behavior of the variator. The inertias effects of the pulleys are incorporated in the model of the actuation system.
Figure 3.2 shows a schematic representation of the variator model. The boundary of the model is depicted by the dashed box. The geometric relations are presented in Section 3.2.1. The torques, exerted by the pushbelt at the primary and secondary pulley, $T_{p,i}$ and $T_{s,i}$, are described in Section 3.2.3 using a characteristic property of the variator, *i.e.* the slip dependent traction of the variator. A distinction is made

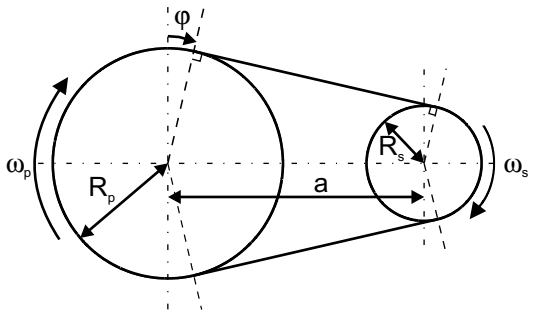

Figure 3.3: Variator geometry

between the clamping forces F_p and F_s and the actuation forces $F_{act,p}$ and $F_{act,s}$. The clamping forces are exerted on the pulley sheaves by the belt and are therefore part of the variator model. The actuation forces are exerted on the pulley sheaves by the actuation system and are not described by the variator model. Section 3.2.2 focusses on the estimation of the clamping forces. Transient behavior of the variator is described in Section 3.2.4.

3.2.1 Geometry and definitions

The geometric ratio r_g and the speed ratio r_s of the variator are defined by

$$r_g = \frac{R_p}{R_s} \tag{3.2}$$

$$r_s = \frac{\omega_s}{\omega_p} \tag{3.3}$$

Here R_p and R_s represent the running radius of the belt on the primary, respectively secondary pulley. It is assumed that the path of the belt on each of these pulleys is a part of a circle. The speeds of the pulleys at the contact line of the pulleys and the belt is given by

$$v_p = R_p\omega_p \tag{3.4}$$

$$v_s = R_s\omega_s \tag{3.5}$$

Variations of the belt speed v_{belt} along the belt are small enough to be neglected. In Section 3.2.3 it will be shown that when a non-zero torque is transmitted, always a certain slip occurs between the belt and at least one of the pulleys, *i.e.* that $v_{belt} - R_p\omega_p \neq 0$ and/or $v_{belt} - R_s\omega_s \neq 0$. It is assumed that, in stationary conditions, slip only occurs on the pulley with the smallest spanned arc, so $v_{belt} - R_p\omega_p = 0$ if $R_p > R_s$, whereas $v_{belt} - R_s\omega_s = 0$ if $R_s > R_p$. The relative slip ν is defined by

$$\nu = \frac{v}{v_p} = \frac{R_p\omega_p - R_s\omega_s}{R_p\omega_p} = 1 - \frac{r_s}{r_g} \tag{3.6}$$

This quantity shows to be convenient when describing the traction in the variator, although this definition of slip is only useful for $r_g \neq 0$ and $\omega_p \neq 0$. At these low

input speeds, the slip dynamics will become infinitely fast. In Appendix B.2, this problem is further analyzed.
Figure 3.3 depicts the variator geometry. If spiral running is neglected, *i.e.* the primary and secondary running radii R_p and R_s are constant over the complete angles of wrap φ_p and φ_s, it is seen that

$$L = 2a\cos(\varphi) + \varphi_p R_p + \varphi_s R_s \quad ; \quad R_p - R_s = a\sin(\varphi) \tag{3.7}$$

$$\varphi_p = (\pi + 2\varphi) \quad ; \quad \varphi_s = (\pi - 2\varphi) \tag{3.8}$$

where L is the length of the pushbelt and a is the distance between the primary and secondary shaft. The primary and secondary pulley positions x_p and x_s are related to the running radii according to

$$R_p = \frac{x_p}{2\tan(\beta)} + R_0 \quad ; \quad R_s = \frac{-x_s}{2\tan(\beta)} + R_0 \quad ; \quad R_0 = \frac{L_0 - 2a}{2\pi} \tag{3.9}$$

where β is half the pulley wedge angle, R_0 is the running radius if $r_g = 1$ and L_0 is the belt length when the belt is not elongated. The belt elongation $\Delta L = L - L_0$ can be expressed as a relation of the pulley positions x_p and x_s according to

$$\Delta L = \frac{\varphi_p x_p - \varphi_s x_s}{2\tan\beta} - 2a(1 - \cos\varphi) \quad ; \quad \varphi = \arcsin\left(\frac{x_p + x_s}{2a\tan\beta}\right) \tag{3.10}$$

In Section 3.2.2 a relation will be derived between the belt elongation (and therefore x_p and x_s) and the clamping forces F_p and F_s in the variator.

3.2.2 Clamping force model

The clamping forces F_p and F_s play an important role in describing the behavior of the variator. In this section a model is presented, which relates the clamping forces to other variables, like x_p and x_s [52]. A similar approach for a chain drive CVT is presented in [57].
The ADAMS simulation model, described in [45], tries to capture the variator behavior by modeling each component of the metal V-belt as a rigid or flexible body. To analyze the belt-pulley-contact, contact elements are used. In [45] it is claimed that the obtained results are similar to physical tests. However, the CPU time for a simulation is very large, due to the large number of degrees of freedom. This model is suitable for variator analysis, but not for simulations with complete driving cycles. A model for these simulations has to be computationally fast, but nevertheless has to incorporate slip in the variator, clamping forces, etc..
The clamping force model, presented in this section, assumes that the bands of the pushbelt may be seen as a closed string without bending stiffness and that the combination of all discrete blocks may be seen as a one dimensional continuum. Static variator models described by Gerbert [30] and Kim [33] assume the tension force

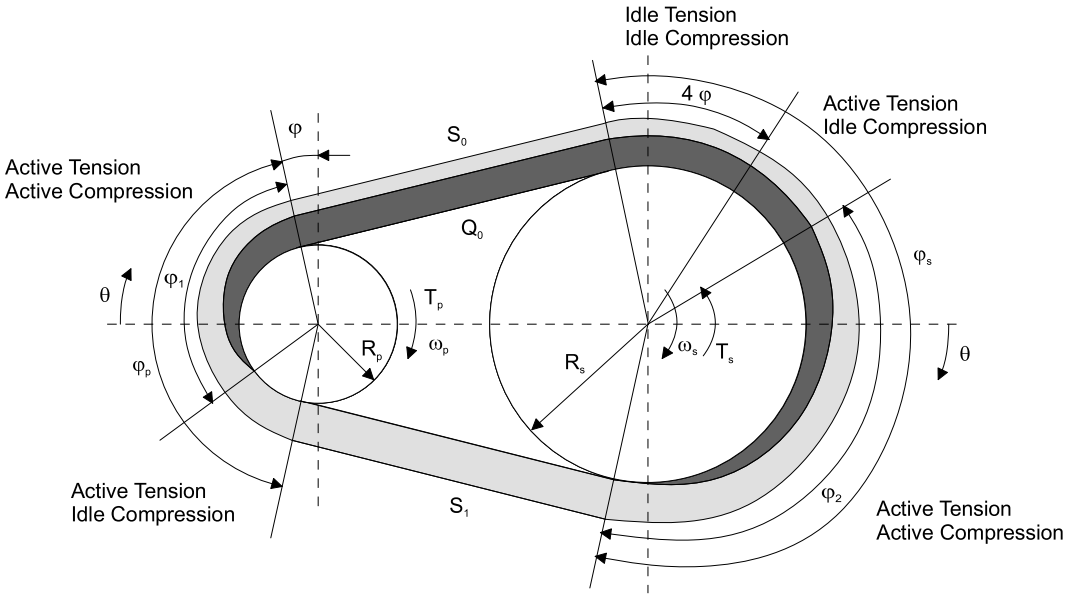

Figure 3.4: Tension and compression forces for $r_g \leq 1$ and $(S_1 - S_0)R_p \leq T_p$ (UD) (note that $\varphi < 0$ in this situation)

to be constant along the belt. In this thesis it is assumed that Coulomb friction is present between the bands and the blocks and between the blocks and the pulley sheaves [111], [54]. Therefore, the tension force in the belt will not be constant. Furthermore, it is assumed that the belt runs at a constant radius over the complete angle of wrap at each pulley, *i.e.* the spiral running of the belt is neglected. The details of the presented model are given by Vroemen [111] and Kobayashi [54]. In this section only the basic relations are given, including the adaptation of this model in order to incorporate it in the complete Empact CVT simulation model.

This model gives insight in the tensile force S in the bands of the belt and the compressive forces Q between the blocks of the belt. The compression force between the blocks can not be higher than the tension force in the bands, because else buckling of the belt could occur.

Four different regimes of operation have to be distinguished. First, a distinction is made between underdrive (U), where $r_g \leq 1$, and overdrive (O), where $r_g > 1$. Second, a distinction is made between a driving (D) situation, where $T_p\omega_p \geq 0$, and a driven or reversed situation (R), where $T_p\omega_p < 0$. In the driving situation the primary shaft drives the secondary shaft, whereas in the reversed situation the secondary shaft drives the primary shaft. For the sake of shortness, only the underdrive driving (UD) regime will be discussed here. Other regimes can be described in similar ways [111].

Figure 3.4 shows the UD case. For this regime, the compression force Q is built up at the primary pulley along the active compression arc φ_1, leaving an idle compression arc $\varphi_p - \varphi_1$ where $Q = 0$. The tension force S is reduced from S_1 to S_0 over

the complete arc φ_p. At the secondary pulley, Q is reduced over the active arc φ_2, whereas S is built up over an equally large arc as it is reduced at the primary pulley, *i.e.* $\varphi_1 = \varphi_2$. At this driven pulley both an idle compression arc, where $Q = Q_0$, and an idle tension arc, where $S = S_0$, exist. The part of the belt where $Q > 0$ is called the dense part. Here, the pushbelt elements are pushed against each other. The part where $Q = 0$ is the slack part. Here, the elements slide free over the bands. To get an expression for the primary and the secondary clamping force, first a relation is derived between the tension force and the elongation of the belt. From this expression, the compression force Q can be obtained. Next, the active arcs are estimated using the maximum compression force Q_0. After that it is straightforward to calculate the clamping forces F_p and F_s. The details of these successive steps are described below.

Tension force

It is assumed that the bands behave according to Hooke's law, so the elongation can be expressed as

$$\Delta L = \frac{1}{EA} \int_y S(y) dy \tag{3.11}$$

where y is a coordinate along the belt, E is Young's modulus and A is the cross sectional area of the bands. Rewriting this equation for the UD case gives

$$\begin{aligned} EA\Delta L &= \int_{-\frac{1}{2}\varphi_p}^{\frac{1}{2}\varphi_p} S^p(\theta) R_p d\theta + \int_{\frac{1}{2}\varphi_s - \varphi_p}^{\frac{1}{2}\varphi_s} S^s(\theta) R_s d\theta + ... \\ & \quad (S_0 + S_1)\, a\cos(\varphi) + S_0 R_s 4\varphi \end{aligned} \tag{3.12}$$

The tension forces $S^p(\theta)$ and $S^s(\theta)$ along the primary, respectively the secondary active tension arcs are given by [111]

$$S^p(\theta) = (S_0 - F_B) e^{\mu_1 \left(\frac{1}{2}\varphi_p - \theta\right)} + F_B \quad ; \quad \text{for } \theta \in \left[-\frac{\varphi_p}{2}, \frac{\varphi_p}{2}\right] \tag{3.13}$$

$$S^s(\theta) = (S_0 - F_B) e^{-\mu_1 \left(\frac{1}{2}\varphi_s - \varphi_p - \theta\right)} + F_B \quad ; \quad \text{for } \theta \in \left[\frac{\varphi_s}{2} - \varphi_p, \frac{\varphi_s}{2}\right] \tag{3.14}$$

$$S^s(\theta) = S_0 \quad ; \quad \text{for } \theta \in \left[-\frac{\varphi_s}{2}, \frac{\varphi_s}{2} - \varphi_p\right] \tag{3.15}$$

where μ_1 is the friction coefficient between the bands and blocks and $F_B = \rho_b v_{belt}^2$ is the centrifugal force of the bands with ρ_b mass per unit length. The relation between the tension forces S_1 in the slack part and S_0 in the dense part of the belt is given by

$$S_1 = (S_0 - F_B)\, e^{\mu_1 \varphi_p} + F_B \tag{3.16}$$

By substituting (3.13), (3.15) and (3.16) in (3.12), an explicit relation can be obtained between S_0, ΔL and φ. Next, the tension force S_0 can be determined as a function of the centrifugal force F_B, the pulley positions x_p and x_s, using the relations from Section 3.2.1.

Compression force

The next step on the path from pulley position to the clamping forces, is to calculate the compression force in the belt. The compression force Q^p at the primary active compression arc and the compression force Q^s at the secondary active compression arc (Figure 3.4) can be expressed as

$$Q^p(\theta) = S^p(\theta) + F_C - \left(S^p(\theta_1) + F_C\right) e^{\frac{\mu_2}{\sin\beta}(\theta_1-\theta)} \quad ; \quad \text{for } \theta \in \left[\theta_1, \frac{1}{2}\varphi_p\right] \tag{3.17}$$

$$Q^s(\theta) = S^s(\theta) + F_C - \left(S^s(\theta_2) + F_C\right) e^{\frac{\mu_2}{\sin\beta}(\theta_2-\theta)} \quad ; \quad \text{for } \theta \in \left[\theta_2, \frac{1}{2}\varphi_s\right] \tag{3.18}$$

where $\theta_1 = \frac{1}{2}\varphi_p - \varphi_1$, $\theta_2 = \frac{1}{2}\varphi_s - \varphi_2$, μ_2 is the friction coefficient between the elements and the pulley, $F_C = \rho_c v_{belt}^2$ is the centrifugal force of the blocks with ρ_c mass per unit length and φ_1 is the magnitude of the active compression arc. The unknown active angles φ_1 and φ_2 have to be determined suing the boundary conditions $Q^p(\theta) = Q_0$ for $\theta = \frac{1}{2}\varphi_p$ and $Q^s(\theta) = Q_0$ for $\theta = \frac{1}{2}\varphi_s - \varphi_2$.
The maximum compression force Q_0 can be obtained from

$$T_{p,i} = Q_0 R_p + (S_1 - S_0)(R_p + \Delta R) \tag{3.19}$$

where $T_{p,i}$ is the internal torque exerted by the belt on the primary pulley and ΔR is the distance between the radius of the bands R_p and that of the rocking edges of the V-belt blocks.

Active compression arcs

By introducing the boundary condition for Q, an expression can be obtained for the maximum compression force Q_0 as a function of the active compression arcs. For the UD case these relations are given by

$$Q_0 = (S_0 - F_B)\left(1 - e^{\left(\mu_1 - \frac{\mu_2}{\sin(\beta)}\right)\varphi_1}\right) + F_C\left(e^{-\frac{\mu_2}{\sin(\beta)}\varphi_1} - 1\right) \tag{3.20}$$

for the primary pulley and

$$Q_0 = (S_0 - F_B)\left(e^{\mu_1(\varphi_p-\varphi_2)} - e^{-\frac{\mu_2}{\sin(\beta)}\varphi_2+\mu_1\varphi_p}\right) + F_C\left(e^{-\frac{\mu_2}{\sin(\beta)}\varphi_2} - 1\right) \tag{3.21}$$

for the secondary pulley. An explicit solution for the size of the active compression arcs φ_1 and φ_2 can not be found from these equations. However, if the exponential functions are approximated by $e^{-\mu_1\varphi_2} \approx \frac{a+b\varphi_2}{c+d\varphi_2}$, it is possible to find an explicit solution. Figure 3.5 shows the estimation of φ_1 and the estimation error as a function of the tension force S_0 and the compression force Q_0 in the belt. In the dashed area $Q_0 > S_0$, which would lead to buckling of the belt. It can be seen that when a large tension force is present in comparison to the compression force, the active arc is small, whereas the active arc increases to the complete wrapped angle when the compression force increases or the tension force decreases.

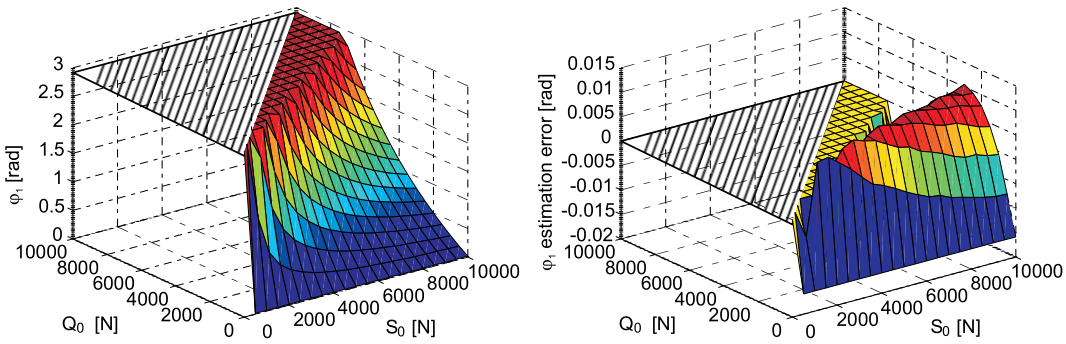

Figure 3.5: Estimation of φ_1 at $r_g = 1$ and $w_p = 250$ [rad/s]

Resulting clamping force

Now the tension force, compression force and active arcs are known, it is possible to find the primary clamping force F_p and secondary clamping force F_s by integrating the sum of the tension and compression force over the wrapped angles, according to

$$F_p = \int_{\varphi_p} \frac{S^p(\theta) - Q^p(\theta) - F_B - F_C}{2\tan\beta} d\theta \tag{3.22}$$

$$F_s = \int_{\varphi_s} \frac{S^s(\theta) - Q^s(\theta) - F_B - F_C}{2\tan\beta} d\theta \tag{3.23}$$

A similar derivation of the clamping forces can be made for the underdrive reversed (UR), the overdrive driven (OD) and the overdrive reversed (OR) situation. Details of these situations are given in [111]. In [20] it is shown that the ratio between the primary and secondary clamping force, according to this model, fairly well agrees with the experimentally determined clamping force ratio, at least for stationary situations.

3.2.3 Torque transmission

The torques $T_{p,i}$ and $T_{s,i}$, exerted by the belt on the primary, respectively secondary pulley, depend on the clamping forces F_p and F_s, on the slip ν and on the geometric ratio r_g [12], [47]. For the UD case these torques are given by

$$T_{s,i} = \frac{2\mu(\nu, r_g) F_s R_s}{\cos(\beta)} \tag{3.24}$$

$$T_{p,i} = r_g T_{s,i} \tag{3.25}$$

where the traction coefficient $\mu(\nu, r_g)$ is the effective friction coefficient between the belt and pulleys, averaged over the complete wrapped angle. In [11] and [9] it is shown that the traction coefficient does not depend on the primary pulley speed ω_p. A similar relation holds for the OD, UR and OR cases, if the clamping force in 3.24 is replaced by $\min(F_p, F_s)$.

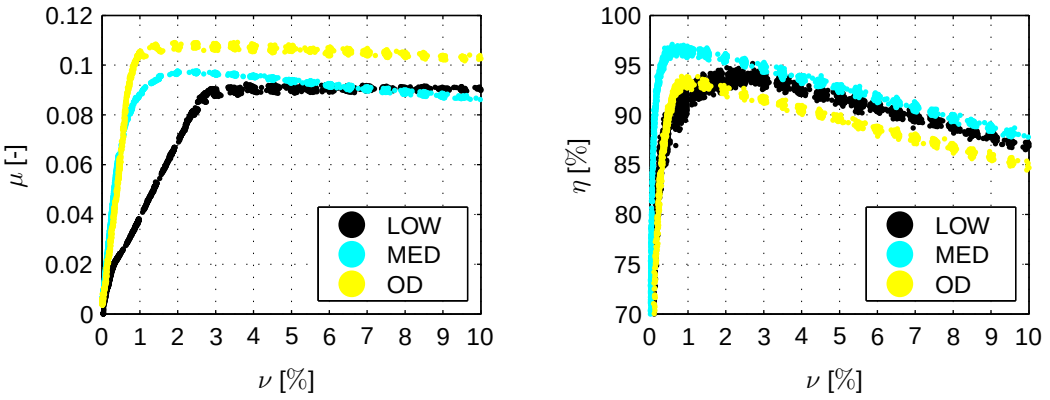

(a) Traction coefficient

(b) Variator efficiency

Figure 3.6: Variator measurement results from a belt box [11] in $r_g = 0.4$ (LOW), $r_g = 1.1$ (MED) and $r_g = 2.26$ (OD)

In [9] the traction curve μ is reconstructed from measurements at a stand-alone variator. Because in these measurements the torques T_p and T_s in the input, respectively the output shaft of the variator are measure, and not the internal torques $T_{p,i}$ and $T_{s,i}$ exerted by the belt at the pulleys, the experimentally determined traction coefficient incorporates the torque losses due to friction in the bearings of the variator. These losses are small and may be neglected at the used experimental setup. The dissipation due to friction between bands and blocks of the pushbelt is also incorporated in μ. These losses will also be present in the variator of the Empact CVT and are therefore assumed to be part of the variator model.
Figure 3.6(a) gives an example of an experimentally determined traction coefficient μ as a function of the slip ν for these values (LOW, MED and OD) of the geometric ratio r_g. It can be seen that with increasing ν, μ also increases until a certain maximum value is reached. For higher slip values μ even shows a decrease for some ratios. This behavior is typical for friction drives like tyres, clutches and mechanical CVT's.
Although the measurements were performed in (quasi-)stationary conditions, the traction relations from (3.24) and (3.25) will also be used for transient situations.
At the maximum traction level, the clamping force, needed to transmit a given torque T_p, is minimal. As the frictional losses increase with increasing clamping force, the efficiency decreases with increasing clamping forces. Figure 3.6(b) shows the variator efficiency $\eta = T_s\omega_s/(T_p\omega_p)$ against the slip ν for three different ratios. It can be seen that peak efficiency is reached at slip levels just below the top traction level. At the point of maximum efficiency, the slope of the traction curve is still positive, but a minor change of the slip level causes the slope to change significantly and may even make the slope negative, possibly resulting in unstable behavior. Hence,

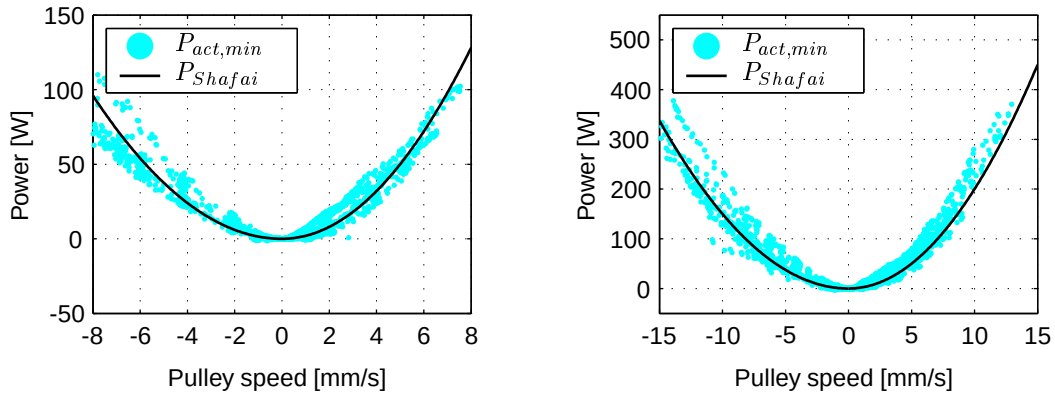

(a) Measurements for $F_s = 10$ kN and $\omega_p = 150$ rad/s

(b) Measurements for various F_s and ω_p

Figure 3.7: Minimal actuation power and actuation power according to Shafai

to optimize CVT efficiency, the slip level in the variator must be controlled at a level close to the maximum traction level using a robustly stabilizing controller.

3.2.4 Transient variator model

Transient variator models, like those of Ide *et al.* [40], Shafai *et al.* [88] and Carbone *et al.* [18], describe the rate of ratio change $\dot{r}_g$ as a function of, amongst others, the actual clamping force F_p and the clamping force F_p^* needed to maintain a stationary CVT ratio. Whereas Ide *et al.* and Carbone *et al.* give a nonlinear relation for $\dot{r}_g$, depending on the difference $F_p - F_p^*$, the ratio, the primary speed and the input torque, Shafai *et al.* give a linear relation between the clamping force and the velocity $\dot{x}_p$ of the moveable primary pulley sheave according to

$$m_s \ddot{x}_p + b_s \dot{x}_p = F_p - F_p^* \tag{3.26}$$

where m_s is a representative mass of the sheave and the belt and b_s is the Shafai damping constant. Here $m_s \ddot{x}_p$ is relatively small compared to $b_s \dot{x}_p$ and can therefore be neglected. The minimally required mechanical power to move the pulley sheaves is given by (2.1). By combining (2.1) and (3.26), the power required to enable a ratio change in the Shafai model can be given by

$$P_{Shafai} = \dot{x}_p F_p - \dot{x}_s F_s = \dot{x}_p \left(F_p^* + b_s \dot{x}_p \right) - \dot{x}_s F_s \tag{3.27}$$

Using the geometrical relation $\dot{x}_s = f(x_p)\dot{x}_p$, which can be derived from (3.10) assuming that the belt elongation can be neglected, and the pulley thrust ratio $\kappa = F_p^*/F_s$ (see Appendix B.1) [111], [40], [9], this leads to

$$P_{Shafai} = b_s \dot{x}_p^2 + \left(\kappa - f(x_p) \right) F_s \dot{x}_p \tag{3.28}$$

It is assumed that the latter term can be neglected compared to the first term, resulting in a quadratic relation between the dissipated power during shifting and the shifting speed.
Figure 3.7(a) shows again the measured $P_{act,min}$ at the CK2 test setup from Figure 2.7(a). During this measurement, the clamping force was kept constant at $F_s = 10$ [kN] and the primary shaft speed was controlled at $\omega_p = 150$ [rad/s]. In the figure also the actuation power estimated using (3.28) is depicted. The results show indeed a quadratic relation between $\dot{x}_p$ and the actuation power, *i.e.* a linear relation between $\dot{x}_p$ and the actuation force. However, for $\dot{x}_p < 0$ the estimated Shafai damping constant $b_s = 1.5 \cdot 10^6$ [Nm/s] and for $\dot{x}_p > 0$ the estimated Shafai damping constant $b_s = 2.0 \cdot 10^6$ [Nm/s]. Results of measurements, carried out at higher clamping forces and at different ω_p, are depicted in Figure 3.7(b). Here, the same Shafai power estimation is shown, which fits the data very well. The dependency on clamping force, ratio, primary speed and input torque as described by Ide and Carbone can therefore be neglected.

3.3 Empact actuation system

The actuation system of the Empact CVT can be described using a lumped parameter model. Rigid bodies are described using a representative mass or inertia, elasticity of the bodies is modeled by spring elements and dissipation in the materials is represented by damper elements.
In the Empact simulation model, the translational stiffness and damping of the thrust bearing is represented by a parallel combination of a linear spring and damper at the thrust bearing location. The pushbelt stiffness is incorporated in the variator model by the elongation of the belt as described in Section 3.2.2. The stiffness and damping of the rotating parts of the actuation system are represented by a torsional spring and a damper between the worm gear and servo motor and by a parallel combination of a linear spring and damper for the chain transmission [67]. Although pulley bending has a significant effect on the variator shifting behavior [9], [18], [82], [92], thorough analysis shows that this effect on the dynamics of the Empact actuation system can be neglected in the frequency range of interest (below 100 [Hz]). All other elements, *i.e.* the spindles and the gears, of the Empact CVT are considered rigid in this frequency range. The resulting actuation model is outlined in Figure 3.8.
For a compact description of the kinematics of the Empact actuation system, a special notation is introduced. The rotation of the gears of the epicyclic sets are referred to as $\theta_{\alpha\beta\gamma}$. Here, $\alpha = \{a, c, p, s\}$ refers to the annulus, carrier, planet and sun respectively, $\beta = \{l, r\}$ refers to the left and right epicyclic set and $\gamma = \{p, s\}$ refers to the primary or secondary side of the Empact CVT. Furthermore, the translation

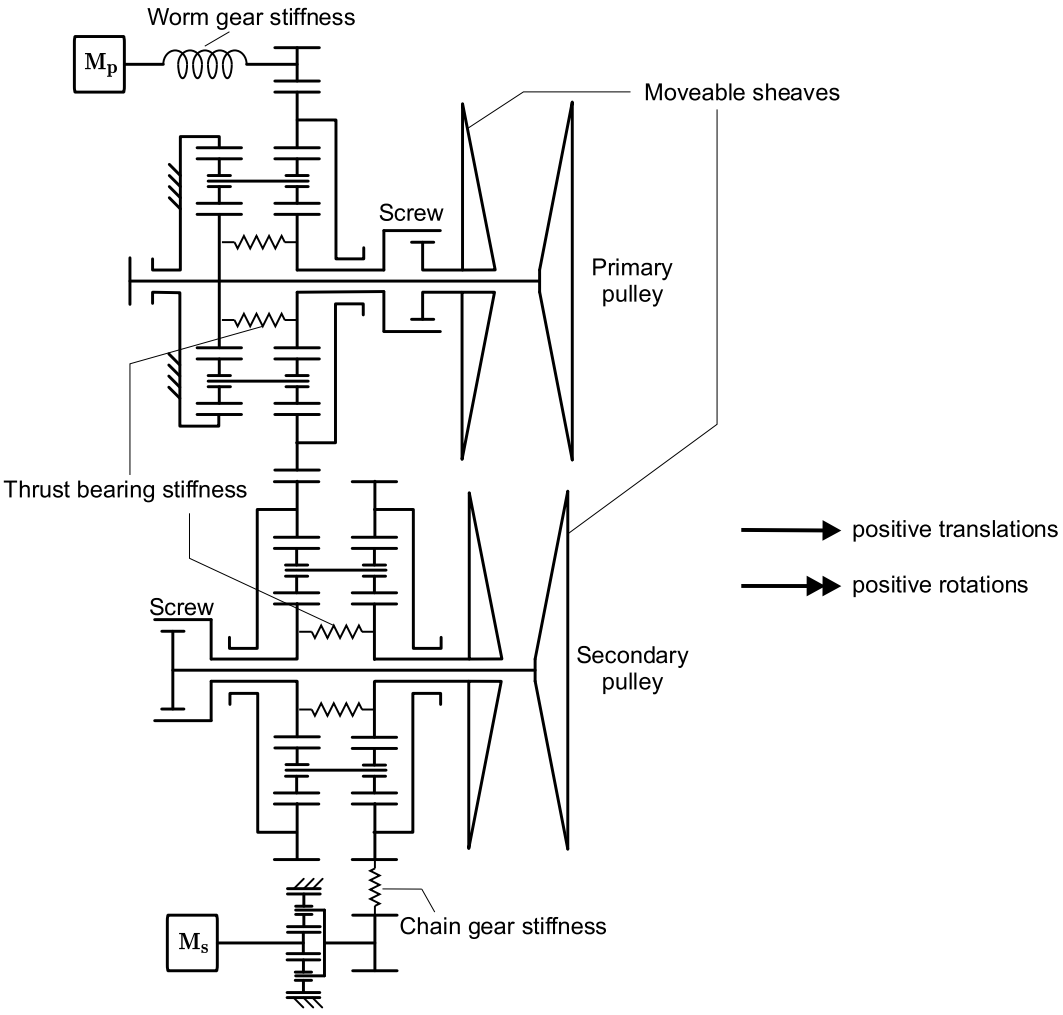

Figure 3.8: Schematic representation of the Empact actuation system model

of the moveable pulley sheaves, the rotation of the CVT shafts, the rotation of the servomotors and the translation of the nut of both spindles will be referred to as x_γ, θ_γ, $\theta_{m\gamma}$ and $x_{n\gamma}$ respectively. The origin of these variables is chosen such that they are equal to zero in the reference configuration, *i.e.* the configuration with geometric ratio $r_g = 1$ and undeformed, stress-free springs. Sign conventions for translations and rotations are shown in Figure 3.8.

3.3.1 Kinematics

The kinematic relations of a single epicyclic gear are given by

$$\begin{aligned} \omega_s &= (z+1)\omega_c - z\omega_a \\ \omega_s &= z\omega_a - (z-1)\omega_p \end{aligned}$$

where ω_s, ω_c, ω_a and ω_p are the angular velocities of the sun, carrier, annulus and planet gears, respectively, and z is the ratio of the radii of the annulus and the sun gear. Extending these relations to the epicyclic sets of the Empact system results in

$$(z+1)\,\dot{\theta}_{clp} = \dot{\theta}_p \tag{3.29}$$
$$\dot{\theta}_{srp} = \dot{\theta}_p - z\dot{\theta}_{arp} \tag{3.30}$$
$$(z-1)\,\dot{\theta}_{plp} = -\dot{\theta}_p \tag{3.31}$$
$$(z-1)\,\dot{\theta}_{prp} = -\dot{\theta}_p + 2z\dot{\theta}_{arp} \tag{3.32}$$
$$(z+1)\,\dot{\theta}_{cls} = \dot{\theta}_s + z\dot{\theta}_{ars} \tag{3.33}$$
$$\dot{\theta}_{sls} = z\dot{\theta}_{arp} + \dot{\theta}_s + z\dot{\theta}_{ars} \tag{3.34}$$
$$(z-1)\,\dot{\theta}_{pls} = -2z\dot{\theta}_{arp} - \dot{\theta}_s - z\dot{\theta}_{ars} \tag{3.35}$$
$$(z-1)\,\dot{\theta}_{prs} = -\dot{\theta}_s + z\dot{\theta}_{ars} \tag{3.36}$$

In these relations, the fact that the left primary annulus is fixed to the ground and that the right primary annulus is connected to left secondary annulus, is taken into account. The translation from the sun rotations to the pulley translation is performed by the screw transmission at both shafts. The kinematic relation of a screw transmission is given by

$$\dot{x}_b - \dot{x}_n = s(\dot{\theta}_b - \dot{\theta}_n)$$

where s is the pitch of the screw, $\dot{x}_b$ and $\dot{x}_n$ are the translational velocities of the bold and nut, whereas θ_b and θ_n are the rotations of the bold and nut. For the primary screw with pitch s and the secondary screw with opposite pitch $(-s)$, this relation results in

$$\dot{x}_{np} = \dot{x}_p - s(\dot{\theta}_{srp} - \dot{\theta}_p) = sz\dot{\theta}_{arp} + \dot{x}_p \tag{3.37}$$
$$\dot{x}_{ns} = \dot{x}_s + s(\dot{\theta}_{sls} - \dot{\theta}_s) = sz\dot{\theta}_{arp} + sz\dot{\theta}_{ars} + \dot{x}_s \tag{3.38}$$

3.4 Friction models

To account for the power losses in the Empact CVT, friction models for bearings, gears, variator and screw transmissions are incorporated in the simulation model using the LuGre friction model [69], [68], [70], [16]. This friction model incorporates physical effects like stick-slip and frictional lag by describing the average displacement of a set of bristles that represent the contact surface between two bodies. Using the LuGre model, the friction torque T_{LuGre} between two bodies is given by

$$T_{LuGre} = \sigma_0 z + \sigma_1 \dot{z} + \sigma_2 \dot{x} \tag{3.39}$$

$$\dot{z} = \dot{x} - \sigma_0 \frac{|\dot{x}|}{g(\dot{x})} z \tag{3.40}$$

where σ_0 and σ_1 are the bristle stiffness and damping respectively, z is the average bristle deflection, $\dot{x}$ is the relative velocity between the bodies and $g(\dot{x})$ is a positive function which describes the type and level of friction.
The bristle stiffness and damping parameters are mostly important to describe the stick-slip behavior and hysteresis. These phenomena only play a role at low velocity, or when crossing zero velocity. As the model of the Empact CVT will only be used to simulate forward driving at representative vehicle velocities ($v_{car} > 15$ [km/h]), proper estimations of σ_0 and σ_1 are only necessary for the worm gear, chain gear, the screw gears and thrust bearings. For these parts, measurements at dedicated test setups have been performed to estimate the friction parameters. Further optimization of the estimations are performed during validation experiments at the Empact test rig, described in Section 3.5. For all other gears and bearings, σ_0 and σ_1 are chosen relatively small. The LuGre implementation for these elements is only required for numerical reasons during start of the simulation. The type and level of the friction is described by

$$g(\dot{x}) = T_f \tag{3.41}$$

where the friction torque T_f is depending on the type of element, *i.e.* bearing, gear or screw.
The friction torques in the gears are estimated using models described in [74], [43] and [113]. In these models, T_f is given by

$$T_{f,tooth} = T_{in} H_v f \tag{3.42}$$

where $T_{f,tooth}$ is the tooth friction torque, T_{in} is the input torque at the gear, H_v depends on the geometry of the gears and f, the coefficient of friction according to Kelley [6], [46], [110], depends on lubrication parameters.
The friction torque for rolling element bearings can be estimated by

$$T_{f,bearing} = T_l + T_v \tag{3.43}$$

where T_l is the load dependent static friction torque and T_v is the viscous friction torque. Palmgren [72], [34] empirically found that these torques are given by

$$T_l = f_1 F_\beta d_m \tag{3.44}$$

$$T_v = 10^{-7} f_0 (N\nu_l)^{2/3} d_m^3 \quad N\nu_l > 2000 \tag{3.45}$$

$$T_v = 160 \cdot 10^{-7} f_0 d_m^3 \quad N\nu_l \leq 2000 \tag{3.46}$$

where f_0 and f_1 depend on the type of bearing and lubrication, F_β is the bearing load, d_m is the mean bearing diameter, ν_l is the lubricant viscosity and N is the rotational speed in revolutions per minute.
The friction torques of the screws and worm, defined at the input side, are based on the efficiency of the corresponding element, expressed as

$$T_f = T_{in}(1 - \eta) \tag{3.47}$$

where T_{in} is the input torque and η is the efficiency of the corresponding element. Validation measurements for the secondary spindle are performed. It is shown that the estimation fits the measured data very well.
Friction torques in both servos and chain transmission are considered to be independent on the load.
Finally, the variator torque losses $T_{f,var}$ are estimated by measurements at the CK2 transmission presented in [109].

3.5 Validation results

This section presents some time domain validation results for the Empact CVT simulation model. Frequency domain validation of this model is described in Chapter 5. Figure 3.9 shows a comparison of results from a simulation and measurement at the test rig. The depicted experiment starts at a constant input speed of $w_p = 150$ [rad/s], a torque of $T_{S_2} = 20$ [Nm] exerted by the load motor S_2 on the system and a secondary servo torque of $T_{ms} = 0.2$ [Nm], which corresponds to approximately $F_s = 10$ [kN] in stationary conditions. First, from $t = 31$ [sec] to $t = 38$ [sec], the CVT shifts from $\hat{r}_g = 0.5$ to $\hat{r}_g = 2.0$ with $\dot{x}_p = 2$ [mm/s]. At $t = 41$ [sec], the secondary actuator torque is increased to $T_{ms} = 0.4$ [Nm]. Next, from $t = 47$ [sec] to $t = 56$ [sec], the load torque is increased to 90 [Nm]. Finally, from $t = 59$ [sec] to $t = 67$ [sec], the CVT shifts back to $r_g = 0.5$ and from $t = 70$ [sec] to $t = 97$ [sec] the load torque is increased to 205 [Nm]. Figure 3.10 shows the estimated tension and compression forces and the active compression arcs during the simulation.
To match the results of the simulation model to the results from the measurement, the friction plays a significant role. Especially the Coulomb friction of the worm gear and screws is high. During shifting, the friction in the spindles decreases the actual clamping forces in the variator. The hysteresis of the friction also has influence on

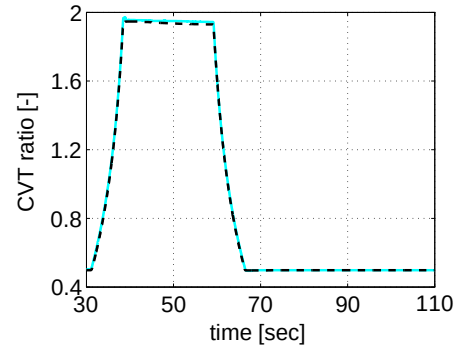

(a) CVT ratio $\hat{r}_g$

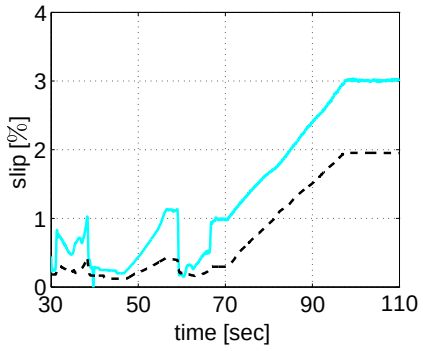

(b) Slip $\hat{\nu}$

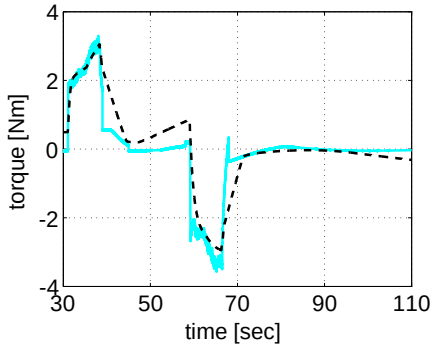

(c) Primary servo torque T_{mp}

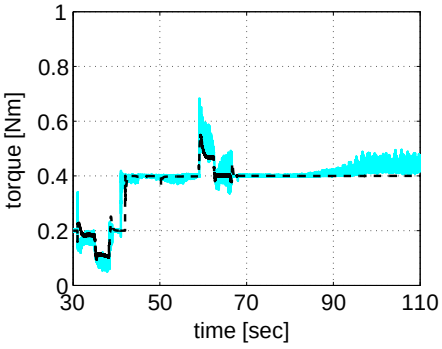

(d) Secondary servo torque T_{ms}

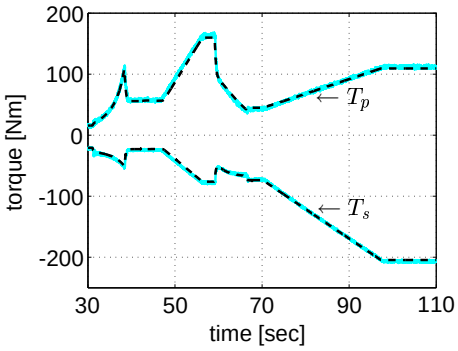

(e) Input torque and output torque

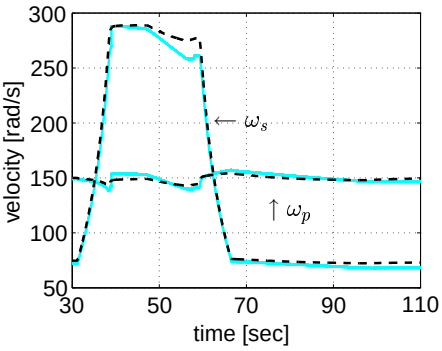

(f) Primary and secondary shaft velocity

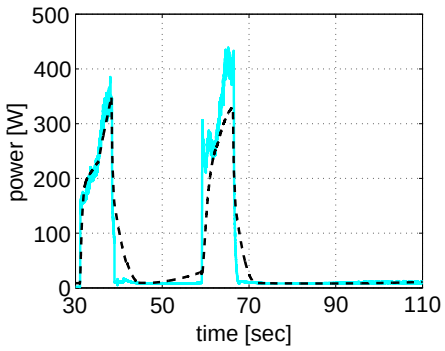

(g) Actuation power $P_{act,Empact}$

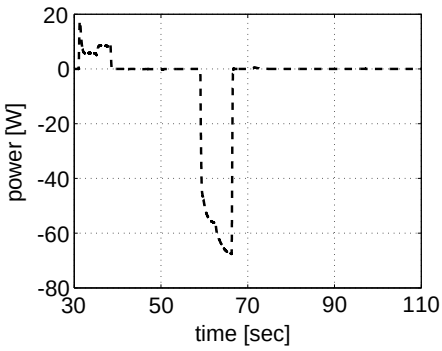

(h) Recovered power by the meshing gears

Figure 3.9: Simulation results (dashed line) and measurement results (solid line)

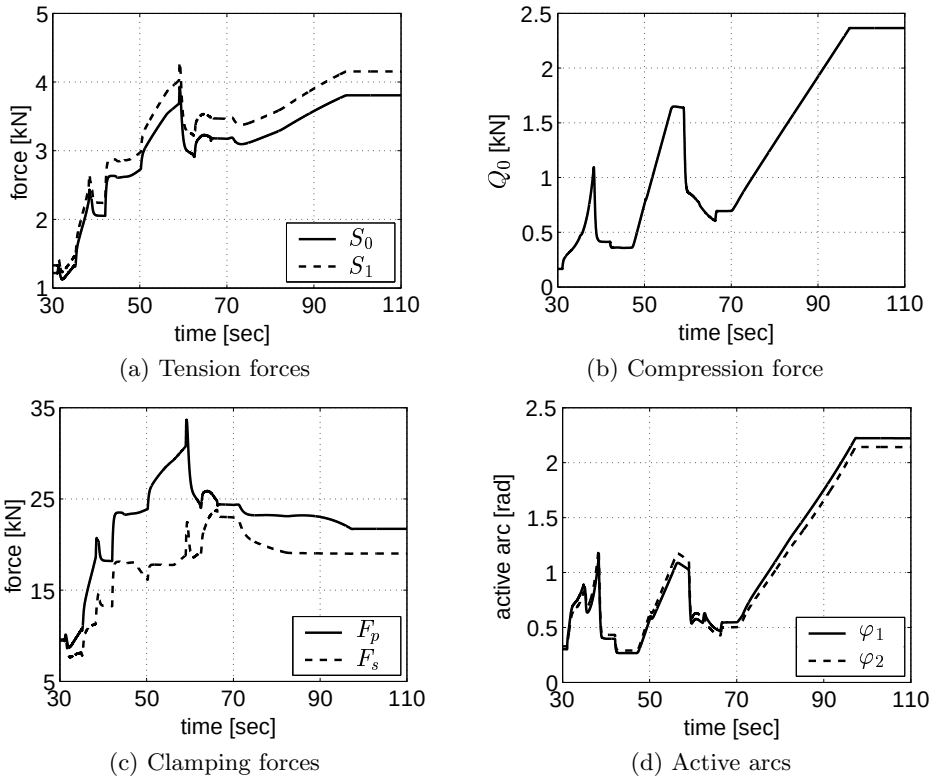

(a) Tension forces (b) Compression force

(c) Clamping forces (d) Active arcs

Figure 3.10: Additional simulation results

the steady state clamping force, as can be seen from Figure 3.10(c). For instance, after the increase of the secondary actuator torque from 0.2 to 0.4 [Nm] at $t = 41$ [sec], the expected secondary clamping force is 20 [kN]. However, due to the friction in the actuation system, the actual clamping force is only 18 [kN]. Another important effect of the friction is that it provides the hold torque for the primary servo when the variator is not shifting. This decreases the primary servo torque T_{mp} to approximately 0 [Nm] in stationary situations. The actuation power in stationary situations is therefore also minimal. As can be seen from Figure 3.9(h), the energy recovery by the meshing gears has the most effect when shifting from OD to LOW. Due to the high power dissipation in the variator and the low efficiency of the spindles, the actuation power reduction by the meshing gears is, during transient behavior, limited to approximately 25 [%].

Most simulation results are very similar to the measurement results, but the slip in the measurement is significantly higher than in the simulation. During shifting this can partly be explained by the fact that radial slip is not accounted for by the variator model. Due to slip in radial direction, the slip in tangential direction increases. However, when the CVT is not shifting, the slip is also larger in the measurement than in the simulation. This could be due to a wrong estimation of the friction in the actuation system. This is however not likely, because the estimated primary servo torque T_{mp}, which strongly depends on the friction losses, shows very

good similarity. A third cause could be that the traction coefficient μ of the Empact CVT differs significantly from the traction curves shown in Figure 3.6(a), which were measured on a different variator. However, a decrease by a factor of two seems very large and is not expected.

Chapter 4

Control problem formulation

The overall control objective for a CVT incorporated in a driveline is to force the engine speed to follow a desired profile. This profile is chosen such that the internal combustion engine is operated close to its optimal operating point, *i.e.* to the point with maximum efficiency under the constraint of a good driveability of the car. Given a required speed profile of the vehicle, the ratio setpoint follows.
As discussed in Chapter 2, in order to use the full potential of the Empact system, the slip in the variator must be controlled. In this way, the clamping forces are minimized to achieve optimal transmission efficiency. Care must be taken then to avoid large, long lasting slip, because these can cause damage to the belt and variator. Slip peaks with short duration however, do not cause wear at the belt or variator, especially when low clamping forces are applied [103], [102].
Because for $|\omega_p| \to 0$ it holds that $|\nu| \to \infty$, *i.e.* slip is undefined at very low input speeds, slip control can not be applied under these operating conditions. Experiments have shown that in case slip is not controlled and only a feedforward clamping force is applied, the secondary actuator shows stick-slip oscillations [35] due to the high level of friction in the system. This significantly influences the driveability. This effect will be shown in Chapter 7 using experimental results. To minimize the stick-slip oscillations, the velocity of the secondary servo ω_{ms} will be controlled in addition to the ratio and slip.
The control problem can be formulated as to find a controller K, such that the controlled system is robustly stable and has robust performance. Robustly means here under all plant perturbations and disturbances. Section 4.1 gives a description of the system inputs, outputs and the disturbances that act on the system. The performance specifications are explained in Section 4.2 by means of a disturbance model. The description of the control architecture in Section 4.3 forms a basis for the control design presented in Chapter 6. Finally, Section 4.4 discusses some issues on design limitations.

4.1 System description

The variables to be controlled are the CVT ratio r_g, the slip ν in the system and the secondary actuator velocity ω_{ms}. This velocity can be directly obtained from the measured servo position θ_{ms}. However, the ratio and slip can not be measured directly in the variator [9] and must therefore be estimated from measurable variables. The measured variables in the Empact CVT are the primary and secondary servomotor rotations θ_{mp} and θ_{ms} and the primary and secondary shaft velocities ω_p and ω_s. If the torsional compliances and the thrust bearings are considered to be rigid, the relations (3.29) to (3.38) can be extended with

$$\theta_{mp} = r_w \theta_{arp} \quad ; \quad \theta_{ms} = r_r r_c \theta_{ars} \quad ; \quad x_{np} = 0 \quad ; \quad x_{ns} = 0 \tag{4.1}$$

where r_w, r_r and r_c are the reduction of the worm gear at the primary side and of the planetary reduction gear and chain reduction at the secondary side, respectively. When combining these relations, x_p and x_s can be expressed as a function of θ_{mp} and θ_{ms} according to

$$x_p = \frac{\theta_{mp}}{r_w} sz \quad ; \quad x_s = \left(\frac{\theta_{ms}}{r_r r_c} + \frac{\theta_{mp}}{r_w} \right) sz \tag{4.2}$$

Hence, by using (3.9), an estimate $\hat{r}_g$ for the geometric ratio can be obtained. Because of the large transmission ratio between both servos and moveable pulley sheaves and the relatively high stiffness of the thrust bearings, the error made in this estimation is very small. When torques $T_{mp} = 10$ [Nm] and $T_{ms} = 1$ [Nm] are applied at the servos, which exceed the maximum servo torques as used in the Empact CVT, the errors for the pulley position estimation are less than $2 \cdot 10^{-5}$ [m]. From a control perspective, it is interesting to directly control the measured θ_{mp}, such that a co-located feedback with respect to the input T_{mp} is obtained. Therefore, the static reconstruction (3.9 and 4.2) is used to obtain $\theta_{mp,ref}$ from $r_{g,ref}$ and the position θ_{mp} is controlled instead of the estimated geometric ratio $\hat{r}_g$.
The slip, as defined in (3.6) is reconstructed using $\hat{\nu} = 1 - \frac{\omega_s}{\omega_p} \hat{r}_g^{-1}$. The largest slip estimation error is ± 0.2 [%]. This error can influence the achieved performance in terms of efficiency. However, by relating the slip reference to the optimal efficiency from a traction curve that is measured using the estimated slip $\hat{\nu}$, this error is avoided. Stability or performance problems due to internal dynamics are not expected, because of the high damping level in the system.
The input variables of the Empact CVT are the primary and secondary servomotor torque, T_{mp} and T_{ms} respectively, whereas the driveline torques T_p and T_s can be regarded as disturbances on the system. Here, T_p represents the drive torque at the primary shaft of the CVT and T_s represents the load torque at the secondary shaft of the CVT. The resulting plant P with disturbances, inputs, measured variables and mapping $\mathcal{M}$ to the controlled outputs variables is shown in Figure 4.1.
Based on this system description, the controlled variables are defined as the servo

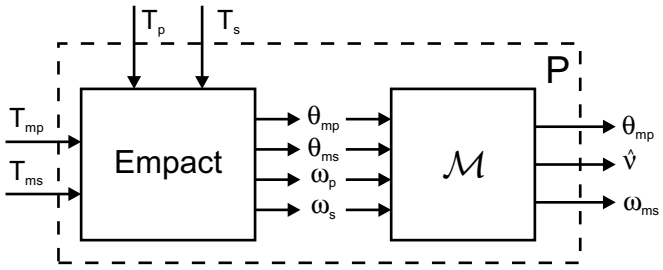

Figure 4.1: Plant P description

position tracking error $e_{\theta_{mp}}$, slip error $e_{\hat{\nu}}$ and the secondary servo velocity error $e_{\omega_{ms}}$.

4.2 Performance specification and system requirements

An important constraint for the controlled system is that slip cannot be controlled under all operating conditions. As already indicated in Section 3.2, at low speeds the open loop slip dynamics becomes infinitely fast, which leads to a loss of controllability. Furthermore, to control slip at low driveline torques, the clamping forces must be decreased to very low values, which could lead to a control problem due to backlash in the chain and to the relatively high friction in the system. Besides this problem, achieving optimal efficiency at these torques is not particularly interesting, because the effective power loss $T_p\omega_p(1-\eta_{Empact})$ is very small. This obviously also holds for low ω_p. Therefore, it has to be possible to switch off the slip controller at low speeds and low transmitted torques. A further requirement is that, if an integral control is used in the slip controller, it must be possible to reset the integrator state since fast slip peaks at low input speeds could cause the integrator to wind up.
Later on it will be shown that control of the secondary actuator velocity ω_{ms} increases the shifting performance. However, control of θ_{ms} is not desired. If the secondary clamping force is changed, a displacement of the secondary pulley occurs due the belt compliance and with that also a change of θ_{ms}. Hence, if θ_{ms} is fixed by the controller, which would be the result if a stiff controller is applied, this would lead to a loss of controllability of the slip in the system. Therefore, the low frequency gain of the ω_{ms} controller must be limited, *i.e.* no integrating behavior is desired.
To specify the performance requirements of both ratio and slip control, the effect of the driveline torques on the ratio and slip are analyzed. At the input side of the CVT, the disturbance torque T_p stems from the internal combustion engine. Since the throttle position and engine speed are measured, the engine torque is known with reasonable accuracy. This torque is transmitted through the TC and DNR set to the CVT. Since the state of the TC (lockup engaged or not) and of the DNR set are controlled, the disturbance torque T_p is known at each moment and may be

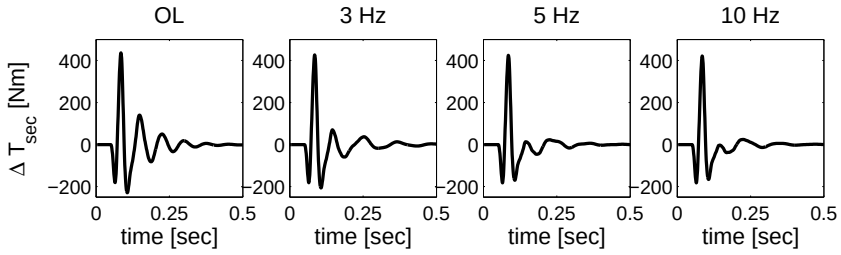

(a) Secondary torque disturbance

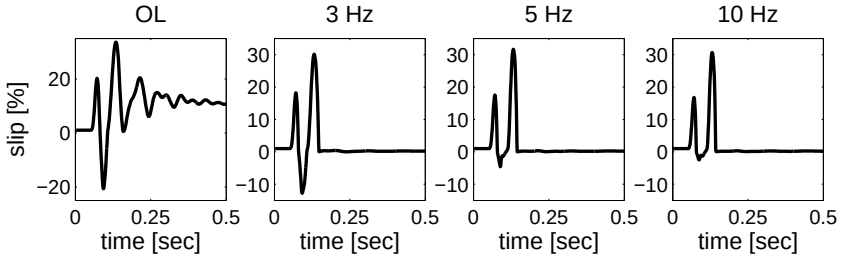

(b) Slip

Figure 4.2: Disturbance simulation results when driving over a curb of 150 [mm] height with $v_{car} = 40$ [kph] and $r_g = 2.2$ without slip control (OL) and for different bandwidths (as indicated)

accounted for in the controller using feedforward or computed torque compensation. The influence of T_p is therefore left out of further disturbance analysis. The effect of the load torque T_s on the ratio and slip is estimated using simulations, resulting from a model for a complete front-wheel drive powertrain [73]. This model includes models for the ICE, TC, variator, FDR, differential gear, left and right driveshafts, tyres and vehicle suspension. The tyres are modeled using MF SWIFT 6.0 tyre models [8] with rigid ring dynamics and 2D track road contact method [83]. This model describes the dynamic tyre behavior accurately up to 100 [Hz]. The variator is modeled as described in Section 3.2. For ease of ratio and slip control design, actuation forces are directly applied at the moveable pulley sheaves, *i.e.* the Empact actuation system is left out here.

The final model is of order 32, in addition to the internal degrees of freedom of the tyre and variator models. Torque disturbances are introduced into the driveline by the road height profile given by ISO 8608:1995(E) specifications and by several characteristic obstacles as defined by [83].

Simulations are performed at multiple operating points, defined by the vehicle velocity, CVT ratio, engine torque and slip level. In each of these points different road disturbances are applied. The performance of a low and high bandwidth ratio controller, a low and high bandwidth slip controller, open loop clamping force control and combination of these are analyzed.

Figure 4.2 shows a typical result of the secondary load torque variation and slip re-

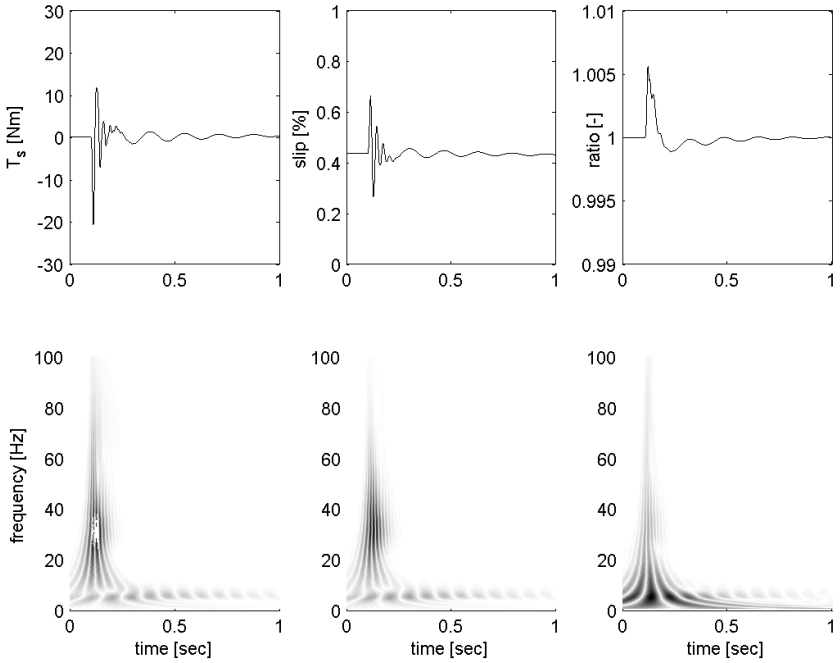

Figure 4.3: Driveline disturbances for a 15 [mm] step in road height

sponse when driving over a curb of 150 [mm], *i.e.* simulating a sidecurb, at 40 [kph] and $r_g = 2.2$ (OD). The initial engine torque during this simulation is 80 [Nm] and the slip reference is close to the optimal variator efficiency point. The analyzed slip controllers reject the low frequency part of the disturbances well. Increasing controller bandwidth results in a decrease of the first (positive) slip peak and an even larger rejection of the second (negative) slip peak. The third slip peak is hardly effected by the different controllers. These slip events are all of very short duration (< 0.1 [sec]). When open loop clamping forces are applied, the slip increases to very high values for a longer period in time. Figure 4.3 shows the secondary shaft torque T_s, the slip ν and ratio r_g for a step of 15 [mm] at the road height at 40 [km/h] vehicle speed and $r_g = 1$, using a 10 [Hz] bandwidth for both ratio and slip control. The bottom figures show the corresponding time/frequency analysis of these signals using wavelets. It can be seen that the frequency content of the torque and slip signals is relatively high, however the duration of this high frequency signals is very short, *i.e.* less than 0.1 [sec].

To represent the probability of failure of the metal V-belt due to slip, a F, v-diagram can be used [9], [103]. In this diagram, the belt slip velocity is plotted against the element normal force. Failure lines for LOW and OD are presented in [103]. Figure 4.4 depicts the simulation results for driving over a curb in the F, v-diagram for LOW and OD ratio, using open loop clamping force and a 3 [Hz] and 10 [Hz] slip control bandwidth. The failure lines are depicted by the black lines. It can be seen that the failure lines are crossed for a very short period of time when a 10 Hz slip

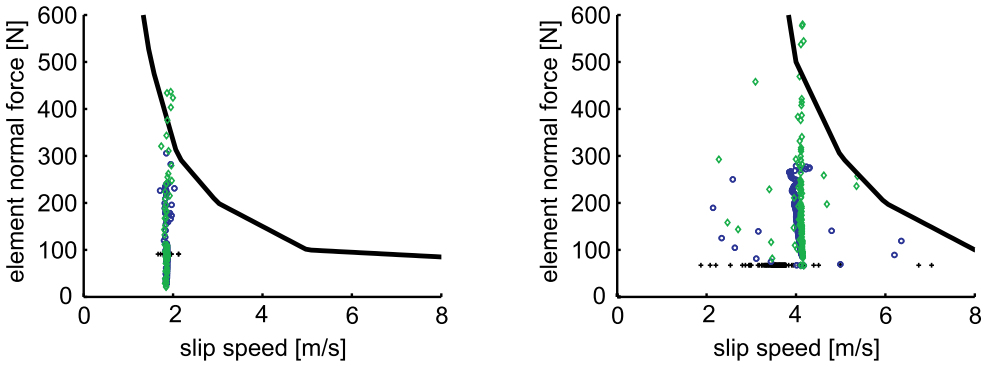

(a) LOW (b) OD

Figure 4.4: F, v-diagram for the ratios LOW and OD at optimal slip values. Without slip control (+), with a 3Hz (o) and 10Hz ($\diamondsuit$) slip controller. The sample rate of the plotted measurements is 100 Hz.

controller is implemented. This causes, according to this criterion, belt damage. For small obstacles the failure lines are not crossed. According to this criterion it is better to control slip with a low-bandwidth controller or even not to reject slip at all, i.e., use the variator as a torque fuse. However, a shortcoming of this F, v-diagram is that the effect of the time spend beyond the failure line is not taken into account. Preliminary experiments at the Empact test rig show however, that the short, high frequency slip peaks will not result in damage of the belt and variator. It is therefore assumed that short time slip events under (relatively) high clamping forces are allowed and that slip control can be applied.
As can be seen from Figure 4.3, the effect of the step disturbance on the ratio is most pronounced in the low frequency area. It can be shown that when the bandwidth of the ratio controller is reduced, the high frequency disturbances gain in amplitude. Driveability analysis shows that good disturbance reduction of the ratio and slip controller leads to better driveability [73]. The ratio reference however, must not have spectral content above 1 [Hz].
Based on these results, a desired bandwidth of 10 [Hz] is chosen for both ratio and slip control.

4.3 Control architecture

Based on the mechanical properties of the Empact CVT, for which the ratio and clamping force are decoupled by the meshing gears between the primary and secondary side epicyclic sets, and for the requirement that slip control cannot be applied under all operating conditions (at low speeds or low driveline torques), a decentralized control structure is chosen as shown in Figure 4.5. Pairing of the inputs and outputs is mainly based on the mechanical design, but will be justified by the dy-

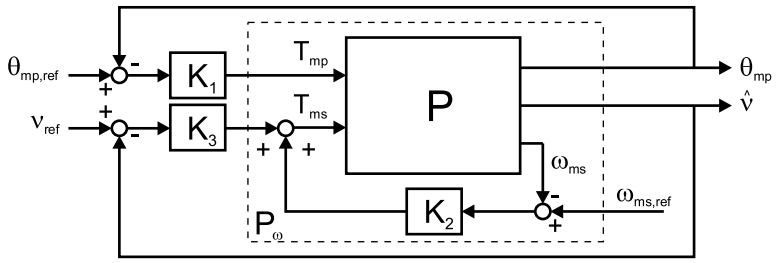

Figure 4.5: Decentralized control architecture

namic interaction analysis presented in Section 5.5. The ratio, *i.e.* θ_{mp}, will be controlled using the primary servomotor (controller K_1). In this way, the ratio control design simplifies to a co-located control design. The slip $\hat{\nu}$ will be controlled using the secondary servomotor (controller K_3). It has been one of the considerations in the mechanical design to use this servo to realize the basic clamping force in the system. The velocity ω_{ms} is fed back via the controller K_2.

There are several methods to design decentralized controllers. Here the Sequential Loop Closing (SLC) procedure [91] is used. This method has the advantage that information about controllers in other loops can be used, such that conservatism can be reduced and closed loop stability can be guaranteed. This is particulary interesting here, because the ratio and slip loop have similar bandwidth, hence the loops will have the largest effect on each other around the bandwidth frequency. The order in which the loops are closed is mainly specified by stability issues. The SLC procedure does not guarantee stability of lower level loops (the loops that are closed last) if high level loops fail [38]. Because the slip controller K_3 must be switched dependent on the operating condition, whereas stability of the ratio loop must be guaranteed at all times, the last loop closed is the slip loop. After closing this loop, no iterative design steps are taken, such that no loop information of the slip loop is used in the other loops, thus maintaining guaranteed stability. This stability condition also leads to closing the ratio loop before closing the ω_{ms} loop.

The individual controllers can either be designed by manual loop shaping or automated loop shaping techniques such as $\mathcal{H}_\infty$ or μ-synthesis. However, to be able to use these techniques, suitable models for control design are needed. The control oriented model identification will be the main subject of Chapter 5. The final control design will be presented in Chapter 6.

As mentioned in the previous section, to suppress the influence of torque delivered by the combustion engine, a feedforward compensation is applied. This compensation makes use of (3.24) and (3.25) to estimate the required clamping force. T_p is estimated from the engine torque map and torque converter characteristics by using the throttle position $\varphi_{throttle}$ and ω_s. Moreover, both the ratio and slip reference strategies also make use of these variables. The throttle position, controlled by the driver of the car, is first digitally filtered and then send to the Engine Control Mod-

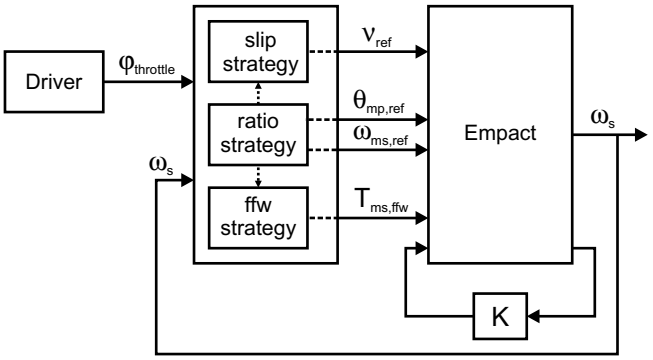

Figure 4.6: Feedforward and reference strategy

ule (ECM). Therefore, by assuming that the control feedback of the driver is very slow, this signal can be considered as a pure feedforward. The secondary shaft speed however, is a measured signal and must therefore be considered as a feedback signal. To prevent this feedback to cause instability of the closed loop system, this signal is low-pass filtered such that quasi-stationary behavior is obtained. The feedforward structure and the reference strategies are depicted in Figure 4.6.

4.4 Design limitations

The choice for a decentralized control structure leads to significant design limitations [27]. As will be shown in Section 5.5, the coupling between T_{mp} and $\hat{\nu}$ is relatively large compared to the coupling between T_{ms} and θ_{mp}. Hence, if the bandwidth of the ratio loop is increased beyond that of the slip loop, the strong interaction will result in a disturbance on this latter loop [26]. In the measurement setup, the slip estimation is contaminated with a high level of measurement noise. This leads to a significant bandwidth limitation for this loop. Due to this bandwidth limitation, the disturbance on the slip loop coming from the ratio loop cannot be attenuated. Because this disturbance of the slip is unacceptable, the bandwidth of the ratio loop is chosen below the bandwidth of the slip loop.
In many of the cases where inherent design limitations are present, these can be overcome by using a multivariable control design. Although this type of control is not applicable in a straightforward manner in the Empact CVT due to the switching requirement, the improvement that could be achieved with MIMO is investigated in Section 6.1.3.

Chapter 5

Control oriented identification

In order to solve the control problem, a model of the system to be controlled must be known. Although a (nonlinear) model is available for simulation purposes, in order to design the decentralized LTI controllers, also an approximate, linear plant model that describes the frequency domain characterization of the system is required [91], [37], [115], [3]. Gevers [31] states that "the best way to evaluate the quality of the plant approximation $\hat{P}$ is to test it under the experimental conditions under which the plant P is due to operate, *i.e.* in closed loop with the to be designed controller. For the same reason, it should ideally be identified under those same feedback conditions. This is of course impossible since knowledge of the model is required to design the controllers". Therefore, iterative model identification and control design must be used to approximate the final experimental conditions in successive steps. In this way, the uncertainty in the frequency range of importance for the design of the successive controllers can be reduced. Furthermore, in the presence of noise, closed loop identification leads to less conservative control designs than open loop identification [117].

From the dynamical analysis of the system, described in Chapter 3, it can be expected that the input-output behavior of the system depends significantly on the ratio and slip in the system [49]. The nonlinear behavior requires the identification to be carried out in closed loop. In this way the system can be linearized in or around a certain operating point, thereby minimizing the disturbances due to the nonlinearities.

The purpose of control oriented models is to describe the relevant input-output behavior of the system. There are several methods to obtain such models in a closed loop environment. Manual loop shaping, data-driven control design [55] and Quantitative Feedback Theory [37], [115] are control design methods that can handle models described with frequency domain data. Automated control design techniques like $\mathcal{H}_\infty$ however, require a preferably low order, linear and time invariant

(LTI) description of the system in state space or a transfer function in the Laplace domain. A variety of techniques is available to arrive at an approximating LTI description, for instance prediction error methods [63], subspace system identification [106], [105], maximum-likelihood (ML) identification [65] or approximate realization techniques [85], [14]. Because for the experimental setup step and pulse excitation signals have shown to give reproducible responses, the latter technique proves to give good results.
Due to the high level of noise and disturbances in the experimental setup, the quality of the system approximations is fairly low. Therefore, the simulation model is used to obtain the plant descriptions and perform control design. These controllers are then implemented at the experimental setup. Time domain validation using this experimental setup is shown throughout this chapter.
The identification experiment or input design is described in Section 5.1. Identification for pulse data is presented in Section 5.2. The closed loop identification procedure is described in Section 5.3, whereas Section 5.4 describes the results of this iterative identification and control design procedure on the simulation model. Next an interaction analysis of the identified plant is given in Section 5.5. This forms the basis for the final ratio and slip control design, discussed in Chapter 6.

5.1 Identification experiment design

Several tests were carried out to design the final identification procedure. Various types of identification signals were used in these tests, e.g. random noise, swept sine, multiple sine, pseudo random binary sequence (PRBS), step and pulse excitation signals. Each response was analyzed using an appropriate method to obtain a plant estimation. In the simulation environment, all these identification experiments achieved similar results. However, using data from the experimental setup a significant difference in plant approximation was visible, due to the high level of noise and disturbances. It turned out that the pulse excitation achieved the best predictable and reproducible results for the time response of the system. With this type of signal, a relatively high amplitude can be used without overheating the servo motors, thereby achieving a good signal to noise ratio and reducing the effects of stick due to friction. Furthermore, as will be described in Section 5.3, the identification of the slip dynamics is initially performed without slip feedback controller. Pulse excitation in this case has the advantage that the system stays close to the operating point and returns to this operating point. An additional advantage of pulse excitation in a simulation environment is, that the calculation of the response requires significantly less processing time than with a noise or other persistently exciting excitation signal.
The ideal pulse excitation for identification is an impulse. The spectral content of this signal is very broad. However, using the impulse response for system identifica-

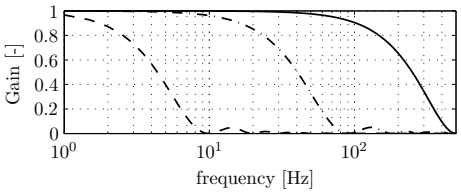

Figure 5.1: Power spectra of 1-sample pulse (-), 10-sample pulse (-.) and 100-sample pulse (- -) at 1000 [Hz] sampling frequency.

tion is not applicable in practice. The discrete impulse, a pulse of one sample width, is often used to approach the impulse excitation. Nevertheless, to put enough energy in the system, a very high amplitude of the excitation signal would be required. The step excitation, *i.e.* an infinitely broad pulse, has a high energy already at low amplitudes. A disadvantage of this signal is, that the spectral content is narrow. Using a pulse excitation with a duration of several samples can be a tradeoff between the amplitude and spectral content requirement [44]. Figure 5.1 shows the power spectrum of pulse signals of 1, 10 and 100 samples width at a sampling frequency of 1000 [Hz]. The -20 [dB] crossover amplitude (gain=0.1 [-]) is usually taken as the minimum amplitude for proper system identification results. A 100-sample pulse will therefore give good results up to 8 [Hz]. A step response would only obtain good results below 1.5 [Hz]. In the final tests, pulses with different durations and amplitudes are used.

An advantage of pulse responses is that a large number of identical identification experiments can be performed in relatively little time. By averaging the measured responses, typically over 50, the influence of disturbances and noise on the data can be minimized. Pre-treatment of measurement data is applied to obtain suitable data for system identification algorithms. Measurements which are completely out of range with respect to other measurements, are removed from the data set. High frequent measurement noise is reduced by low pass filtering. Because this filtering is performed off-line, it can be applied forward and reverse, such that it causes no additional time delay in the signal. Drifts and slow variations do not average out because of their low frequency behavior, hence they will cause model errors in the low frequency range. Therefore trend correction is applied to remove these low-frequency disturbances from the data.

To get a full description of the system, pulse response experiments are performed in different operating points, both using the simulation model and the experimental setup. To analyze the linearity of the estimated system in a certain operating point, different pulse amplitudes must be analyzed. The pulse excitation must be small enough to keep the system close to the operating point.

In all identification tests, the sampling frequency was set to 1000 [Hz]. Analog anti-aliasing filters are incorporated in the data acquisition system.

5.2 Approximate realization using pulse responses

An appropriate method to estimate linear IO-responses from pulse responses is approximate realization. This method constructs a discrete system $\mathcal{H}(A, B, C, D)$

$$x_{k+1} = Ax_k + Bu_k \tag{5.1}$$

$$y_k = Cx_k + Du_k \tag{5.2}$$

from the system Markov parameters directly from the time response data obtained from impulse responses [36], [56]. Van Helmont *et al.* [104] introduced a modification of this algorithm to use step responses instead of impulse responses [85]. Trudnowski *et al.* [96] and Kamwa *et al.* [44] describe a transition of this method to a pulse excitation. Basically, they assume that the tail of the pulse response ($y(t > a)$ where y is the measured response and a is the pulse width) is the impulse response of a fictitious linear system $\{\tilde{A}, \tilde{B}, \tilde{C}\}$. This system is diagonalized according to $\{\Lambda, T^{-1}\tilde{B}, \tilde{C}T\}$. Here $\Lambda = T^{-1}\tilde{A}T$ is a diagonal matrix containing the system eigenfrequencies on the diagonal. These eigenfrequencies correspond to the eigenfrequencies of the actual system. By writing this system and the pulse response as partial-fraction expansions, the residues of the actual system can be expressed in the residues of the fictitious system. A shortcoming of this method is that the obtained system is expressed in complex algebra. In the identification procedure, as described in Section 5.3, the input sensitivity of the plant will be estimated. In the proposed method it is assumed that the direct feedthrough D matrix of the system is zero, which is obviously not true for the sensitivity of a controlled mechanical system. Therefore, this method is not applicable here.
To use the pulse response in the approximate realization method, two different approaches are proposed here. The first method, called here 'impulse reconstruction', differentiates the measured response to obtain the Markov parameters and uses the Kung algorithm [56] to estimate the state space realization $\mathcal{H}$, whereas the second method, denoted as 'step reconstruction', integrates the measured response and uses the modified version of the Kung method described by Van Helmont *et al.* [104]. For identification of the simulation model, the impulse reconstruction is used, whereas for the identification in the practical environment the step reconstruction is used.

Impulse reconstruction

The impulse reconstruction approach is useful when the signal to noise ratio is very good. Due to the required differentiation of the data, noise can cause errors in the high frequency range.
For a discrete-time system, the step response matrix S_k is defined as $S_k = 0$, $k = 0, -1, -2, \ldots$ and

$$S_k = \sum_{i=1}^{k} D_i, \quad k = 1, 2, 3, \ldots \tag{5.3}$$

where D_i is the impulse response at time instance i. The pulse response matrix P_k can then be defined as

$$P_k = S_k, \qquad k = 0, 1, 2, \ldots, l \tag{5.4}$$

$$P_k = S_k - S_{k-l}, \quad k > l \tag{5.5}$$

where l is the pulse width. The Markov parameters, or the impulse response of the system, are now given by

$$D_0 = P_0 \tag{5.6}$$

$$D_k = P_k - P_{k-1}, \quad k = 1, 2, \ldots, l \tag{5.7}$$

$$D_k = \sum_{i=0}^{n} \left(P_{k-il} - P_{k-il-1} \right), \quad k > l \tag{5.8}$$

where $n = \text{floor}\left(\frac{k}{l}\right)$. The pulse response must be normalized to match the energy of an unit impulse. Using the normalized impulse response $\tilde{D}_k$, the Kung algorithm defines Hankel matrices H_E, H_A, H_B and H_C according to

$$H_E = \begin{bmatrix} \tilde{D}_1 & \tilde{D}_2 & \cdots & \tilde{D}_r \\ \tilde{D}_2 & \tilde{D}_3 & \cdots & \tilde{D}_{r+1} \\ \tilde{D}_3 & \tilde{D}_4 & \cdots & \tilde{D}_{r+2} \\ \vdots & \vdots & \ddots & \vdots \\ \tilde{D}_r & \tilde{D}_{r+1} & \cdots & \tilde{D}_{r+r} \end{bmatrix} \tag{5.9}$$

$$H_B = \begin{bmatrix} \tilde{D}_1 & \tilde{D}_2 & \tilde{D}_3 & \cdots & \tilde{D}_r \end{bmatrix}^T \tag{5.10}$$

$$H_C = \begin{bmatrix} \tilde{D}_1 & \tilde{D}_2 & \tilde{D}_3 & \cdots & \tilde{D}_r \end{bmatrix} \tag{5.11}$$

whereas H_A originates from H_E if all responses are shifted one time step upwards, *i.e.* if $\tilde{D}_j$ is replaced by $\tilde{D}_{j+1}$ for $j = 1, 2, \ldots, 2r$. The integer r is given by $r = \text{floor}(N/2)$ with N the number of samples.

The matrix H_E is decomposed using a singular values decomposition according to

$$H_E = U \Sigma V^T \tag{5.12}$$

where the eigenvector matrices U and V are orthogonal and the matrix Σ is a semi-positive definite, diagonal matrix, consisting of r singular values $\sigma_1 \geq \sigma_2 \geq \cdots \geq \sigma_r$. By selecting the system order ρ such that $\sigma_{\rho+1} \gg \sigma_\rho$, the system matrices can be obtained from

$$A = \Sigma_\rho^{-\frac{1}{2}} U_\rho^T H_A V_\rho \Sigma_\rho^{-\frac{1}{2}} \tag{5.13}$$

$$B = \Sigma_\rho^{-\frac{1}{2}} U_\rho^T H_B \tag{5.14}$$

$$C = H_C V_\rho \Sigma_\rho^{-\frac{1}{2}} \tag{5.15}$$

$$D = \tilde{D}_0 \tag{5.16}$$

where the subscript ρ denotes the first ρ columns c.q. rows of the relevant matrix.

Step reconstruction

This method is applicable for broader pulses, also in a noisy environment. The step response can be reconstructed from the pulse response by

$$S_{ki} \quad = \quad P_{ki} + P_{ki-l}, \quad k = l, l-1, \ldots, 1 \tag{5.17}$$

for $i = 1, 2, \ldots$. The step response must be normalized to match the unit step response. The system $\mathcal{H}$ can again be obtained by the above outlined procedure, but this time using modified Hankel matrices according to Van Helmont *et al.* [104]. Using the normalized step response $\tilde{S}_k$, the Hankel matrices H_E, H_A, H_B and H_C are defined according to

$$H_E = \begin{bmatrix} \tilde{S}_1 & \tilde{S}_2 & \cdots & \tilde{S}_r \\ \tilde{S}_2 - \tilde{S}_1 & \tilde{S}_3 - \tilde{S}_1 & \cdots & \tilde{S}_{r+1} - \tilde{S}_1 \\ \tilde{S}_3 - \tilde{S}_2 & \tilde{S}_4 - \tilde{S}_2 & \cdots & \tilde{S}_{r+2} - \tilde{S}_2 \\ \vdots & \vdots & \ddots & \vdots \\ \tilde{S}_r - \tilde{S}_{r-1} & \tilde{S}_{r+1} - \tilde{S}_{r-1} & \cdots & \tilde{S}_{r+r} - \tilde{S}_{r-1} \end{bmatrix} \tag{5.18}$$

$$H_B = \begin{bmatrix} \tilde{S}_1 & \tilde{S}_2 - \tilde{S}_1 & \tilde{S}_3 - \tilde{S}_2 & \cdots & \tilde{S}_r - \tilde{S}_{r-1} \end{bmatrix}^T \tag{5.19}$$

$$H_C = \begin{bmatrix} \tilde{S}_1 & \tilde{S}_2 & \tilde{S}_3 & \cdots & \tilde{S}_r \end{bmatrix} \tag{5.20}$$

whereas H_A again originates from H_E if all entries are shifted one time step upwards. Using the measured pulse response to reconstruct a step response is mostly applicable for large pulse durations. For short pulses, the estimation will give low frequency errors due to possible drift.

Impulse versus step reconstruction

To illustrate the differences between the step and impulse reconstruction, as an example these methods are applied here to estimate a second order system $\mathcal{H}(s)$ with natural frequency $f_n = 100/(2\pi)$ [Hz], relative damping $\zeta = 0.25$ [-] and low frequency gain of -20 [dB]. Figure 5.2 shows the response of this system to a unit pulse of 0.01 [sec], measured with a sampling frequency of 1000 [Hz] ($l = 10$). Random noise is added to the process output. It can be seen that the signal to noise ratio for the reconstructed impulse response is worse than for the reconstructed step response. This can also be seen from the singular values in the approximate realization procedure (Figure 5.3). The step reconstruction clearly shows two dominant system modes. For the impulse reconstruction, the singular values are much closer together. In this case there are also two dominant modes, however, a slightly higher noise level could cause the noise to be dominant over the system modes. This could result in a

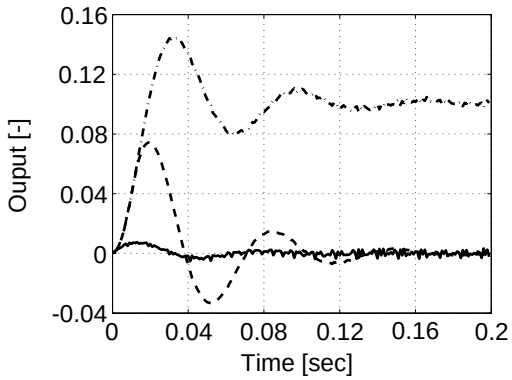

Figure 5.2: Pulse response (- -), impulse reconstruction (-) and step reconstruction (-.) at 1000 [Hz] sampling frequency.

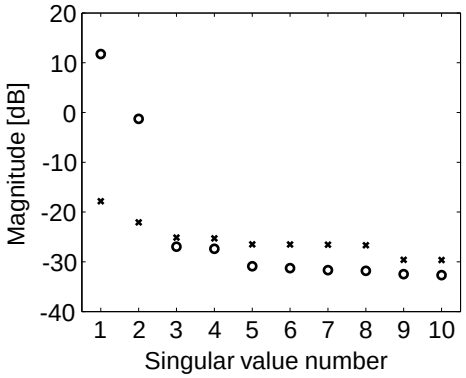

Figure 5.3: Singular values of impulse approximation (x) and step approximation (o)

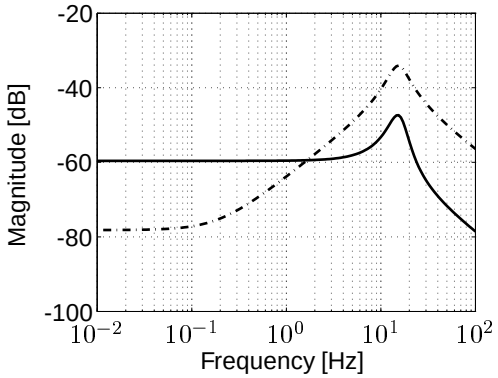

Figure 5.4: Transfer Function estimation error $|\mathcal{H}(s) - \hat{\mathcal{H}}(s)|$ of impulse approximation (-) and step approximation (-.)

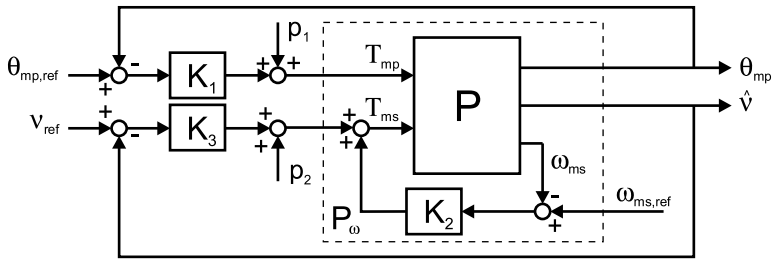

Figure 5.5: Identification setup

higher system approximation order. Figure 5.4 shows the absolute estimation error $|\mathcal{H}(s) - \hat{\mathcal{H}}(s)|$ for both methods. It can be clearly seen that for low frequencies, the step approximation performs better, whereas for the high frequencies, the impulse approximation performs better.

5.3 Closed loop identification procedure

In the closed loop environment pulse excitations p_1 and p_2 are added to the corresponding controller outputs (see Figure 5.5). In this way an estimation can be obtained for the sensitivity S and the process sensitivity PS. In the approximate realization, these two transfer function matrices will be estimated simultaneously by stacking the plant input u and output y on top of each other. The realization is then applied to the pulse response matrix

$$P_k = \begin{bmatrix} \tilde{y}_{11_k} & \tilde{y}_{12_k} \\ \tilde{y}_{21_k} & \tilde{y}_{22_k} \\ \hline \tilde{y}_{31_k} & \tilde{y}_{32_k} \\ \tilde{y}_{41_k} & \tilde{y}_{42_k} \end{bmatrix} \tag{5.21}$$

where $\tilde{y}_{ji_k}$ is the normalized response at time k of the j-th output to a pulse p_i of the i-th input ($i = 1, 2$). With a proper selection of the outputs $\tilde{y}_{ji_k}$, the resulting system $\mathcal{H}$ can be defined as

$$\mathcal{H} = \begin{bmatrix} S \\ \hline PS \end{bmatrix} \tag{5.22}$$

Hence, the plant P can be directly obtained from $\mathcal{H}$ by $P(z) = PS(z)S^{-1}(z)$, under the assumption of invertibility of S.

One problem in closed loop identification it that, to design the controller used in the identification procedure, an initial plant description must be available. To control the ratio of the CVT, co-located control of the primary servomotor position θ_{mp} is used. Then it is straightforward to design a stabilizing controller K_1 and the lack of a plant description is not a problem. To design a slip controller without a proper plant description, however, is not straightforward. This problem can be avoided by

first applying open loop identification in the stable slip region, *i.e.* where the slope of the traction curve $\mu' >> 0$ (small slip values). In this case excessive slip can be prevented by applying an open loop torque T_{ms} at the secondary servomotor. Based on this initial plant estimation, a stabilizing slip controller can be designed and the identification can be performed in closed loop from this point. The successive identification steps for this procedure are described next.

1st identification step

In this step the ratio loop is closed using controller K_1, whereas the other loops are open, *i.e.* $K_2 = 0$ and $K_3 = 0$. The outputs $\tilde{y}_{1i}$ to $\tilde{y}_{4i}$ are defined as T_{mp}, T_{ms}, θ_{mp} and ω_{ms} respectively. Here, the goal is to find a description of plant P from T_{mp} and T_{ms} to θ_{mp} and ω_{ms} to design the second controller K_2.

2nd identification step

In this identification step controller K_2 is implemented, $K_3 = 0$ and K_1 is unchanged. Now by using the slip $\hat{\nu}$ as output $\tilde{y}_{4i}$, an estimate for the plant P_ω, denoted by the dashed box in Figure 5.5, can be obtained and used to design a stabilizing slip controller K_3.

3rd identification step

In this step all control loops are closed using the controllers designed in the previous steps. Now an iterative procedure is used to obtain plant estimations for slip values close to the maximum efficiency level, *i.e.* close to the top of the traction curve where $\mu' = 0$. In each step the plant P_ω is estimated and stability of the resulting closed loop system is evaluated. If necessary, the controller gain is adapted or a new controller is designed. This estimation and control adaptation is repeated until a satisfactory broad operating range is covered.

5.4 Closed loop identification results

This section presents the results of the identification procedure applied to the simulation model. Controllers designed based on these results are implemented in the simulation model as well as in the experimental setup. The experimental results are used to validate the time response of the simulation model.
Operating points in identification step 1 and 2 are defined by a geometric ratio r_{g_0}, secondary actuation torque T_{ms_0}, primary shaft speed ω_{p_0} and driving torque T_{p_0}. Operating points in identification step 3, *i.e.* when using a slip controller, are defined by r_{g_0}, ω_{p_0}, T_{p_0} and the nominal slip ν_0.

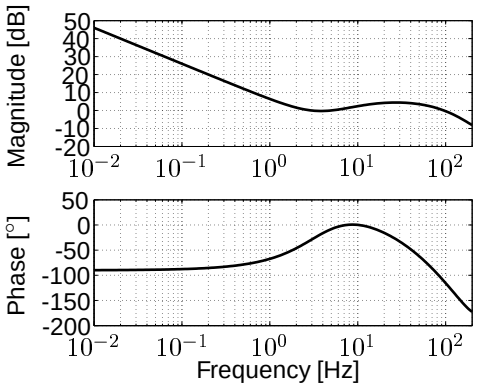

Figure 5.6: Bode plot of K_1

5.4.1 1st identification step results

The goal in this step is to find a suitable model of plant P in order to design the controller K_2.
Based on the physical properties of the plant, it is expected that the plant P_{11} has a very large damping, resulting in a -1 slope for low frequencies. P_{11} furthermore shows a mass-decoupling of the actuation system around 10-15 [Hz]. The controller K_1 used in this identification step is therefore chosen as a lead-lag controller. The pole of the lag part is placed at the origin, such that maximal integral control is achieved. The lead part is designed such that a minimum phase loss around 10-15 [Hz] is achieved, obtaining large stability margins. Furthermore, to reduce the effect of measurement noise, a 2^{nd} order lowpass Butterworth filter at 30 [Hz] is implemented. Figure 5.6 shows the transfer function of this controller.

Pulse responses

The gray lines in Figure 5.7(a) depict 25 experimentally measured responses of the primary servomotor position θ_{mp} to a 10 sample pulse with an amplitude of 1.5 [Nm] at the primary servomotor torque T_{mp}. The average of these responses is shown by the black line. The operating point is defined by $r_{g_0} = 1.0$, $T_{ms_0} = 0.2$ [Nm], $\omega_{p_0} = 200$ [rad/s] and $T_{p_0} = 50$ [Nm]. It can be seen that, due to static friction in the system, the responses vary slightly and the low frequency behavior is influenced. Figure 5.7(b) depicts the responses to different pulse sizes in the same operating point. Due to the relatively high level of Coulomb friction with respect to the pulse amplitude of 0.5 [Nm], this response is influenced most by the friction. Higher amplitude pulses achieve a better signal to noise ratio and are therefore less influenced by the static friction. Analysis of the responses at higher pulse amplitudes shows that the local behavior of the system is linear. Figure 5.7(c) and 5.7(d) show the response of the simulation model in the same operating point, using the same pulse excitation signals. The first figure (c) shows the response when the complete friction models as described in Section 3.4 are implemented, whereas the latter

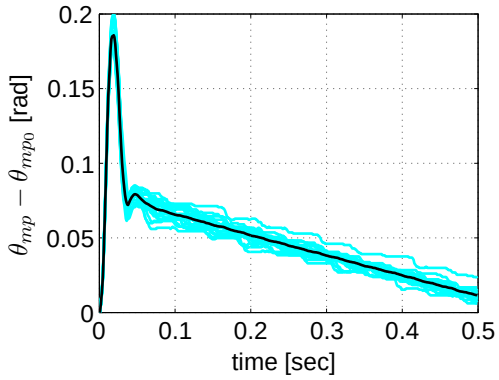

(a) Measured pulse responses

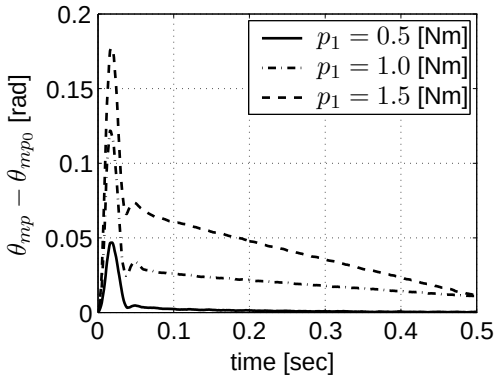

(b) Averaged measured pulse responses

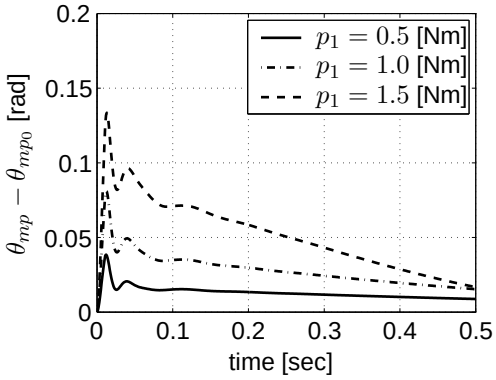

(c) Simulation with complete friction model

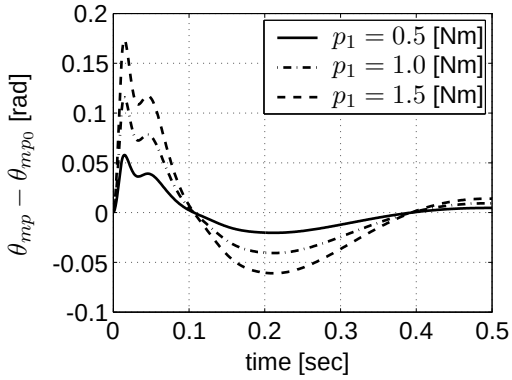

(d) Simulation with viscous friction model

Figure 5.7: Measured and simulated pulse responses from p_1 to θ_{mp} ($\hat{r}_{g_0} = 1.0$, $l = 10$ [samples] $= 0.01$ [sec])

figure (d) shows the response when only the linear viscous part of the friction model is implemented. It can be seen that the responses with the complete friction model show qualitatively the same behavior as the experimental setup, however amplitudes and low frequency response differ significantly. When only viscous friction is used, the system shows a linear behavior, for both low and high frequencies. Figure 5.8 shows the same analysis for the response of the secondary servo velocity ω_{ms} to a pulse at the secondary servomotor torque T_{ms}. Here, the operating point is defined by $r_{g_0} = 0.5$, $T_{ms_0} = 0.2$ [Nm], $\omega_{p_0} = 200$ [rad/s] and $T_{p_0} = 50$ [Nm]. The static friction has only small effect on these responses.
For both the primary and secondary pulse response, the simulation model predicts the behavior of the experimental setup very well. The shape of the response of ω_{ms} indicates a mass-spring-damper behavior, which is expected from the system design. This is also supported by the dynamical analysis presented in Appendix B.4, which shows that no rigid body mode is present at the secondary actuation side. The primary actuation side also acts like a mass-spring-damper system, which is inherent behavior of the position feedback on this servomotor.

System description

Because the behavior of the system with and without static friction is at least qualitatively similar (only the low frequency behavior is contaminated by the static friction), the responses obtained with only viscous friction are used for system approximation. Thorough analysis shows that the average of a large number of plant estimations from responses with static friction approaches the estimation with just viscous friction.
The concept of approximate realization, as described in Section 5.2, is applied to derive the LTI models in different operating points. The impulse reconstruction is used, because the noise and disturbance levels are small when using simulation data. Figure 5.9(a) shows the reconstructed and normalized impulse response of θ_{mp} for three different operating points. As expected, no high frequent noise amplification due to differentiation is visible. The response shows only minor dependency on the CVT ratio. Figure 5.9(b) shows the Hankel singular values of the complete system $\mathcal{H}$. Normally the system order is chosen where a large decay in magnitude between two successive singular values occurs. However, no clear decay is visible here. A too large systems order would influence the controllers order when using automated control design techniques. Because here the controllers are designed using manual loop shaping, the system order introduces no limitations on the designed controllers. Typically, an order of 20 is chosen, such that the singular values larger than -20 [dB] are taken into account. In this way the pulse response is approximated with a relative error smaller than 0.1 [%].
Figure 5.10 shows the resulting sensitivity $S_{11} = (I + P_{11}K_1)^{-1}$ for three different ratios. It can be seen that this system is stable with a bandwidth between 2 and

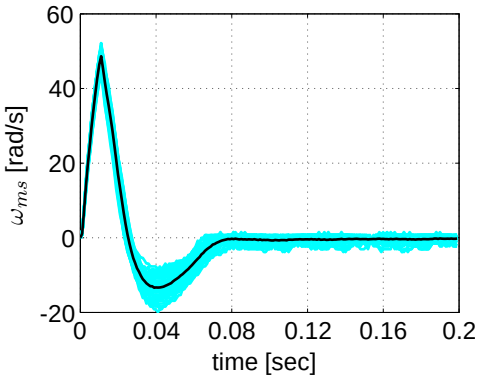

(a) Measured pulse responses

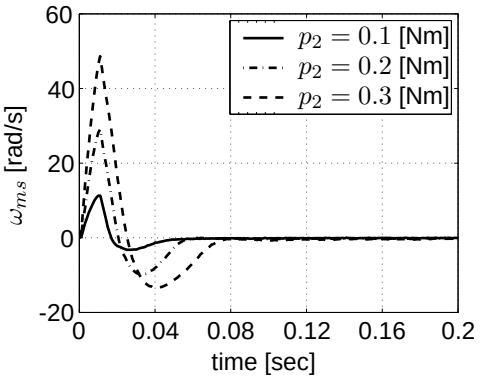

(b) Averaged measured pulse responses

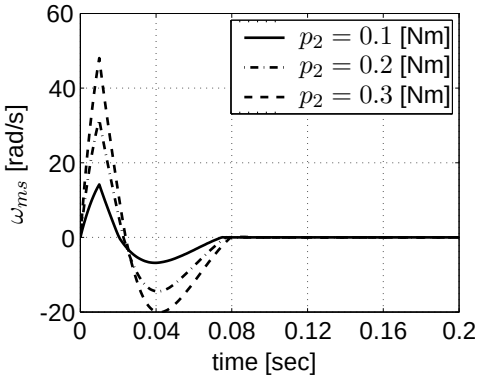

(c) Simulation with complete friction model

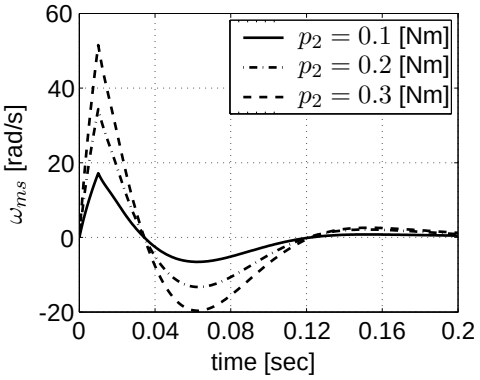

(d) Simulation with viscous friction model

Figure 5.8: Measured and simulated pulse responses from p_2 to ω_{ms} ($\hat{r}_{g_0} = 0.5$, $l = 10$ [samples] $= 0.01$ [sec])

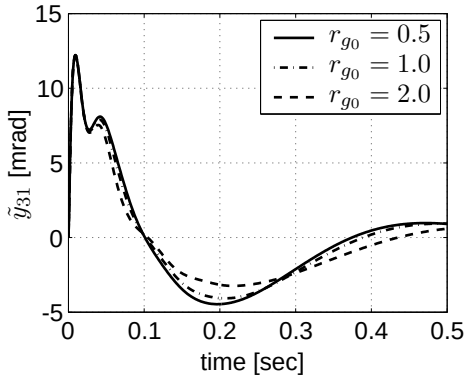

(a) Normalized impulse reconstruction $\tilde{y}_{31}$

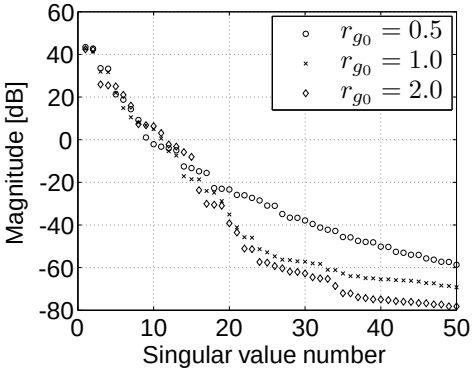

(b) Hankel Singular values

Figure 5.9: Realization procedure results for system $\mathcal{H}$

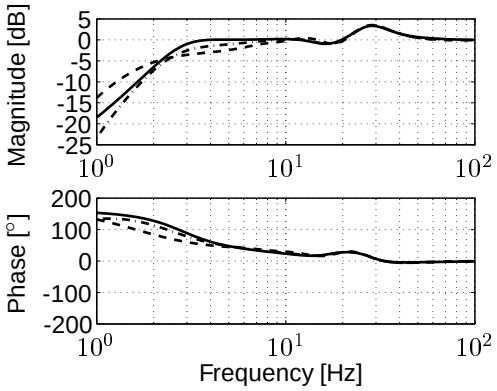

Figure 5.10: Sensitivity S_{11} at $r_g = 0.5$ (-), $r_g = 1$ (-.) and $r_g = 2$ (--)

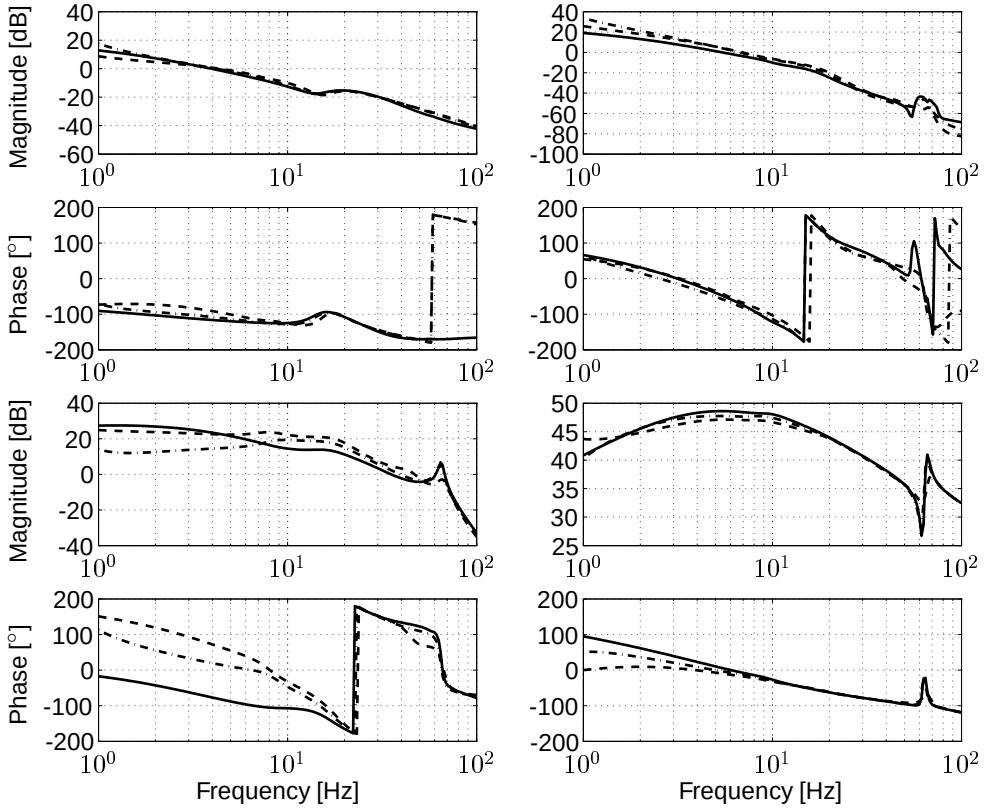

Figure 5.11: plant P estimation at $r_g = 0.5$ (-), $r_g = 1$ (-.) and $r_g = 2$ (--)

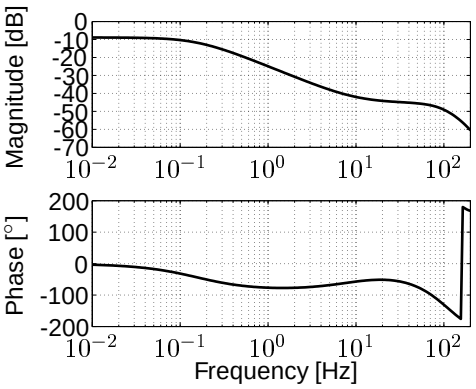

Figure 5.12: Bode plot of K_2 designed in step 1

3 [Hz], depending on the CVT ratio. S_{22} is not shown here, because $K_2 = 0$ and $K_3 = 0$, hence $S_{22} = 0$. Figure 5.11 shows the corresponding plant estimations. In the first diagonal element P_{11}, a strongly damped mass decoupling of the primary actuation can be seen around 20 [Hz]. The secondary actuation system acts indeed as a mass-spring-damper, as can be seen by the +1 slope at low frequencies in P_{22}, which tends towards a -1 slope for higher frequencies. Analysis shows that this roll-off is due to the decoupling of the primary actuation side by the pulley and the belt stiffness. This introduces two strongly damped poles around 8 [Hz], which also cause the phase to decrease already at low frequencies. Furthermore, an (anti-)resonance is visible at 65 [Hz], which is due to the secondary servo and chain stiffness.

Control design

Based on these results, the secondary servo controller K_2 is designed using the equivalent plant G_{22}, *i.e.* the plant transfer function from input 2 to output 2 when loop 1 is closed. For the ω_{ms} loop this equivalent plant is defined by $G_{22} = P_{22} - P_{21}K_1S_{11}P_{12}$. A lead-lag controller with an aimed closed loop bandwidth of 20 [Hz] is chosen. As it is not desired to control the position of the secondary actuator, no integral action is used. The resulting controller K_2 is shown in Figure 5.12. Stability of the resulting closed loop system is checked by studying the open loop transfer function of the equivalent plants. For the ratio control loop, the equivalent plant is defined by $G_{11} = P_{11} - P_{12}K_2S_{22}P_{21}$. Figure 5.13(a) and 5.13(b) show the open loop transfer functions of the equivalent plants $G_{11}K_1$ and $G_{22}K_2$ respectively. Both transfer functions show stable closed loop behavior. Analysis of the equivalent plants shows that the influence of the secondary loop on P_{11} and the influence of the primary loop on P_{22} is very small, hence no two-way interaction is present in the plant. Section 5.5 will give a more detailed interaction analysis of the final closed loop plant.

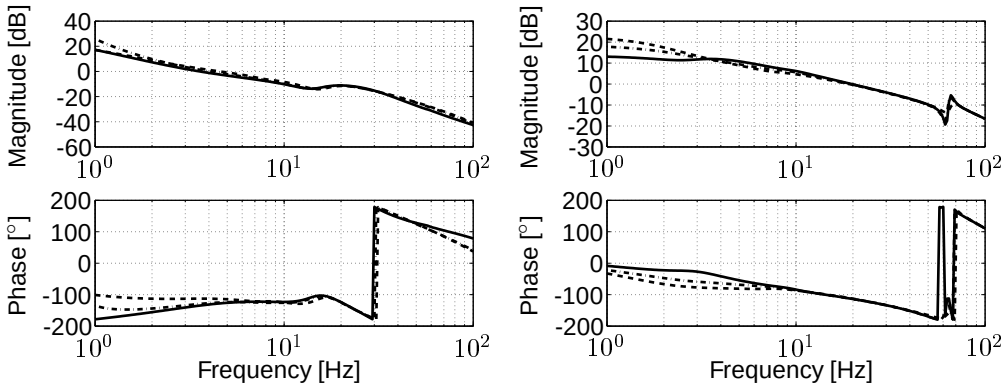

(a) $G_{11}K_1$ (b) $G_{22}K_2$

Figure 5.13: Open loop transfer function at $r_g = 0.5$ (-), $r_g = 1$ (-.) and $r_g = 2$ (- -)

5.4.2 2nd identification step results

A similar identification as described in the previous section is now repeated, but this time on the modified plant P_ω with the controllers K_1 and K_2 implemented and the slip as the plant output variable. The goal in this step is to obtain a plant description in order to design a first slip controller.

Pulse responses

Because of the small interaction in the first and second loop, the response of θ_{mp} to a pulse on the primary input will be similar to the response shown in Figure 5.7. Figure 5.14(a) shows 50 measured responses of the variation of the slip around its nominal value $\hat{\nu} - \hat{\nu_0}$ to a 100 sample pulse with amplitude 0.4 [Nm] at the secondary servomotor input. The slip is filtered using an zero-phase 8^{th} order Butterworth filter with a cut-off frequency of 25 [Hz]. Figure 5.14(b) shows the corresponding simulation results. The operating point is defined by $r_{g_0} = 1.0$, $T_{ms_0} = 0.2$ [Nm], $\omega_{p_0} = 200$ [rad/s] and $T_{p_0} = 100$ [Nm] ($\hat{\nu_0} \approx 0.8$ [%]). Although the disturbances of the slip measurement are very large, the amplitude and the shape of the averaged, measured response qualitatively correspond very well to the simulation results. To further validate the response, Figures 5.14(c) and 5.14(d) show the secondary servo torque during these pulse excitations. Here, only low frequency offset due to friction is present. Without a slip controller it is very difficult to obtain better responses of the slip. Therefore, first a stabilizing slip controller will be designed using the plant approximation based on the simulation data.

System description

Figure 5.15 shows the resulting plant P_ω at three different ratios. Recall that $P_{\omega_{11}}$ is the ratio transfer function and $P_{\omega_{22}}$ is the slip transfer function. The feedback of

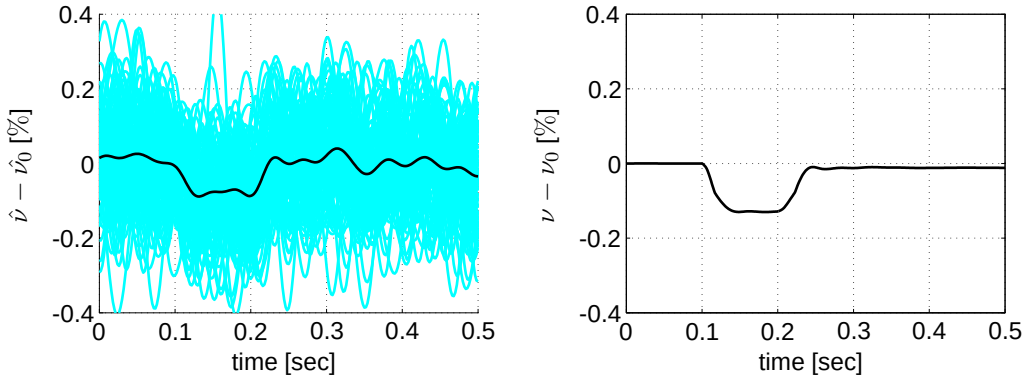

(a) Measured pulse responses of $\hat{\nu} - \hat{\nu_0}$

(b) Simulated pulse responses of $\hat{\nu} - \hat{\nu_0}$

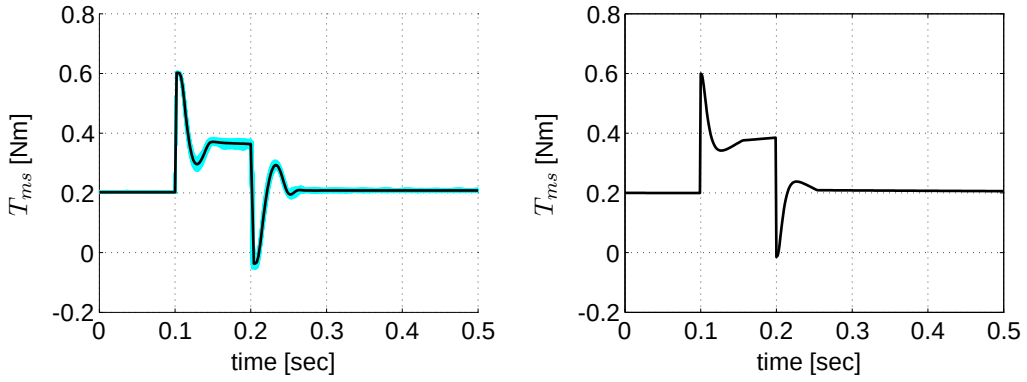

(c) Measured pulse responses of T_{ms}

(d) Simulated pulse responses of T_{ms}

Figure 5.14: Measured and simulated pulse responses from p_2 ($l = 100$ [samples])

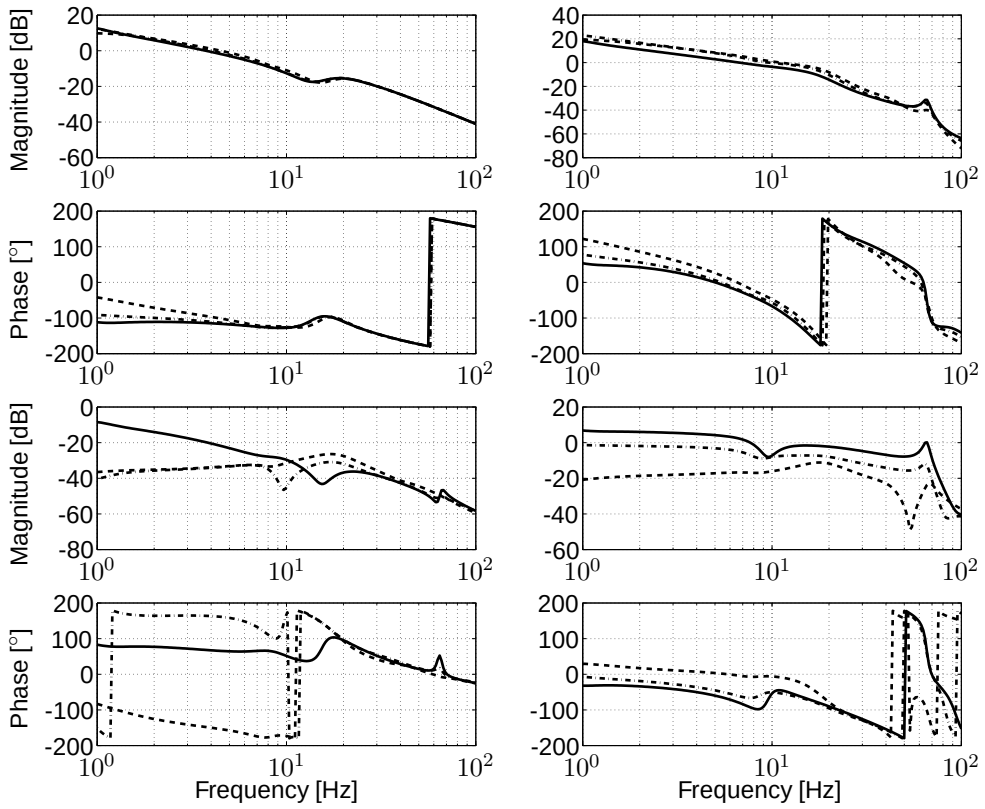

Figure 5.15: P_ω estimation at $r_g = 0.5$ (-), $r_g = 1$ (-.) and $r_g = 2$ (--)

ω_{ms} adds extra damping to the system, mainly in $P_{\omega_{22}}$. The two strongly damped poles around 8 [Hz] also lead to a large phase decay here. Around 9 [Hz] also a zero-pole combination is present due to the torque converter stiffness and driving motor inertia. Only three operating points are described here, but the analysis is carried out for multiple ratio and slip values covering the complete operating range.

Control design

Based on these results, a slip controller can be designed for each operating point on the equivalent plant $G_{\omega_{22}} = P_{\omega_{22}} - P_{\omega_{21}} K_1 S_{\omega_{11}} P_{\omega_{12}}$ where $S_{\omega_{11}} = (I + P_{\omega_{11}} K_1)^{-1}$, taking the interaction into account. Note that $G_{\omega_{22}}$ equals the process sensitivity $PS_{\omega_{22}}$ obtained in the approximate realization of system $\mathcal{H}$. Because the identification in step 3 is performed in or close to a certain operating point, the closed loop system needs to be stable, however not robustly stable for all operating points. A lag-controller is sufficient to meet this requirement. Different gains are chosen for different operating points, such that the resulting open loop cross-over is between 1 and 3 [Hz]. Figures 5.16(a) and 5.16(b) show the open loop transfer functions of the equivalent plants $G_{\omega_{11}} K_1$ and $G_{\omega_{22}} K_3$ for the plants shown in Figure 5.15. Here $G_{\omega_{11}} = P_{\omega_{11}} - P_{\omega_{12}} K_3 S_{\omega_{22}} P_{\omega_{21}}$ and $S_{\omega_{22}} = (I + P_{\omega_{22}} K_3)^{-1}$. The phase and gain

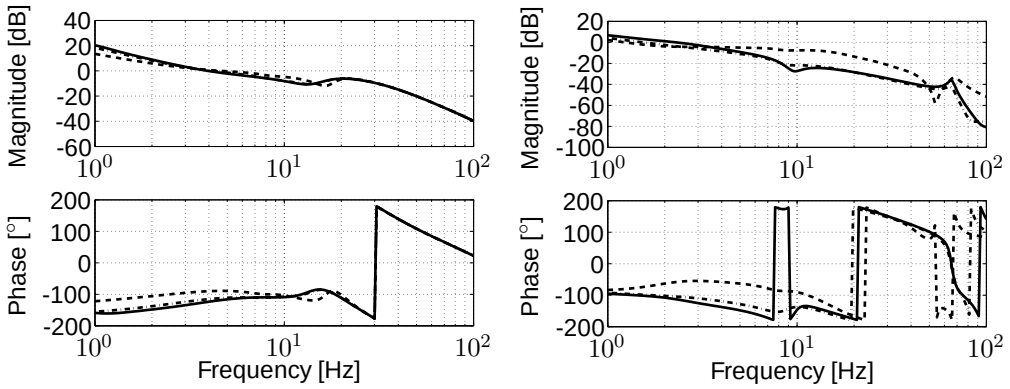

(a) $G_{\omega_{11}} K_1$ (b) $G_{\omega_{22}} K_3$

Figure 5.16: Open loop transfer function at $r_g = 0.5$ (-), $r_g = 1$ (-.) and $r_g = 2$ (--)

margins are large enough to cope with some uncertainties.

5.4.3 3rd identification step results

Using K_1, K_2 and K_3 from the previous sections, the plant P_ω is again identified in closed loop. Stable behavior at high slip levels close to or at the optimal efficiency level can now be obtained. The goal in this step is to find a plant approximation for a satisfactory broad operating range. Section 5.5 presents an interaction analysis based on this plant estimation. The design of robustly stabilizing ratio and slip controllers, using this estimation, is presented in Chapter 6.

Pulse responses

The use of a slip controller has significant benefit for the pulse response, as can be seen from the response in Figure 5.17. This figure shows the response of the variation of the slip $\hat{\nu} - \hat{\nu_0}$ to a 100 sample pulse with amplitude 0.4 [Nm]. The operating point is defined by $r_{g_0} = 1.0$, $T_{ms_0} = 0.3$ [Nm], $\omega_{p_0} = 200$ [rad/s] and $\hat{\nu_0} = 1$ [%]. The slip is again filtered using a zero-phase 8^{th} order Butterworth filter with a cut-off frequency of 25 [Hz]. Although the noise level on the slip is still significant, the behavior of the system shows more reproducible behavior than without slip control. The effects of friction are reduced by the noisy actuation signal, compared to the results in step 2. Again the simulation results show a qualitatively similar behavior for both the slip in the system and the actuation torque.

System description

Figure 5.18 shows the estimations of the plant P_ω for $r_g = 1$ at different slip levels. It can be seen that $P_{\omega_{11}}$, $P_{\omega_{12}}$ and $P_{\omega_{21}}$ do not show any significant dependence on the slip level in the system. However, for $P_{\omega_{22}}$ it is clear that the process gain increases

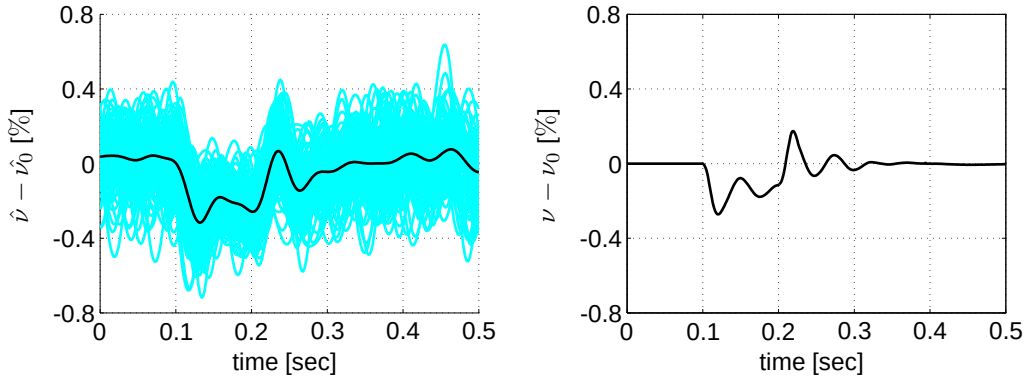

(a) Measured pulse responses of $\hat{\nu} - \hat{\nu_0}$

(b) Simulated pulse responses of $\hat{\nu} - \hat{\nu_0}$

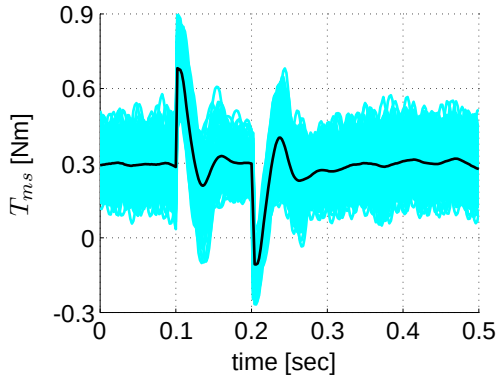

(c) Measured pulse responses of T_{ms}

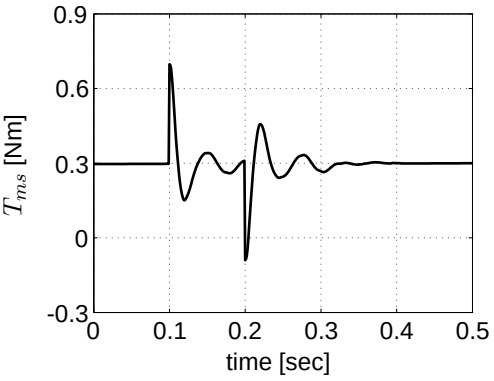

(d) Simulated pulse responses of T_{ms}

Figure 5.17: Measured and simulated pulse responses with slip control from p_2 ($l = 100$ [samples])

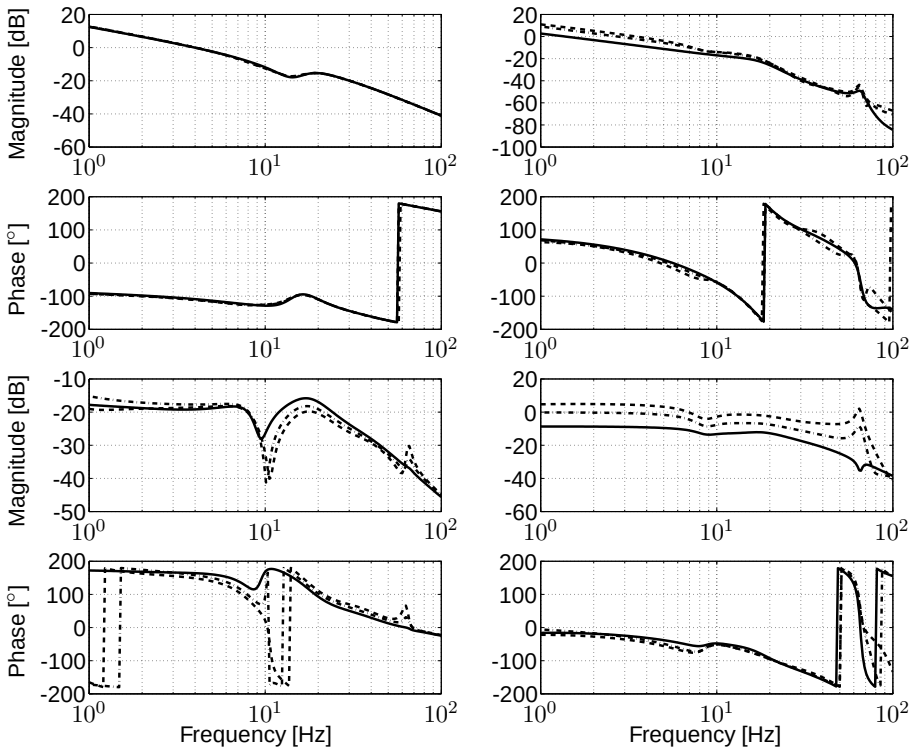

Figure 5.18: Plant P_ω obtained using closed loop plant identification at $r_g = 1$ at $\nu = 0.5$ (-), $\nu = 0.75$ (-.) and $\nu = 1$ (--)

and the damping of the resonances decreases with increasing slip level. This is expected, because of the inherent behavior of the more or less inversely proportional relation between slip and actuation torque, i.e. $\nu \to 0$ as $T_{ms} \to \infty$ and $\nu \to \infty$ as $T_{ms} \to 0$.

Figure 5.19 shows the estimations of P_ω for three different ratios at the slip level where optimal efficiency is reached, whereas Figure 5.20 shows the corresponding identified sensitivity. It can be seen that, at these optimal efficiency slip values, the gain of $P_{\omega_{22}}$ hardly depends on the ratio r_g. However $P_{\omega_{12}}$ shows large variations for different ratios. As will be shown in Section 5.5, the 2-way interaction is limited and no complications for control design are expected due to this variation.

5.5 Interaction analysis

To study the diagonal dominance of a system and to choose pairings, the frequency dependent Relative Gain Array (RGA) defined by $\Lambda(G) = G \times (G^{-1})^T$ is commonly used [91]. For a 2x2 system with elements g_{ij} the RGA is given by

$$\Lambda(G) = \begin{bmatrix} \lambda_{11} & 1-\lambda_{11} \\ 1-\lambda_{11} & \lambda_{11} \end{bmatrix} \quad ; \quad \lambda_{11} = \frac{1}{1 - \frac{g_{12}g_{21}}{g_{11}g_{22}}} \tag{5.23}$$

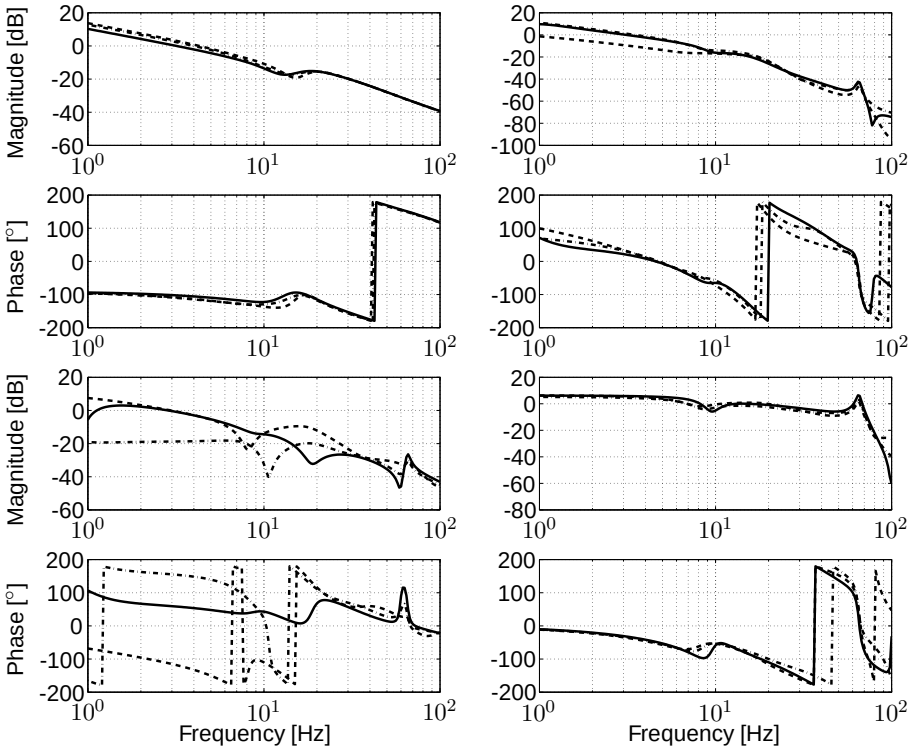

Figure 5.19: Plant P_ω obtained using closed loop plant identification at $r_g = 0.5$ (-), $r_g = 1$ (-.) and $r_g = 2$ (--) for optimal efficiency slip values

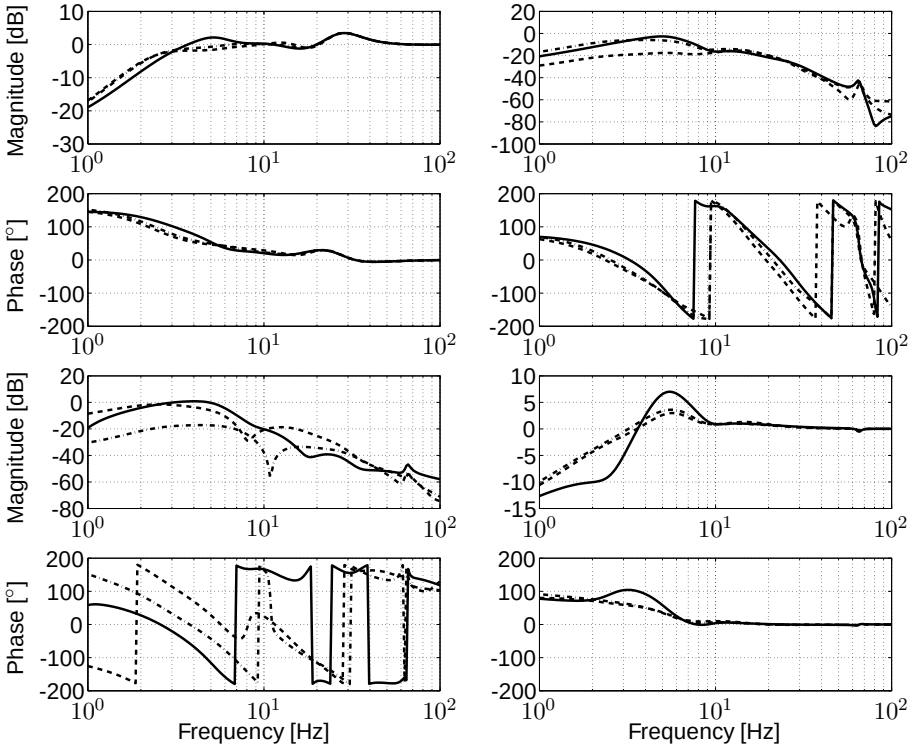

Figure 5.20: Closed loop sensitivity estimation at $r_g = 0.5$ (-), $r_g = 1$ (-.) and $r_g = 2$ (--) for optimal efficiency slip values

When $g_{11}g_{22} \gg g_{12}g_{21}$, the plant is diagonally dominant and $\Lambda(G) = I$. Physically, λ_{11} shows how much the closing of one loop affects the other loop. If λ_{11} is close to 1 at all frequencies, this means that the cross gains, *i.e.* the gains from u_1 to y_2 and from u_2 to y_1, are unaffected by closing the other loops. Pairings which result in $\Lambda \approx I$ are therefore preferred.
The RGA $\Lambda(P_\omega) = P_\omega(s) \times P_\omega^{-1}(s)^T$ for plant P_ω is shown in Figure 5.21. It can be seen that the (1,1)-entry λ_{11} of Λ is close to unity for all frequencies, indicating diagonal dominance and a good choice of pairing. At this point it is interesting to study the RGA of a variator without actuation mechanism, i.e. a variator where the clamping forces are directly applied to the moveable pulley sheaves. For this analysis the disturbance model is used as described in Section 4.2. When the same outputs are chosen as for plant P_ω, i.e. x_p and ν, diagonal dominance significantly depends on the chosen inputs. For inputs $F_{p,act}$ and $F_{s,act}$ the RGA is shown in Figure 5.22(a). It can be seen that no diagonal dominance is achieved. When combining the inputs to $F_{p,act} - F_{s,act}$ and $F_{s,act}$, diagonal dominance is achieved as can be seen from Figure 5.22(b). This latter RGA shows similar behavior as the RGA of P_ω in Figure 5.21. Hence, the electromechanical actuation system decouples the in- and outputs of the variator by the meshing of the ring gears.
Interaction measures can be used to predict the stability of decentralized control systems. Moreover, they provide a measure for the performance degradation caused by these control structures [32]. Here, the matrix

$$E(s) = (P_\omega(s) - \tilde{P}_\omega(s))\tilde{P}_\omega^{-1}(s) \tag{5.24}$$

gives a measure for the relative errors by approximating the full block system $P_\omega(s)$ by a block diagonal system $\tilde{P}_\omega(s)$. An indication of the bandwidth over which good control can be achieved is then given by the spectral radius $\rho^{-1}(E(jw))$. Using the Rijnsdorp interaction measure [80], defined by $\kappa(s) = P_{\omega_{12}}(s)P_{\omega_{21}}(s)/P_{\omega_{11}}(s)P_{\omega_{22}}(s)$, this bound on the closed loop gain can be calculated [32] according to

$$|\tilde{h}_i(jw)| < \rho^{-1}(E(jw)) = |\kappa(jw)|^{-1/2}, \quad i = 1, 2 \tag{5.25}$$

where $\tilde{h}_1 = P_{\omega_{11}}K_1(1 + P_{\omega_{11}}K_1)^{-1}$, $\tilde{h}_2 = P_{\omega 22}K_3(1 + P_{\omega_{22}}K_3)^{-1}$ and ρ^{-1} denotes the inverse spectral radius. Figure 5.23 shows this measure for the identified plant. Although this is a rather conservative measure, because phase information is discarded, no significant limitations are present. Interesting to note is that when the IMC interaction measure [32] is used to specify bounds on individual loops, the closed loop gain $\tilde{h}_i(jw)$ is less than 0 [dB] on the ratio loop, whereas no limitations are imposed on the slip loop. Obviously, this is too conservative for this system. A less conservative measure for stability for a 2x2 system is [32]

$$N(-1, -\tilde{h}_1(s)\tilde{h}_2(s)\kappa(s)) = 0 \tag{5.26}$$

where $N(k, g(s))$ is the net number of clockwise encirclements of $g(s)$ around point $(k, 0)$. This criterium will be used to evaluate the final control design.

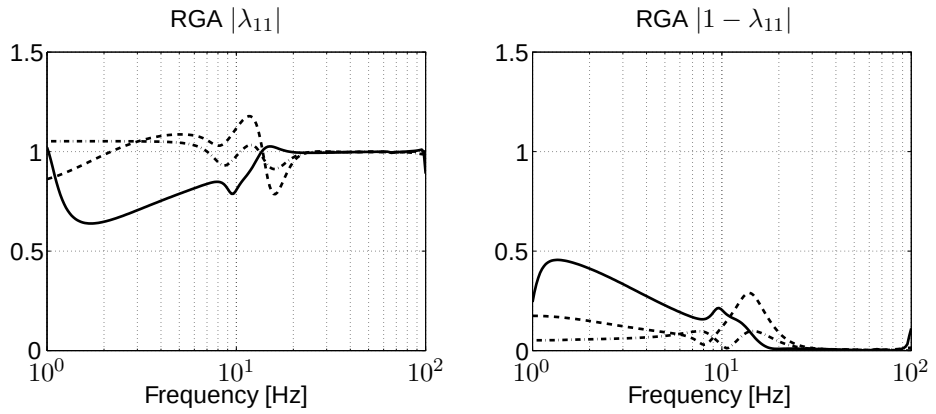

Figure 5.21: RGA of P_ω at $r_g = 0.5$ (-), $r_g = 1$ (-.) and $r_g = 2$ (--) for optimal efficiency slip values

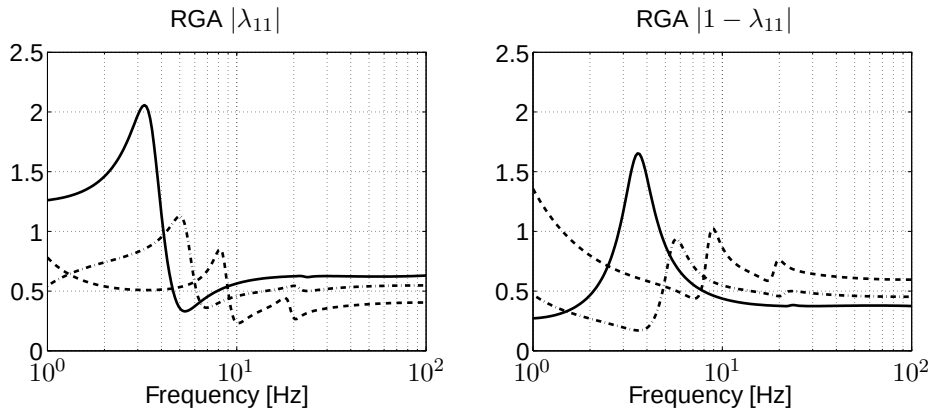

(a) $u = [F_{p,act} \quad F_{s,act}]^T$

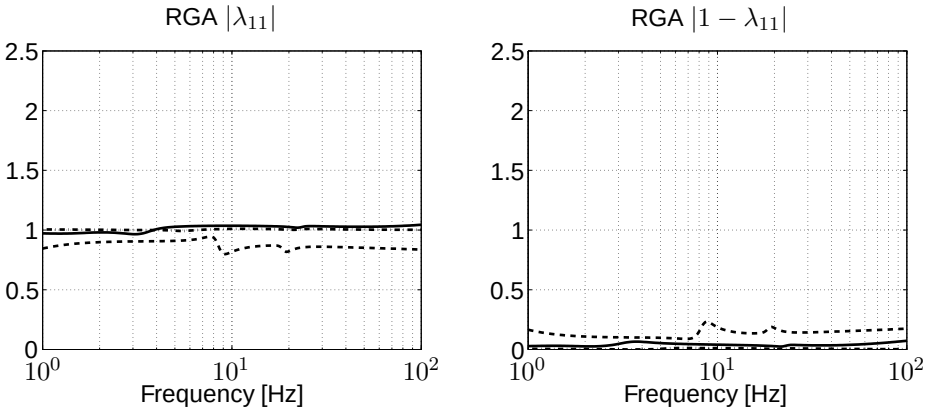

(b) $u = [F_{p,act} + F_{s,act} \quad F_{s,act}]^T$

Figure 5.22: RGA of CVT with direct actuation at variator at $r_g = 0.5$ (-), $r_g = 1$ (-.) and $r_g = 2$ (--) for optimal efficiency slip values

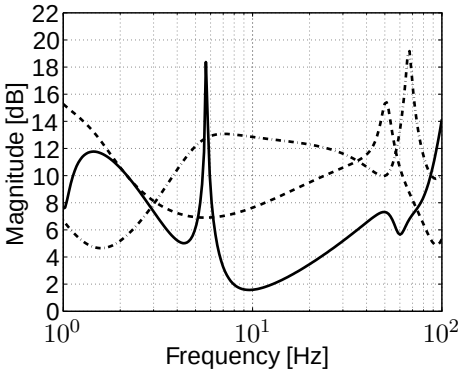

Figure 5.23: Inverse spectral radius of $E(jw)$ at $r_g = 0.5$ (-), $r_g = 1$ (-.) and $r_g = 2$ (- -) for optimal efficiency slip values

Chapter 6

Control design and evaluation

The problem of ratio control is in fact a servo problem, in which the output must be kept close to a given reference, whereas the problem of slip control is a regulator problem, in which a disturbance entering at the system output is to be rejected. Both these goals can be achieved by shaping the sensitivity, such that a minimum bandwidth requirement and integral control are imposed. A requirement for the control problem is that it should be achieved with limited actuation energy. Furthermore, the large measurement noise, mostly present in the automotive environment, imposes limitations on the performance. By bounding the control sensitivity, thereby imposing high frequency roll-off, these latter requirements can be realized.
Three different control designs are presented in Section 6.1 [51]. First a decentralized controller is designed using manual loop shaping. To justify the resulting design, a comparison will be made with a decentralized SISO $\mathcal{H}_\infty$ design. Both control designs follow the Sequential Loop Closing procedure. Finally, a MIMO $\mathcal{H}_\infty$ controller is presented. This type of controller is not directly applicable in the Empact system, because of the requirement to switch the slip controller. This design however gives insight in possible performance improvements.
In order to achieve robust stability and performance, the choice of the nominal plant is important. For the ratio controller this choice is trivial, since the estimation of $P_{\omega_{11}}$ varies only slightly under different operating conditions. For the slip controller this choice is more difficult, since the plant varies significantly with ratio and slip (Figure 5.15). However, the goal is to control slip close to the maximum efficiency of the variator, where the plant P_ω varies only slightly with the ratio (Figure 5.19). Therefore, for both ratio and slip control design, the nominal plant is chosen at $\hat{r}_g = 1.0$ [-] and $\hat{\nu} = 1.0$ [%]. To achieve robust performance in different operating points, gain scheduling of the slip controller is implemented on the final control design. This is the subject of Section 6.2. Section 6.3 presents and evaluates a slip controller switching and anti-windup strategy. Finally, Section 6.4 shows closed loop

performance results on the simulation model and on the prototype test rig.

6.1 Control designs

This section first presents the design considerations and procedures of the different controllers. In these design steps often references are made to the resulting closed loop transfer functions. Figures 6.2 to 6.5 show the controller K, sensitivity S_ω, control sensitivity KS_ω and the open loop KP_ω respectively. Figure 6.6 shows the Nyquist plot of the equivalent plant open loop transfer function for both decentralized controllers. The reference to these figures is left out in the remainder of this section.

6.1.1 Manually loop-shaped decentralized controller

As stated in Section 4.3, for stability issues, first the ratio controller will be designed. The slip controller K_3 is then designed on the equivalent plant $G_{\omega_{22}} = P_{\omega_{22}} - P_{\omega_{21}} K_1 S_{\omega_{11}} P_{\omega_{12}}$. The structure of K_1 is chosen the same as for the ratio controller used during the identification procedure (Figure 5.6), however the gain is adjusted to obtain a bandwidth close to 10 [Hz]. The resulting equivalent plant $G_{\omega_{22}}$ is almost identical to the plant $P_{\omega_{22}}$, and is therefore not depicted here. Based on the characteristics of the plants at the optimal slip level, shown in Figure 5.19, it can be seen that a lead-lag controller would be sufficient to obtain the aimed closed loop bandwidth of 10 [Hz] with adequate gain and phase margins for slip control. A low-pass filter should be added for noise reduction. Even for the plants shown in Figure 5.18, this type of controller in combination with gain scheduling could obtain satisfying performance. Based on $G_{\omega_{22}}$ obtained from the plants shown in Figure 5.19, K_3 is designed as a lead-lag controller with a pole at the origin, a complex zero pair at $f = 6.32$ [Hz] with a relative damping of $\zeta = 0.61$ [-], a pole at $f = 175$ [Hz] and a 2^{nd} order lowpass filter with a relative damping of $\zeta = 1$ at 13 [Hz]. The complex zero pair originates from the zero of the lead filter at $f = 7.53$ [Hz] and the zero of the lag filter at $f = 5.31$ [Hz].
When looking at the Nyquist plots of the open loop $K_1 G_{\omega_{11}}$ and $K_3 G_{\omega_{22}}$, it can be seen that both loops obtain stable behavior with proper gain and phase margins.

6.1.2 $\mathcal{H}_\infty$ loop-shaped decentralized controller

The decentralized $\mathcal{H}_\infty$ controllers are sequentially designed using the 2-block mixed sensitivity problem S/KS, depicted in Figure 6.1. In this way, the sensitivity and control sensitivity can be constrained using frequency shaped weighting filters. The constraints are given by

$$|S_i(s)| \leq 1/\left|W_i^S(s)\right| \tag{6.1}$$

$$|KS_i(s)| \leq 1/\left|W_i^{KS}(s)\right| \tag{6.2}$$

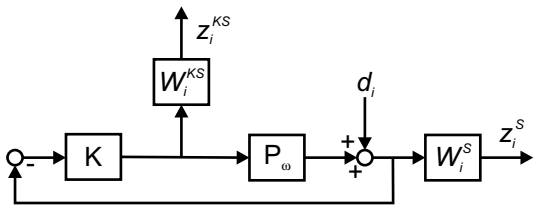

Figure 6.1: Mixed sensitivity (S/KS) problem

where i is 1 or 3 for the ratio and slip loop respectively. The sensitivity weights are chosen such that the amplitude of S is limited to 6 [dB], integral control is enforced and the desired bandwidth is obtained. Based on the plant properties, *i.e.* a -1 slope at low frequencies of $P_{\omega_{11}}$ and a zero slope of $P_{\omega_{22}}$, a second order filter is needed for the ratio loop, whereas for the slip loop a first order filter is sufficient to obtain integral control. The weighting filters for the sensitivity are then given by

$$W_1^S = 0.5\frac{s^2 + 2\beta\omega_{z_1}s + \omega_{z_1}^2}{s^2 + 2\beta\omega_{p_1}s + \omega_{p_1}^2} \tag{6.3}$$

$$W_3^S = 0.5\frac{s + \omega_{z_3}}{s + \omega_{p_3}} \tag{6.4}$$

with $\beta = 0.7$, $\omega_{z_1} = 2\pi f_{bw_1}$, $\omega_{z_3} = 3\pi f_{bw_3}$ and $\omega_{p_i} = 2\pi f_{bw_i}/10^3$, where f_{bw_i} is the desired closed loop bandwidth of the corresponding loop. The choice of a weighting filter for the control sensitivity is not that straightforward. Using the control sensitivity from the manual design, a suitable choice can be made. To achieve second order low pass filtering, the weighting filters are chosen as

$$W_i^{KS} = g_i\left(\frac{\omega_{p_i}}{\omega_{z_i}}\right)^2\frac{s^2 + 2\beta\omega_{z_i}s + \omega_{z_i}^2}{s^2 + 2\beta\omega_{p_i}s + \omega_{p_i}^2} \tag{6.5}$$

where $\beta = 0.7$, $\omega_{z_i} = 6\pi f_{bw_i}$ and $\omega_{p_i} = 2\pi 10^3 f_{bw_i}$. The low frequency gains g_1 and g_3 are given by $g_1 = -25$ [dB] and $g_3 = -10$ [dB]. In this way, the shape of the controller at low frequencies is determined by W_i^S, whereas the high frequency shape is determined by W_i^{KS}. The inverse of these bounds are shown in the resulting sensitivity and process sensitivity bode plots.

The $\mathcal{H}_\infty$ γ-iteration of the ratio controller K_1 achieved $\gamma = 0.99$. Using the resulting controller, the equivalent plant of the second loop is calculated and used as input for the second $\mathcal{H}_\infty$ optimization. This γ-iteration achieved $\gamma = 0.95$.

As described in Chapter 5, the plant order was typically chosen 20. Together with the weighting filters, the resulting order of K_1 would be 24 and that of K_3 would be 23. Using balanced realization [91], the order of the controllers are reduced to 13 and 18 respectively without any significant loss in closed loop performance in the frequency range of interest.

Studying the Bode plot of controller K_3 (Figure 6.2), it can be seen that, instead of using a notch filter to decrease the effect of the resonance at 65 [Hz], the $\mathcal{H}_\infty$

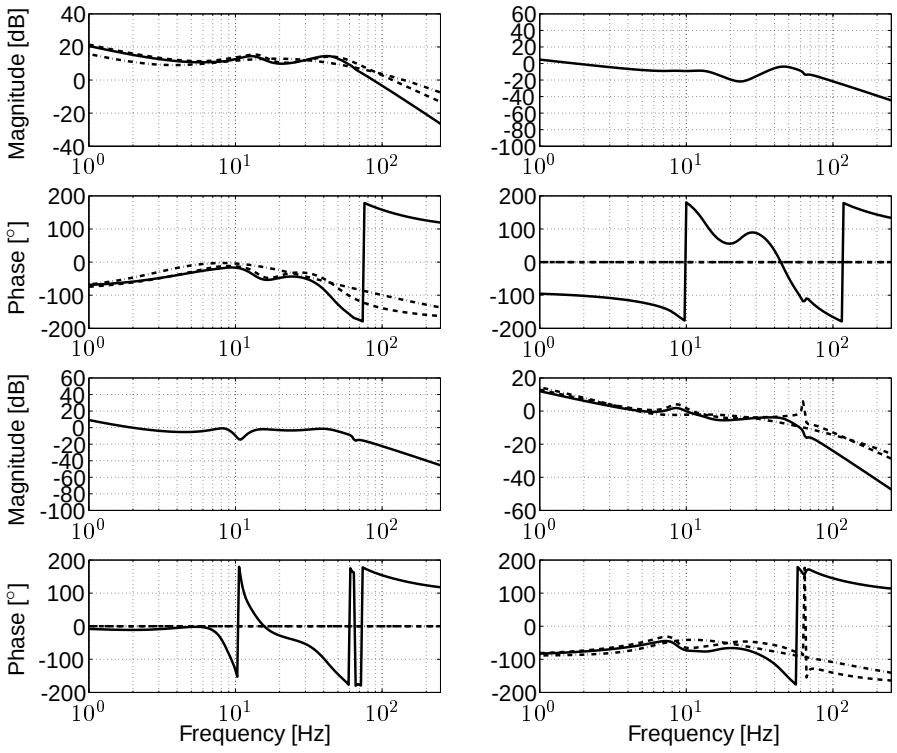

Figure 6.2: Lead-lag controller (-.), decentralized $\mathcal{H}_\infty$ (- -) and MIMO $\mathcal{H}_\infty$ design (-)

controller adds a resonance at 62 [Hz] to obtain additional phase loss, thereby turning the system resonance towards the right half plane in the open loop Nyquist plot ($K_3 G_{\omega_{22}}$ in Figure 6.6(b)) and achieving stable behavior. The result is that a higher gain is achieved around these frequencies, thereby reducing the sensitivity gain. The resulting gain and phase margins are slightly better than with the manually designed controller.

6.1.3 $\mathcal{H}_\infty$ MIMO controller

The weighting filters used here are chosen identical to the weighting filters in the decentralized design. Here, the $\mathcal{H}_\infty$ optimization achieved $\gamma = 1.23$. The bound prescribed by the weighting filters was minimally exceeded by the sensitivity at low frequencies. However, because $\|S\|_\infty < 6$ [dB], no optimization of the weighting filters is done to improve γ. The resulting controller is of order 28.
To reduce the influence of the resonance at 65 [Hz], this controller adds a notch filter at this frequency. Although no additional bounds are put on the control sensitivity, this controller achieves more high frequency roll-off. Also, the MIMO controller implicitly scales the sensitivity such that the cross-terms are of the same order of magnitude and obviously tries to keep the singular values of the sensitivity below the bound W_i^S. In the decentralized designs, the sensitivity of the corresponding equivalent SISO loop are taken into account, however not the singular values of the full

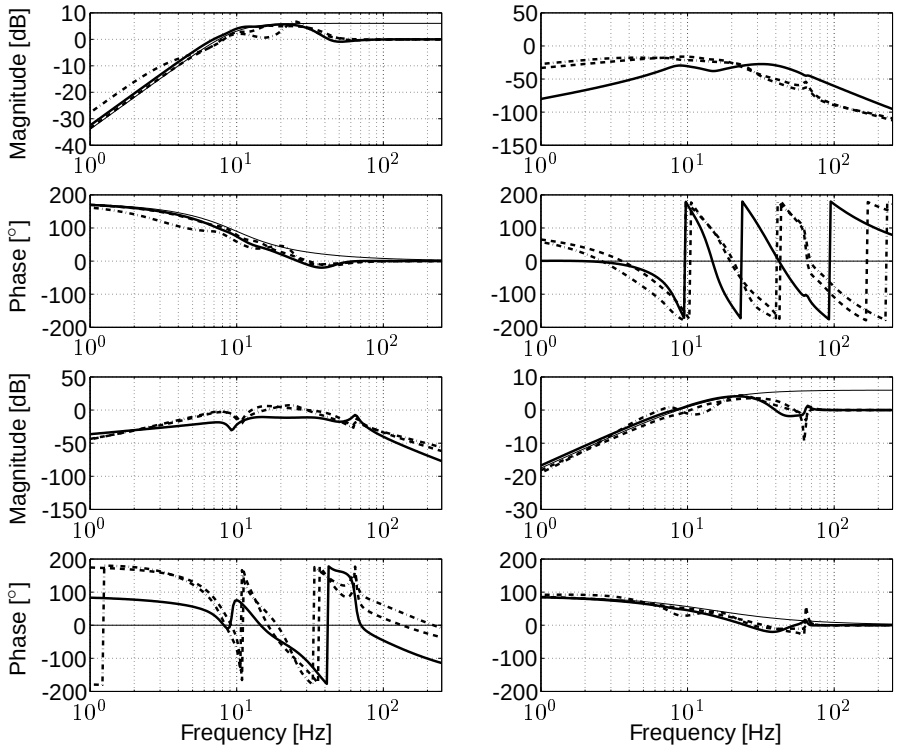

Figure 6.3: S with lead-lag (-.), decentralized $\mathcal{H}_\infty$ (- -), MIMO $\mathcal{H}_\infty$ design (-) and $1/W_i^S$ (thin solid line)

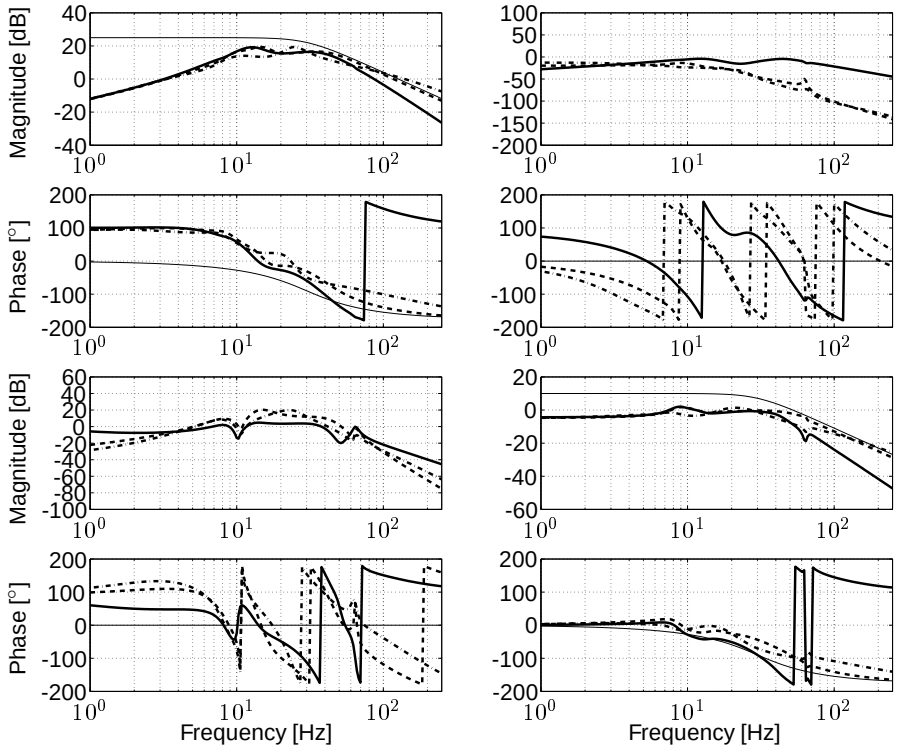

Figure 6.4: KS with lead-lag (-.), decentralized $\mathcal{H}_\infty$ (- -), MIMO $\mathcal{H}_\infty$ design (-) and $1/W_i^{KS}$ (thin solid line)

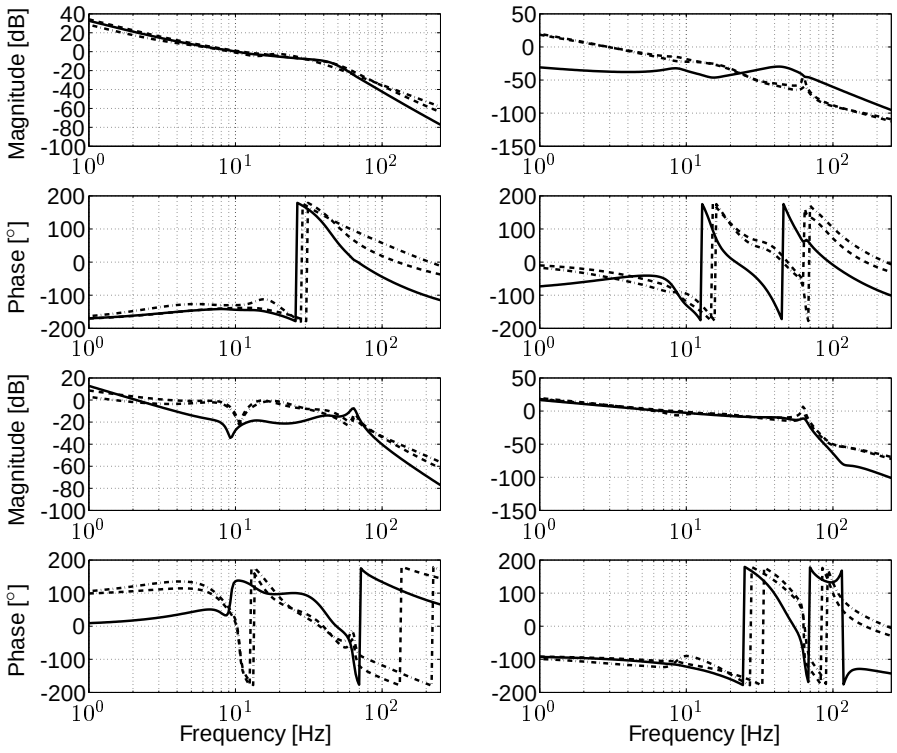

Figure 6.5: KP_ω with lead-lag (-.), decentralized $\mathcal{H}_\infty$ (- -) and MIMO $\mathcal{H}_\infty$ design (-)

closed loop system. Without proper input/output scaling, the cross terms can then have significant influence on the singular values, such that $\|S\|_\infty > \|\text{diag}\left(W_i^S\right)\|_\infty$. Without scaling, the manual design achieves $\|S\|_\infty < 10.5$ [dB] and the decentralized $\mathcal{H}_\infty$ design achieves $\|S\|_\infty < 9.3$ [dB]. Additional input/output scaling can be applied to optimize these results.

6.2 Gain scheduling

To obtain robust performance for all plants, gain scheduling is implemented for controller K_3. The scheduling parameter is chosen as a function of the ratio and slip reference *i.e.* $g_{K_3} = f\left(\nu_{ref}, r_{g_{ref}}\right)$. The gain is chosen such that each scheduled closed loop system a bandwidth of approximately 10 [Hz] is obtained. The scheduling parameter g_{K_3} is shown in Figure 6.7(a) as a function of the slip for LOW, MED and OD ratio.

In the case of scheduling based on the reference trajectory, robust stability and robust performance are maintained, given that the feedback system is stable for all closed loop combinations, and the reference trajectory varies slowly and does not excite unmodelled dynamics of the system [89]. Stability of the resulting closed loop system can be validated using the equivalent plant open loop transfer function and the stability requirement presented in (5.26). This requirement is however not critical

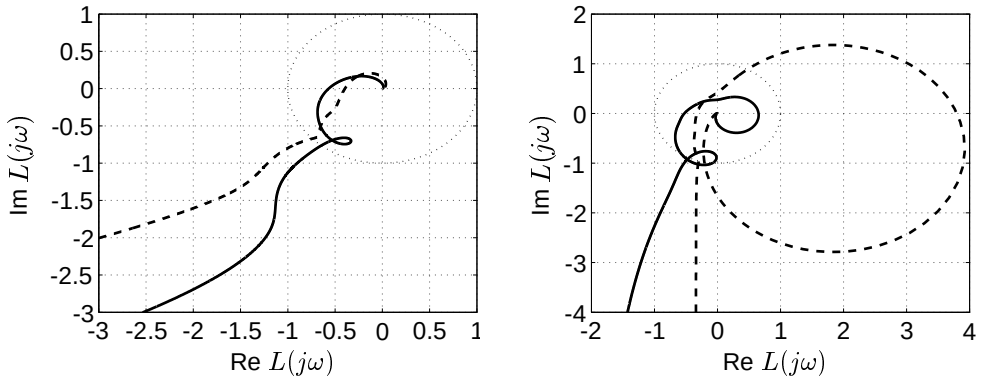

(a) $K_1 G_{\omega_{11}}$ (b) $K_3 G_{\omega_{22}}$

Figure 6.6: Nyquist plot of equivalent plant for manual (–) and $\mathcal{H}_\infty$ (- -) decentralized controllers

for this system, because the two-way interaction of the system is minimal, hence the multiplication of $\tilde{h}_1 \tilde{h}_2 \kappa$ results in relatively small amplitudes. Therefore, stability is analyzed using the open loop transfer function $G_{\omega_{22}} K_3 / g_{K_3}$, *i.e.* the equivalent plant when the gain scheduling is applied. Figure 6.7(b) shows the resulting open loop Nyquist plot. It can be seen that the stability requirements are met for all plants. It is furthermore assumed that the reference trajectory varies relatively slowly and does not excite unmodelled dynamics, such that stability is not influenced by the gain adaptation.
A more thorough analysis of performance and stability using gain scheduling, for example by using Lyapunov conditions and slow-variation arguments [93], [76], [77], [61], or even more extensively in a LPV-framework [60], [61], [78], is beyond the scope of this thesis.

6.3 Controller switching strategy

As stated in Section 4.2, to control slip at low driveline torques requires low clamping forces which could lead to control problems due to the high friction in the system. Switching off the slip controller is then required. In this section four switching strategies are discussed and illustrated using simulation results of a ratio change from OD to LOW at $\dot{x}_{p_{ref}} = -4$ [mm/s] from $t = 40$ [sec] to $t = 44$ [sec]. In this simulation, the slip reference is chosen as $\nu_{ref} = 0.8$ [%] for $r_g = 2$ [-], $\nu_{ref} = 0.8$ [%] for $r_g = 1$ [-], $\nu_{ref} = 1.8$ [%] for $r_g = 0.5$ [-] and a linear interpolation for other ratios. The primary speed is controlled at $\omega_p = 200$ [rad/s] using a stabilizing PI-controller, obtaining a closed loop bandwidth of approximately 1 [Hz]. A constant secondary load of $T_{S_2} = -50$ [Nm] is exerted by the load motor at the system. During this ratio change, the torque at the variator shaft T_s decreases to very low values and

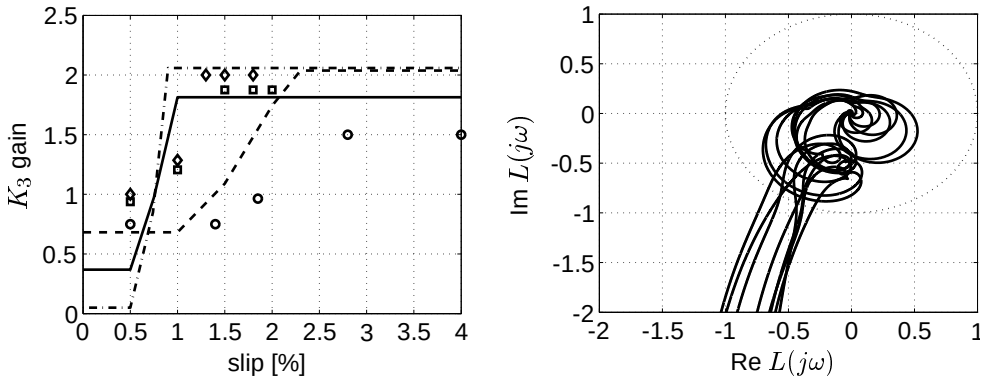

(a) g_{K_3} (b) $G_{\omega_{22}} K_3 / g_{K_3}$

Figure 6.7: Gain scheduling of K_3 for simulation (lines) and measurements (signs) in LOW (- -, o), MED (-, □) and OD (-., ⋄)

crosses zero. Figure 6.8 shows results of slip and clamping force during this fast ratio change for four different control strategies. Note that, because the slip controller K_3 uses the absolute slip value for feedback, the absolute value $|\hat{\nu}|$ is shown. The ratio tracking performance is minimally influenced for all four switching strategies and is therefore not discussed here.

In the first strategy (Figures 6.8(a) and 6.8(b)), the slip controller is not switched. Although the slip is stabilized, the tracking shows large errors. At the point where the clamping forces F_p and F_s become 0 [N], the slip increases at a relatively fast rate and the integrator of the slip controller winds up. The resulting behavior is very nervous. To minimize this effect, an anti-windup strategy based on the clamping force is required. The actual clamping forces can however not be measured, whereas estimation of the clamping forces is very difficult due to the practically unpredictable friction forces in the system. An anti-windup based on the clamping forces is therefore not applicable in a practical environment.

Another possibility to minimize the windup of the integrator, is to switch off the slip controller for low load torques. Figures 6.8(c) and 6.8(d) show results when K_3 is switched off for $T_p < 20$ [Nm]. It can be seen that, although the clamping forces saturate at 0 [N], no large slip peaks occur. The nervous behavior is however still present when K_3 is switched back on at time $t = 41.6$ [sec].

Figures 6.8(e) and 6.8(f) show results when K_3 is switched off for $T_p < 30$ [Nm]. Here also the slip shows no large peaks and, more interesting, the nervous behavior is less pronounced. The clamping forces however, increase to relatively large values compared to the previous strategies, which is not desired when trying to minimize the actuation power.

A fourth strategy is shown in Figures 6.8(g) and 6.8(h). Here not the complete controller is switched, but only the integrator state of K_3 during the ratio change.

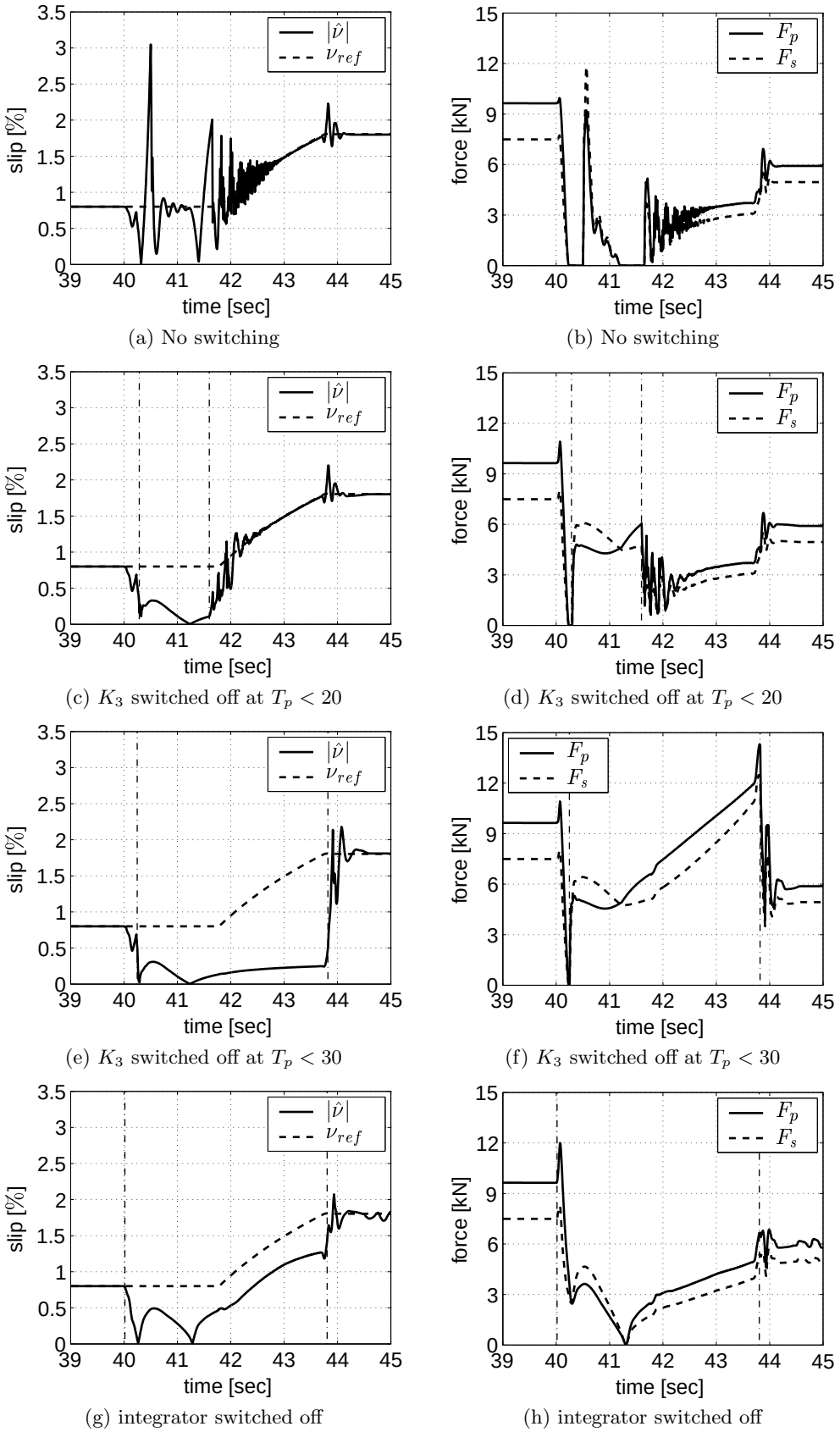

(a) No switching (b) No switching

(c) K_3 switched off at $T_p < 20$ (d) K_3 switched off at $T_p < 20$

(e) K_3 switched off at $T_p < 30$ (f) K_3 switched off at $T_p < 30$

(g) integrator switched off (h) integrator switched off

Figure 6.8: Slip tracking performance at $\dot{x}_{p,ref} = -4$ [mm/s] with four control strategies (controller K_3 switching takes place at vertical dash-dotted lines)

It can be seen that both the large slip peaks are reduced and the nervous behavior is less. During the ratio change the controller still tracks the slip reference, nevertheless with a small offset. The clamping forces are kept close to the optimal values. Moreover, a certain robustness against unexpected torque disturbances is maintained. When switching the integrator part of K_3, the high frequency behavior of the controller is maintained. At low frequencies, the gain of the controller reduces (slope 0) and the phase is close to 0°. When studying the open loop Nyquist plot from Figures 6.6 and 6.7(b), it can be shown that the resulting system is stable when the integrator is switched, as the gain does not increase and the phase increases +90° at low frequencies.
Based on the results from these simulations and analysis, it can be concluded that the switching of the integrator state is the most promising strategy regarding performance and stability. However, additional experiments on the measurement setup have to be performed to verify and optimize this strategy for performance and stability robustness.

6.4 Closed loop performance evaluation

This section presents closed loop controller performance evaluation results from the closed loop system with the designed controllers, including gain scheduling and switching strategy. First the evaluation results using the simulation model are shown. Next, the performance evaluation is extended to the experimental setup. Experimental evaluation of the Empact CVT with respect to power losses and efficiency is presented in Chapter 7.

6.4.1 Simulation evaluation

To evaluate the controller performance and stability of the closed loop system with slip controller gain scheduling and switching, numerous simulations are performed. Some typical results will be described in this section.
To study the disturbance rejection of the slip controller, Figures 6.9(a) to 6.9(f) show results from a simulation when a torque disturbance of -50 [Nm] is applied at the secondary load motor for 0.1 [sec] and 2 [sec] at ratios $r_g = 0.5$ [-], $r_g = 1.0$ [-] and $r_g = 2.0$ [-]. It can be seen that the slip peaks to 2.5 [%], but settles again at its reference within 0.5 [sec] for the pulse and within 0.2 [sec] for the step disturbance. A higher torque peak of -100 [Nm], as shown in Figures 6.9(g) and 6.9(h) for $r_g = 0.5$ [-], results in a relative high slip peak of up to 8 [%], but the slip is reduced below a value of 3 [%] within 0.1 [sec]. This slip peak will not result in damage of the variator (Chapter 4 and [103]). For $r_g = 1.0$ [-] and $r_g = 2.0$ [-] this higher torque peak resulted in a maximum slip level below 5 [%] (not shown here).
To evaluate tracking performance for both ratio and slip, Figures 6.10(a) to 6.10(h) show simulation results of an up- and downshift from $r_g = 0.5$ [-] to $r_g = 2.0$ [-] and

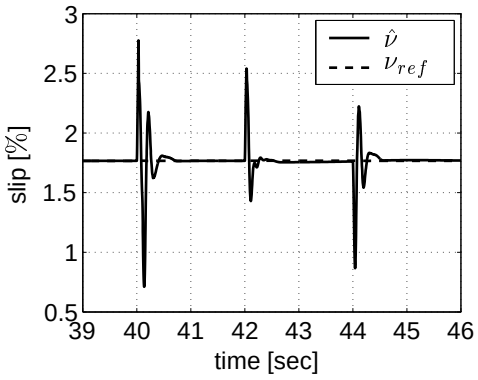

(a) Slip at $\hat{r}_g = 0.5$

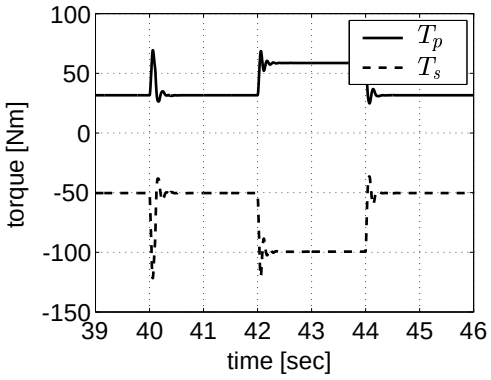

(b) Torque at $\hat{r}_g = 0.5$

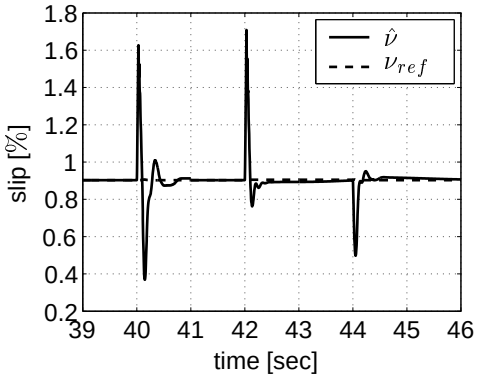

(c) Slip at $\hat{r}_g = 1.0$

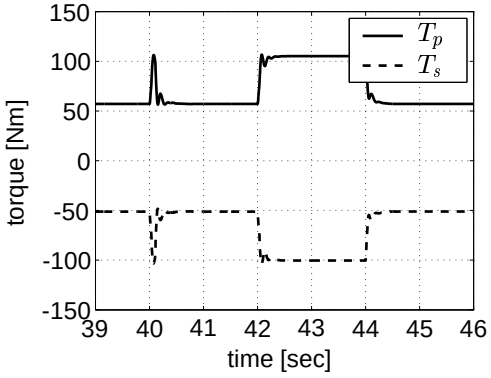

(d) Torque at $\hat{r}_g = 1.0$

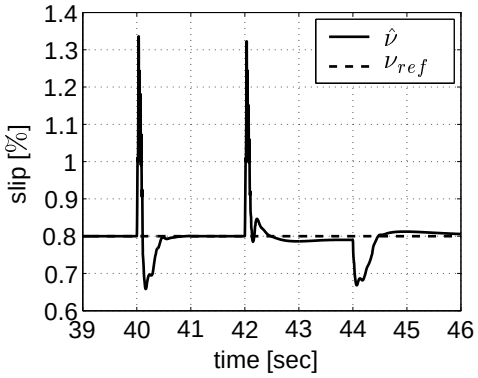

(e) Slip at $\hat{r}_g = 2.0$

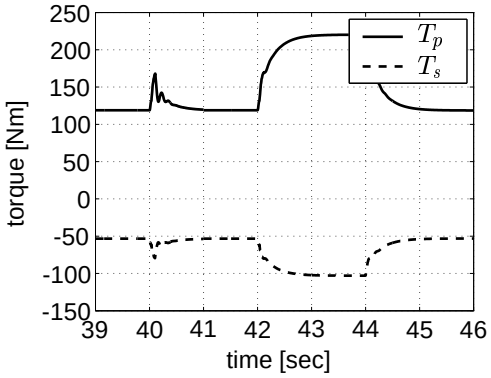

(f) Torque at $\hat{r}_g = 2.0$

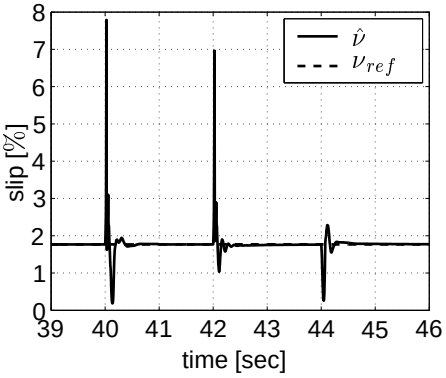

(g) Slip at $\hat{r}_g = 0.5$

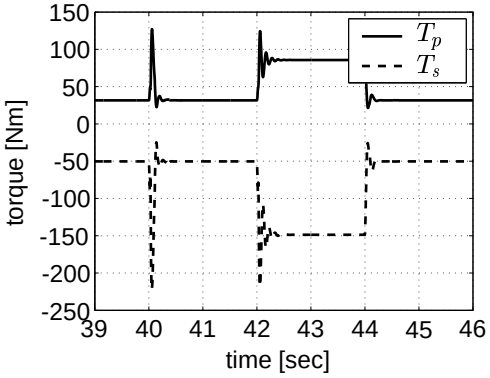

(h) Torque at $\hat{r}_g = 0.5$

Figure 6.9: Controller evaluation results - disturbance rejection

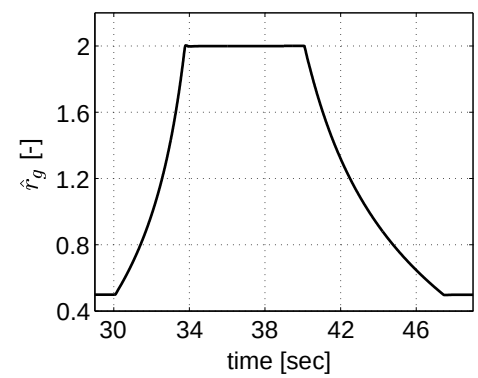

(a) CVT ratio

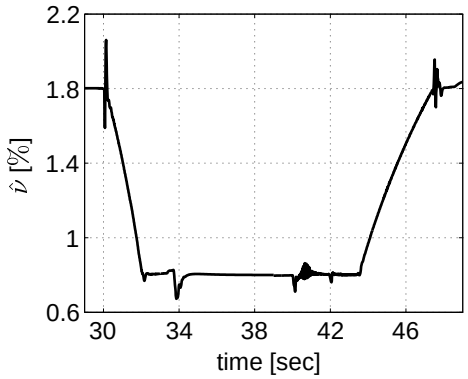

(b) Slip

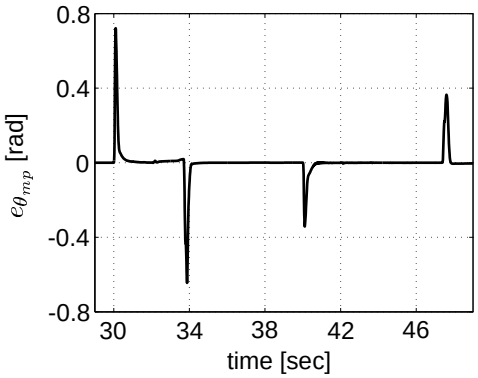

(c) θ_{mp} tracking error

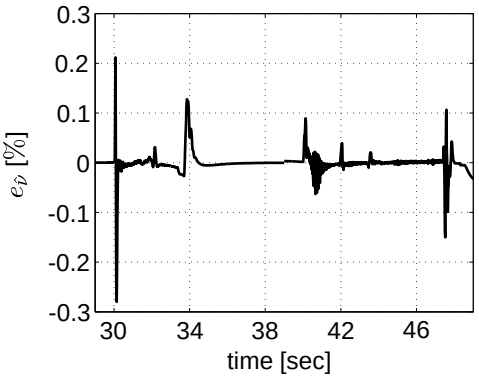

(d) $\hat{\nu}$ tracking error

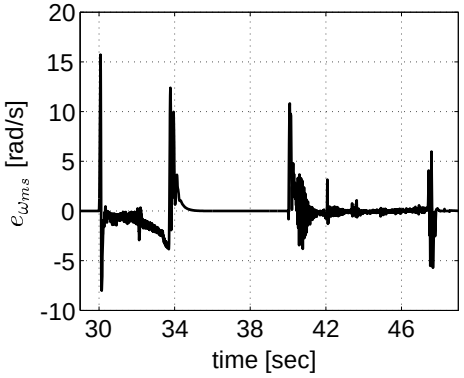

(e) ω_{ms} tracking error

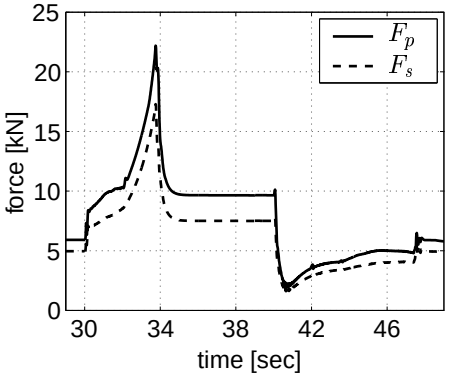

(f) Clamping forces

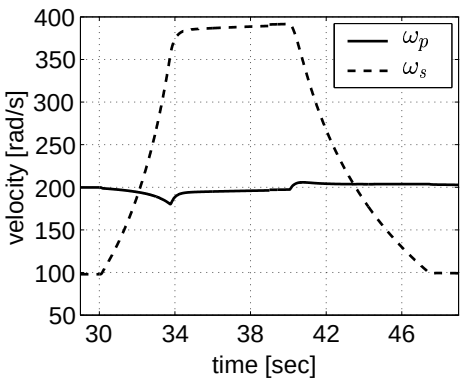

(g) Input and output velocity

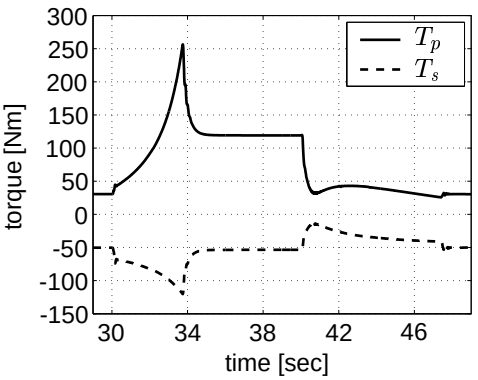

(h) Input torque and output torque

Figure 6.10: Controller evaluation results - tracking performance

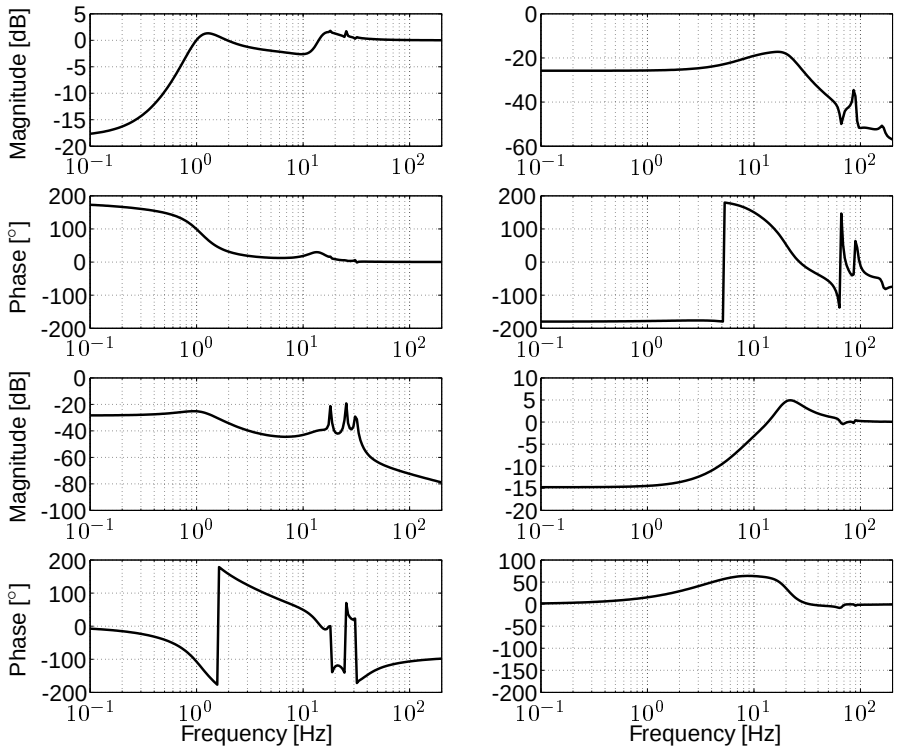

Figure 6.11: Measured sensitivity at $r_g = 1.0$ [-], $\nu = 1.0$ [%], $\omega_p = 200$ [rad/s] and $T_p = 100$ [Nm]

back at $\dot{x}_{p_{ref}} = 4$ [mm/s] and $\dot{x}_{p_{ref}} = -2$ [mm/s] respectively. A constant secondary load of $T_{S_2} = -50$ [Nm] is applied at the load motor. The slip reference is chosen as $\nu_{ref} = 1.8$ [%] for $r_g = 0.5$ [-], $\nu_{ref} = 0.8$ [%] for $r_g = 1$ [-], $\nu_{ref} = 0.8$ [%] for $r_g = 2$ [-] and a linear interpolation for other ratios. The primary speed is controlled at $\omega_p = 200$ [rad/s] using a stabilizing PI-controller, obtaining a closed loop bandwidth of approximately 1 [Hz].

During these ratio shifts, the tracking error $e_{\theta_{mp}}$ remains below 1 [rad] (Figure 6.10(c)), which corresponds to 0.05 [mm] in pulley position error. A pulley position tracking error of 0.5 [mm], which would result in a tracking error of the ICE speed of less than 5 [%], is commonly accepted for CVTs during relatively fast shifting events. The tracking performance of the slip is very good during both the up- and downshift as can be seen in Figure 6.10(d). At the start and stop of the ratio change, *i.e.* where $|\ddot{x}_{p,ref}| > 0$, some small, short peaks can be seen in $e_{\hat{\nu}}$. The tracking error $e_{\omega_{ms}}$ also shows the largest errors at the start and stop of shifting. This error is however not of primary concern.

6.4.2 Experimental evaluation

To verify the closed loop system with the controllers K_1, K_2 and K_3 implemented, the sensitivity is estimated using the pulse response identification as described in

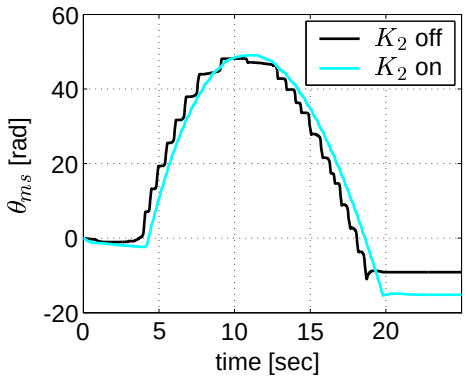

Figure 6.12: Shifting performance with K_2 off (black) and on (gray)

Chapter 5. Figure 6.11 shows the estimated sensitivity for $\hat{r}_g = 1.0$ [-], $\hat{\nu} = 1.0$ [%], $\omega_p = 200$ [rad/s] and $T_p = 100$ [Nm]. The (2,2)-element shows a bandwidth around 10 [Hz] as expected, however due to high friction in the system, the estimation at low frequency is rather poor. This is even more pronounced in the (1,1)-element, where the low frequency estimation is dominated by non-linear friction effects.
Using the estimation of the closed loop sensitivity in different operating points, the gain scheduling parameters for K_3 are determined such that the closed loop bandwidth of the equivalent slip loop is close to 10 [Hz] while maintaining sufficient stability margins. The results are depicted in Figure 6.7(a). The optimal gains deviate slightly from the gains found in the simulation model.
As described in Chapter 4, the shifting performance increases significantly when the velocity of the secondary servo ω_{ms} is controlled. To show this performance enhancement, Figure 6.12 shows θ_{ms} for a ratio change from LOW to OD with and without controller K_2. It can be seen that when this controller is used, the shifting performance is much smoother. This results also in lower tracking errors for both ratio and slip control.
The disturbance rejection of the slip controller is again verified using torque disturbances applied at the CVT output, similar to the simulations shown in Figure 6.9. As will be further discussed in Chapter 7, the used slip reference depends not only on the ratio reference, but also on the applied engine torque. Figures 6.13(a) to 6.13(f) show the results for a 2 [sec] step disturbance for low, medium and overdrive ratio. The left figures show the slip reference ν_{ref} and estimated slip $\hat{\nu}$ in the system, whereas the right figures show the torques at the primary and secondary shafts. The amplitudes of the step disturbances are chosen relatively high, comparable to torque disturbances when driving through a 50 [mm] deep pothole [73]. For the experiment in LOW, the initial torque is below the switching strategy threshold and the integrator state of K_3 is switched off. It can be seen that the slip peaks up to 3-5 [%], depending on the ratio, but settles again at its reference within 0.2 [sec]. Figures 6.14(a) to 6.14(b) show the response of the slip and secondary shaft

torque to a pulse disturbance of 50 [Nm] for 0.1 [sec] exerted by the load motor at the system. It can be seen that the slip controller reduces the slip peaks due to these disturbance also within 0.2 [sec]. Torque disturbances up to 150 [Nm] for both pulse and step excitation have been tested, which caused slip peaks up to 8-10 [%]. These slip peaks were reduced to values below 3 [%] within 0.3 [sec] for all experiments. Visual inspection showed that these short slip peaks do not cause any damage to the belt or pulleys, however more research on this subject is required to investigate the long term effects.

Figure 6.15 shows results of a ratio change experiment from LOW to OD and back for constant pulley reference speed $\dot{x}_{p,ref} = 2$ [mm/s] and $\dot{x}_{p,ref} = -2$ [mm/s] respectively, whereas Figure 6.16 shows results of a ratio change experiment for constant pulley reference speed $\dot{x}_{p,ref} = -4$ [mm/s], $\dot{x}_{p,ref} = +4$ [mm/s] and $\dot{x}_{p,ref} = -6$ [mm/s] respectively. This latter ratio change represents an emergency stop from 65 [km/h] to 15 [km/h] within 2.5 [sec] at an engine speed between 1430 and 1700 [rpm]. During this brake, a vehicle deceleration of -8 [m/s^2] is reached.

The slip reference is chosen ratio and input torque dependent, as described in the previous section and further outlined in Chapter 7. The primary speed is controlled at $\omega_{p,ref} = 150$ [rad/s] and a constant secondary load of $T_{S_2} = -20$ [Nm] is exerted by the load motor at the system. During all ratio changes, the ratio tracking error $e_{\theta_{mp}}$ remains below 2 [rad], even for the relatively fast ratio changes of -6 [mm/s]. When the input torque of the variator exceeds $T_p = 20$ [Nm], it can be seen that the slip controller integrator state is switched on and the slip tracks the slip reference. Even during ratio changes, the slip tracking shows good performance. During the emergency brake at a shift rate of -6 [mm/s], the input torque initially decreases and crosses zero and the slip controller integrator state is shortly switched off and back on. This causes an initial slip peak of -5 [%], whereafter the slip follows the reference again. Note that the controller uses the absolute slip $|\hat{\nu}|$ for feedback, while the actual slip $\hat{\nu}$ is shown here.

Figures 6.15(e) and 6.16(e) show the mechanical output power of the primary and secondary servo, $P_{mp,mech}$ and $P_{ms,mech}$ respectively, whereas Figures 6.15(f) and 6.16(f) show the total power consumed in the primary and secondary servo, P_{mp} and P_{ms} respectively (Chapter 2). It can be seen that during stationary conditions, the total power consumption is very low, typically less than 20 [W]. During the ratio changes of 2 and 4 [mm/s], the total consumed power is limited to 500 [W]. Due to an increase in torque of the primary servo when shifting from LOW to OD, the consumed power shows a short peak up to 750 [W]. Although the mechanical output power of the primary servo is limited to 500 [W] during the emergency brake, the total consumed power in this servo is close to 1300 [W]. This is significantly higher than the results presented in Chapter 2, because the slip in the variator is much lower here (1 [%] instead of 4 [%]). Allowing higher slip values during shifting could substantially decrease the maximum required power.

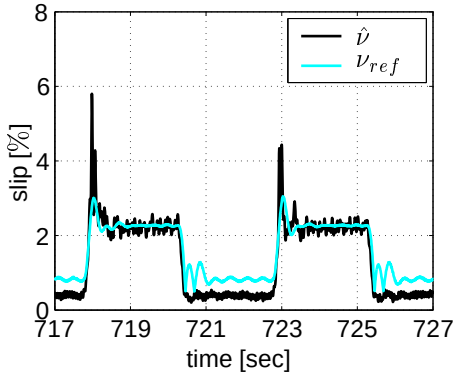

(a) Slip at $\hat{r}_g = 0.5$

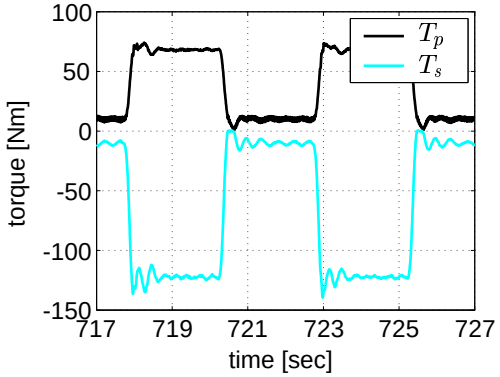

(b) Torque at $\hat{r}_g = 0.5$

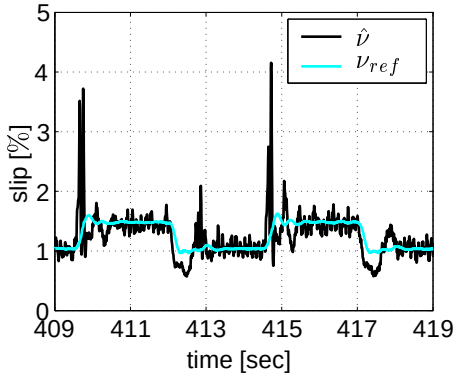

(c) Slip at $\hat{r}_g = 1.0$

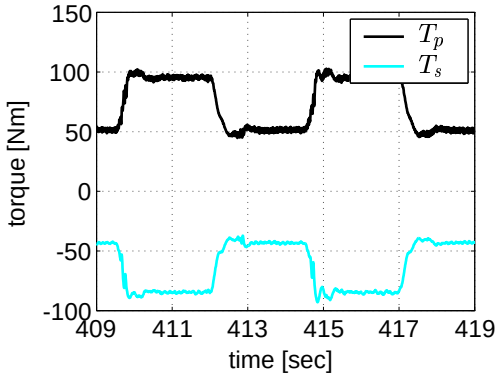

(d) Torque at $\hat{r}_g = 1.0$

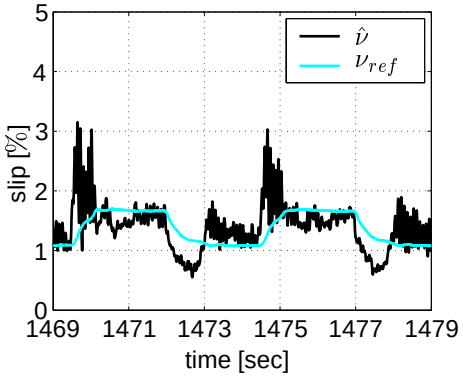

(e) Slip at $\hat{r}_g = 2.0$

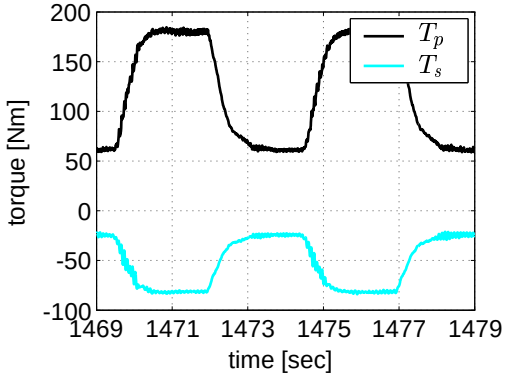

(f) Torque at $\hat{r}_g = 2.0$

Figure 6.13: Step disturbance rejection at the test rig

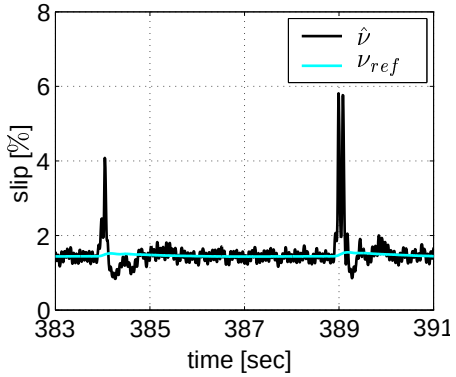

(a) Slip at $\hat{r}_g = 0.5$

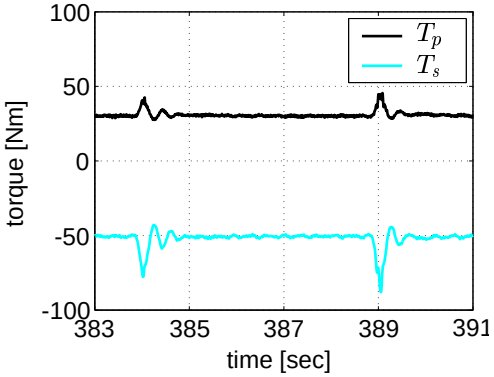

(b) Torque at $\hat{r}_g = 0.5$

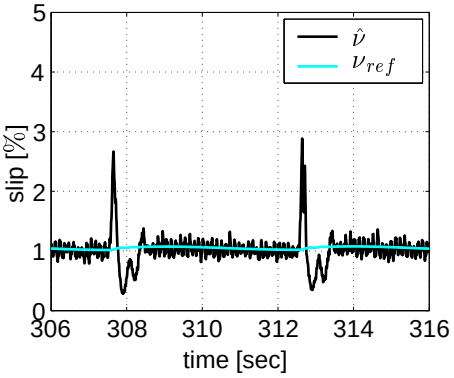

(c) Slip at $\hat{r}_g = 1.0$

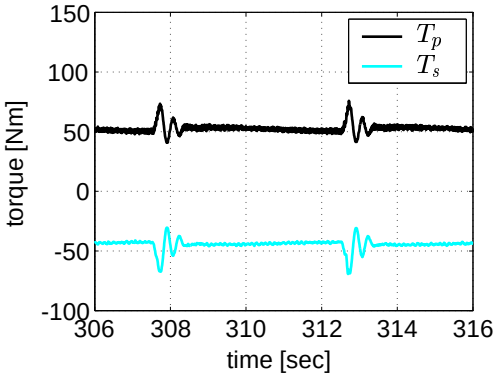

(d) Torque at $\hat{r}_g = 1.0$

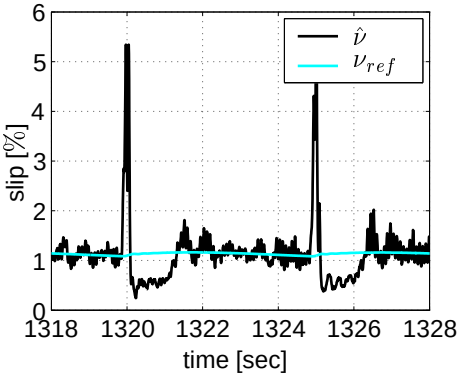

(e) Slip at $\hat{r}_g = 2.0$

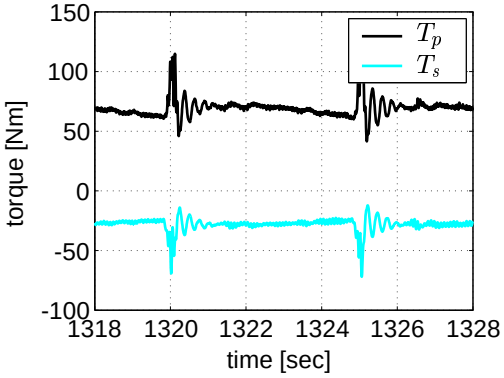

(f) Torque at $\hat{r}_g = 2.0$

Figure 6.14: Pulse disturbance rejection at the test rig

The total efficiency of the Empact CVT is shown in Figures 6.15(g) and 6.16(g). Even for the relatively small load torque (≈ 50 [Nm]), the efficiency during stationary operation in OD is close to 85 [%]. The results presented in Chapter 2, show an optimal efficiency close to 90 [%] for the Empact CVT at 50 [Nm] input torque. Again, to achieve the optimal efficiency, the slip must be controlled at a higher value.

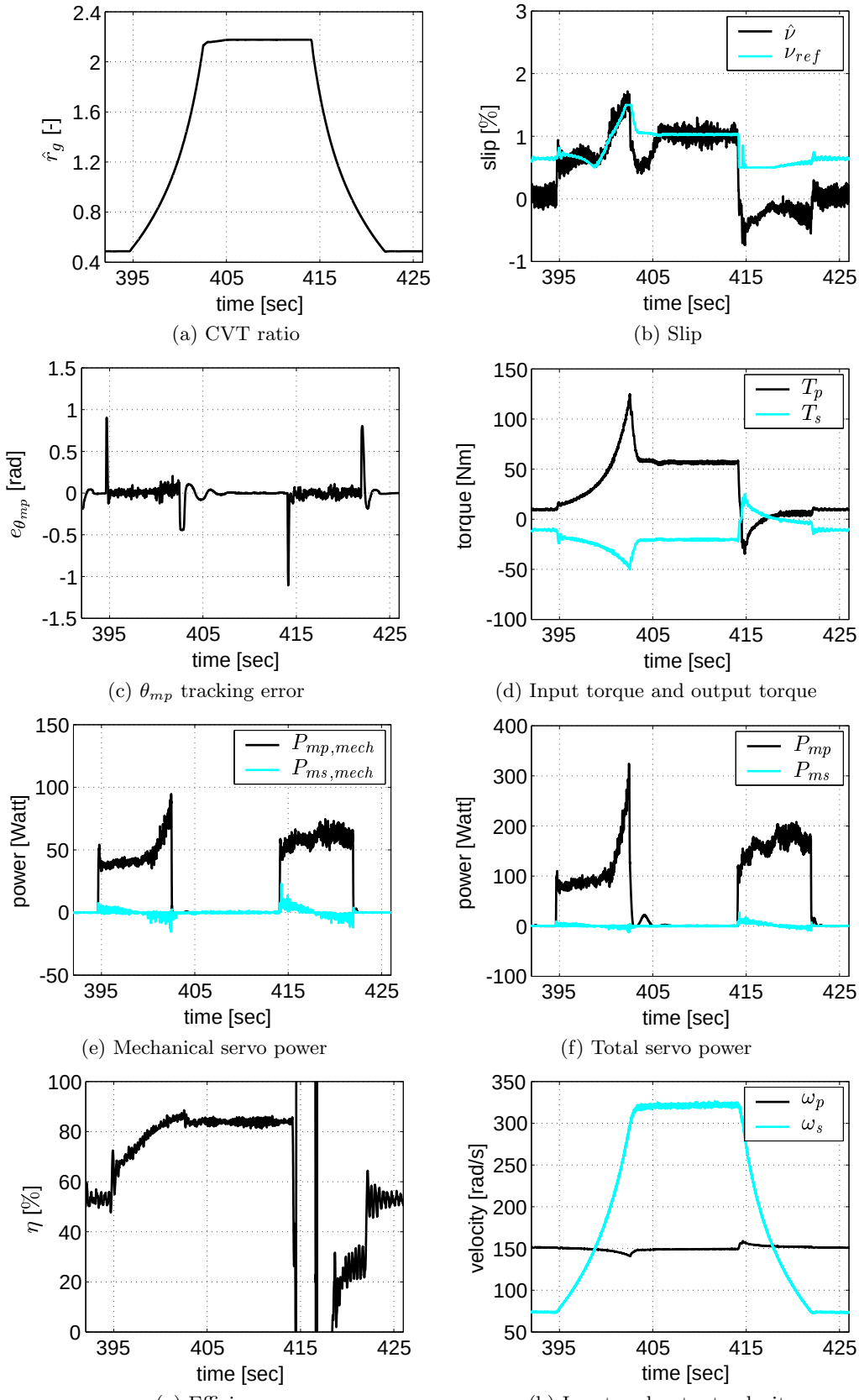

(a) CVT ratio

(b) Slip

(c) θ_{mp} tracking error

(d) Input torque and output torque

(e) Mechanical servo power

(f) Total servo power

(g) Efficiency

(h) Input and output velocity

Figure 6.15: Test rig controller evaluation results - tracking performance

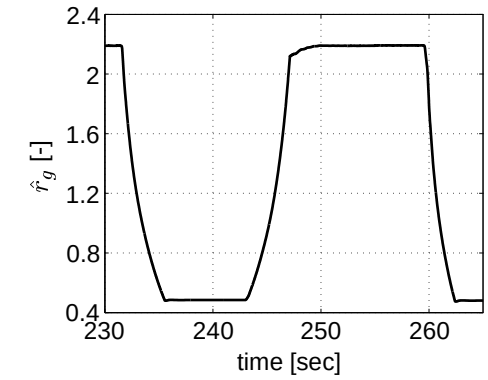

(a) CVT ratio

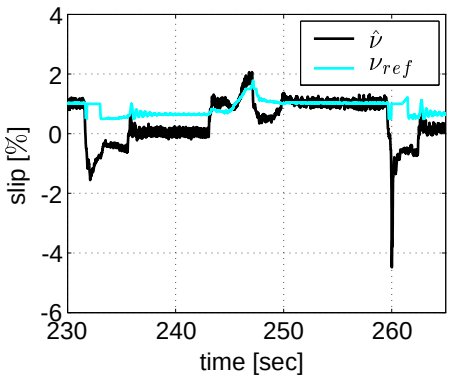

(b) Slip

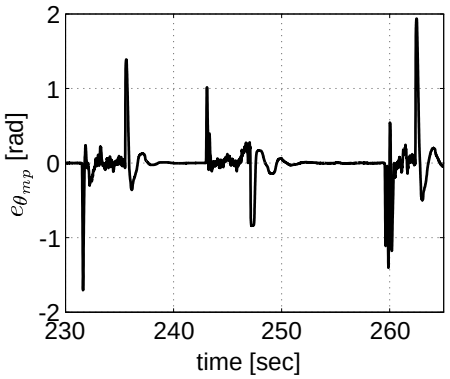

(c) θ_{mp} tracking error

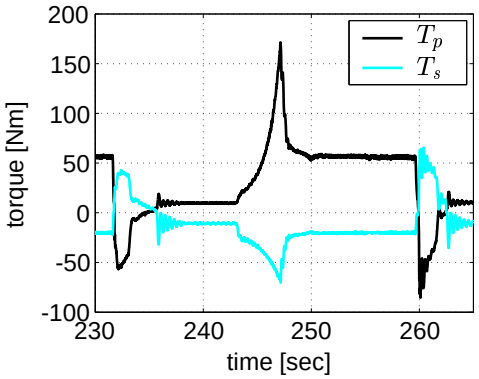

(d) Input torque and output torque

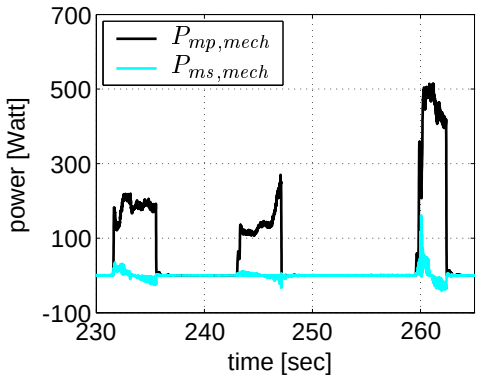

(e) Mechanical servo power

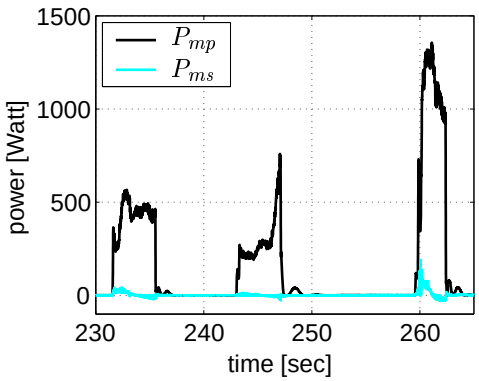

(f) Total servo power

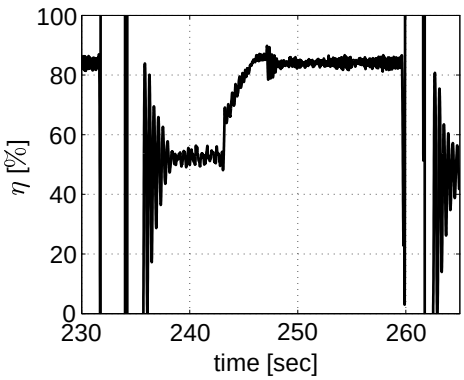

(g) Efficiency

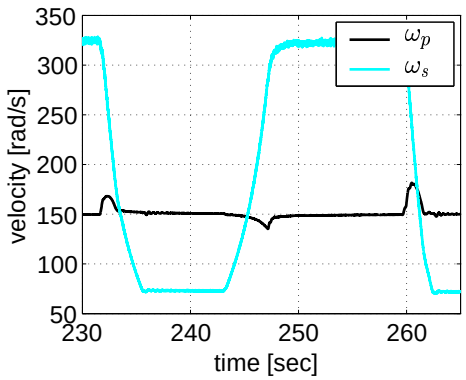

(h) Input and output velocity

Figure 6.16: Test rig controller evaluation results - tracking performance

Chapter 7

Experimental performance evaluation

The robust performance and stability of the controlled system are shown in the previous chapter for both the simulation model and the Empact prototype. The results were obtained at the test rig using experiments, specifically aimed at certain conditioned shifting manoeuvres and torque disturbances. These experiments however do not reflect ordinary driving, such as city or high-way traffic. This chapter presents experimental results for the Empact prototype P2 for ordinary driving situations, represented by the FTP72 driving cycle for the Empact at the test rig and an arbitrary start-stop cycle including kickdown for the Empact in the Audi. The emphasis in this chapter will be on power losses and realized transmission efficiency.

As discussed in Chapter 1, the coordinated driveline controller translates the driver input into a desired ratio reference and throttle position. To obtain realistic shifting behavior during the experiments, Section 7.1 first presents the design of this reference strategy, which is represented by the variogram. The torque converter strategy, *i.e.* the opening and closing of the clutch, is also determined by the coordinated controller. The design of this strategy is beyond the scope of this thesis. Basically, the TC clutch is opened for engine speeds below 1300 [rpm]. Although it is not necessary to decouple the electric driving motor from the CVT at the test rig, the same TC strategy will be used in these experiments to represent realistic variator loads. The slip reference strategy, determined by the CVT component controller, is presented in Section 7.2.

In all experiments in this chapter, the controllers K_1, K_2, K_3 and gain scheduling as described in Chapter 6 are implemented. The K_3 integrator switching (Section 6.3) is applied during relatively fast downshifts and low input torques, *i.e.* if $\dot{x}_p < -2$ [mm/s] or $|T_{ICE}| < 20$ [Nm]. Furthermore, the slip controller K_3 is switched off at low speeds, *i.e.* at $\omega_s < 10$ [rad/s] (≈ 2 [km/h]).

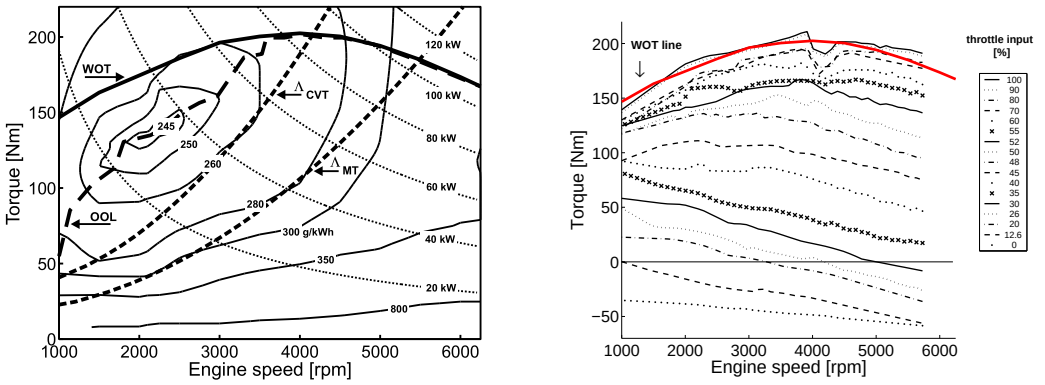

(a) Fuel consumption map

(b) Throttle-torque map

Figure 7.1: Engine characteristics of an Audi A3 2.0 FSI engine

The results of the Empact at the FTP72 driving cycle are presented in Section 7.3. Section 7.4 shows the experimental results of the Audi A3 2.0 FSI at a chassis dyno.

7.1 Ratio reference

In Section 1.3 three operating strategies were introduced. For the *single track* and the *off the beaten track* operating strategies modifications to the ECU are necessary, which are not possible with the test vehicle. Therefore the *speed envelope* strategy, tuned for fuel economy, is chosen for the variogram design. Here, the engine speed is related to the throttle input, such that the engine operating point is close to the Optimal Operating Line (OOL). The variogram design is based on the engine fuel consumption map (Figure 7.1(a)) and the throttle-torque map (Figure 7.1(b)) of the engine. The throttle-torque map is estimated from measurements with the test vehicle on a chassis dyno [73]. Figure 7.2 shows the resulting variogram. Because the OOL represents relatively low engine speeds and high engine torques, the ratio reference tends towards OD relatively fast. For throttle inputs larger than 50 [%], the ratio reference is chosen closer to LOW. To optimize driveability, the desired engine speed is increased for increasing vehicle speed [13]. Furthermore, it can be seen that the engine speed for a throttle input of 0 [%] is higher than for 7.5 [%]. This is implemented to increase engine braking when the driver releases the accelerator pedal. This engine braking effect is also present in MT based drivelines. The maximal engine speed for this E-line variogram is set at 5000 [rpm].
The desired $r_{g_{ref}}$ is translated to a desired trajectory for the primary pulley speed $\dot{x}_{p_{ref}}$ using the geometrical properties of the variator. A driveability study [73] showed that a primary pulley velocity larger than 4 [mm/s] increases shuffling and jerk and is therefore not desired during normal driving. During a kickdown, the additional jerk is recognized as a sportive feeling. Therefore, the desired primary

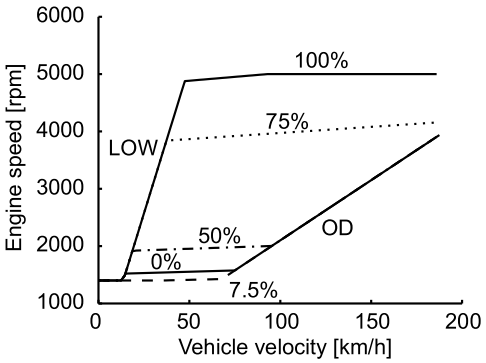

Figure 7.2: The E-line variogram for constant throttle input levels 0 [%] (–), 7.5 [%] (- -), 50 [%] (-.), 75 [%] (:) and 100 [%] (–)

pulley speed satisfies $|\dot{x}_{p,ref}| < 4$ [mm/s] during normal driving and $|\dot{x}_{p,ref}| < 6$ [mm/s] for a kickdown. During emergency braking, driveability is not of importance and then $|\dot{x}_{p,ref}| < 10$ [mm/s]. The resulting pulley speed reference is filtered using a 3^{th} order butterworth filter with a cut-off frequency of 5 [Hz].

7.2 Slip reference

The optimal efficiency of the Empact CVT is achieved at slip levels close to those corresponding to the maximum traction level of the variator. However, when trying to track this optimal slip level at low variator load torques, the required clamping force, *i.e.* secondary actuation torque T_{ms}, is relatively low. Because at this low torque level the friction in the actuation system is dominant, this leads to a loss of controllability of the slip. Therefore, it is chosen to use a lower slip reference at low variator loads, such that the minimal actuation torque T_{ms} is 0.1 [Nm]. This corresponds to a secondary clamping force of approximately 5 [kN], which is still typically two times lower than the minimum clamping force in conventional hydraulically actuated metal V-belt CVTs. Figure 7.3 illustrates the slip reference strategy for ratio $\hat{r}_g = 1.0$ [-] for varying variator load torque (Figure 7.3(c)) and with a changing actuation torque (Figure 7.3(d)). In the depicted experiment, the primary shaft speed is controlled at $\omega_p = 200$ [rad/s]. As can be seen, the slip reference increases with increasing variator load. When the primary torque T_p is smaller than 20 [Nm], the integrator state of K_3 is switched off. Although the efficiency increases significantly when the integrator state is switched on, this gain is only partly caused by the slip controller. At this low torque level, the efficiency is always relatively low.
For LOW and OD ratio, a similar slip reference is developed. The reference for other ratios is a linear interpolation between the LOW, MED and OD slip reference.

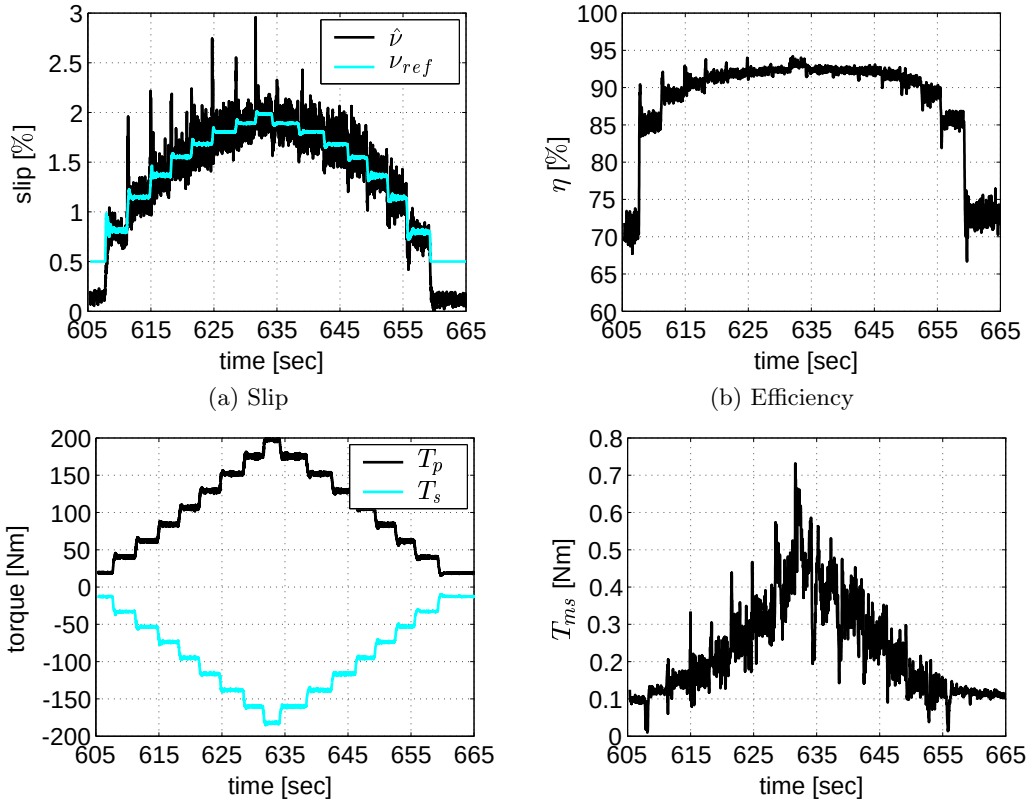

(a) Slip

(b) Efficiency

(c) Variator load torque

(d) Secondary actuator torque

Figure 7.3: Slip reference strategy at $\hat{r}_g = 1.0$ [-]

7.3 Empact FTP72 cycle performance

This section presents the results of an experiment on the test rig (Figure 2.3 and Appendix A.2) in which a part of the FTP72 cycle [66] is simulated. The FTP72 is a standardized drive cycle based on measured urban and highway traffic, developed by the US federal government, and is particularly used for fuel economy and emission testing [42].
The driver input is represented by a PI-feedback of the vehicle speed tracking error e_v, *i.e.* the difference between the FTP cycle speed and the measured speed, with a closed loop bandwidth of approximately 1 [Hz]. Although the driver would normally prescribe the accelerator or brake pedal position, here the PI-controller directly prescribes the required driveline torque. This torque demand is translated into an engine torque and vehicle brake torque. To make sure that the engine speed does not drop below the stationary speed of 764 [rpm], a proportional feedback on the engine speed is used in addition to the PI-feedback. The maximum of these controller output torques is the required engine torque and is implemented at the drive motor. The brake torque is implemented at the load motor. Furthermore, the vehicle inertia effects, tire-road load and air drag are compensated for by a feedforward compensator to obtain realistic variator load. To use the ratio reference from the variogram, the throttle position must be available. This position is reversely estimated from the Audi A3 torque map (Figure 7.1(b)) using the engine torque and speed.
Figure 7.4 shows measurement results of the first part of the FTP72 cycle. Figure 7.4(f) shows the cycle speed v_{FTP} and the realized vehicle speed v. It is not the goal here to minimize the error e_v, but is can be noted that the FTP cycle is tracked very good. Although the FTP72 cycle is a relatively dynamic driving cycle, the engine torque (Figure 7.4(d)) does not exceed approximately 100 [Nm]. As can be seen from Figure 7.4(h), the engine speed is relatively low, which is expected when using E-line tracking. The CVT ratio is depicted in Figure 7.4(a). The resulting tracking error $e_{\theta_{mp}}$ is shown in Figure 7.4(c). This error is limited to approximately 1 [rad], similar to the results presented in the previous chapter. The slip reference ν_{ref} and the realized slip $\hat{\nu}$ are shown in Figure 7.4(b). The tracking performance during (quasi-) stationary driving and during shifting is very good. Figure 7.4(e) shows the total power consumed by the actuation servomotors. At low ω_s, the power of the primary servo P_{mp} occasionally peaks to 300 [W]. The average power consumed over this cycle by this servomotor is approximately 28 [W], whereas the secondary servomotor consumes 7 [W] on the average. Together with the servopump, which provides lubrication oil and operates the TC and DNR clutches, the Empact CVT uses an average of 155 [W]. An optimally slip controlled CK2 transmission would consume approximately 280 [W] on the average at this cycle. The average power consumption of the CK2 transmission with conventional clamping force control would even be over 450 [W]. Figure 7.4(g) shows the achieved

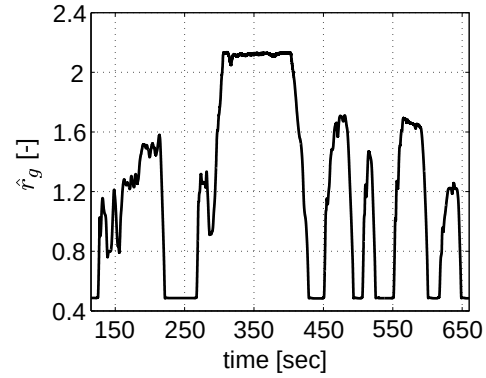

(a) CVT ratio

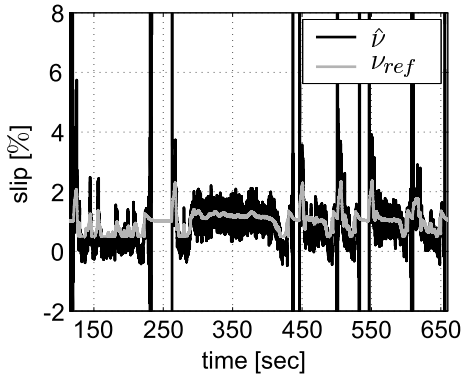

(b) Slip

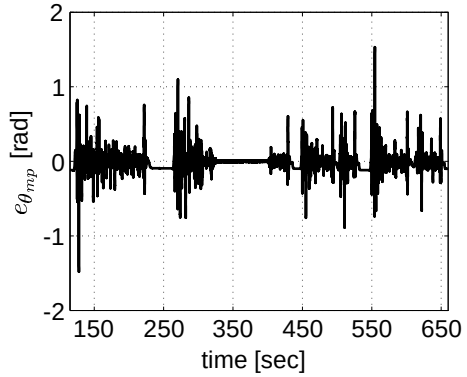

(c) θ_{mp} tracking error

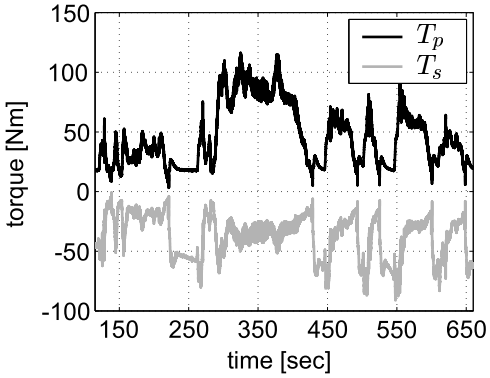

(d) Input and load torque

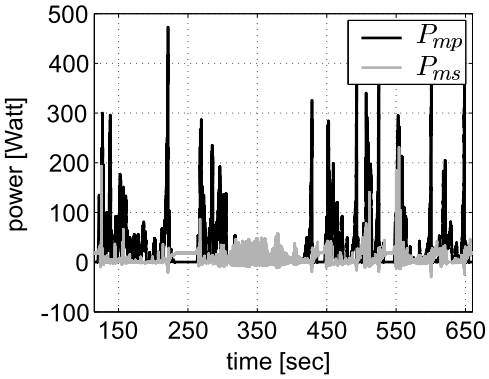

(e) Total servo power

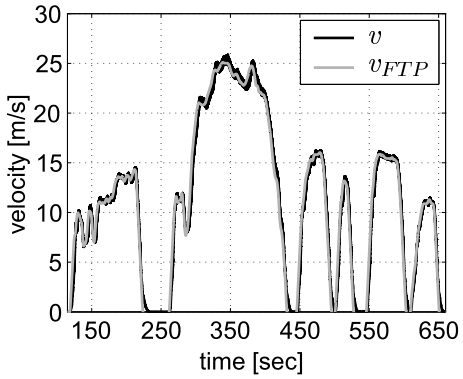

(f) Vehicle speed

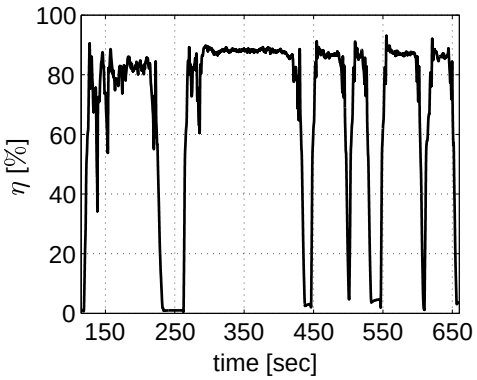

(g) Efficiency

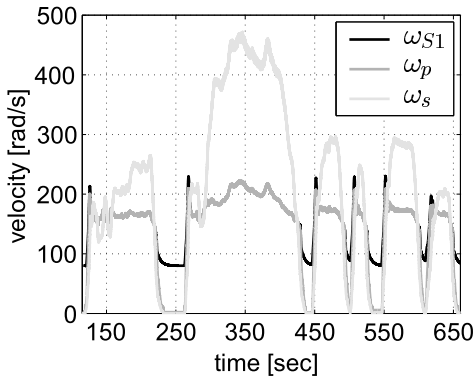

(h) Input and output velocity

Figure 7.4: Empact CVT test rig performance at the FTP72 cycle

Figure 7.5: Audi A3 2.0 FSI with Empact CVT at the chassis dyno

efficiency η of the Empact CVT at this cycle. It can be seen that even for these low input torques, an efficiency of 90 [%] is obtained, which is very close to the maximum efficiency as presented in Chapter 2. A slip controlled CK2 transmission would reach a maximum efficiency of 85 [%] in this cycle, whereas a conventionally controlled CK2 would only reach an efficiency of 80 [%].

7.4 Audi A3 implementation and performance

This section presents experimental results from the Audi A3 equipped with the Empact CVT obtained at a chassis dyno (Appendix A.3). Figure 7.5 shows a photo of the Audi A3 at this test setup. Figure 7.6 shows the Empact CVT attached to the Audi A3 engine. Details on the mechanical implementation of the Empact CVT in this vehicle will be described in [99]. Due to a failure of the end switch which detects the primary pulley end position, the overdrive ratio is here limited by software to $\hat{r}_g = 1.95$ [-] to avoid damage to the system. The chassis dyno simulates a vehicle of 1360 [kg] with rolling resistance and air drag by applying a brake torque using an Eddy Current brake. This brake has a maximum brake power of 235 [kW] at a maximum speed of 200 [km/h]. The driver manually controls both the accelerator and the brake pedal of the car.

It is not chosen to try to track a standardized drive cycle like the FTP72, because no automated steering and driving equipment is available for the chassis dyno. Instead, an arbitrary cycle is performed. In chronological order, this cycle consists of a vehicle launch, acceleration to 70 [km/h] at 55 [%] throttle position, soft braking to 12 [km/h], acceleration to 80 [km/h] at 50 [%] throttle, several short kickdowns with 60 [%] throttle and relatively fast braking to vehicle standstill. The TC clutch is closed at $t = 239$ [sec] and opened again at $t = 521$ [sec]. Figure 7.7 shows the results for the complete cycle, whereas Figure 7.8 and Figure 7.9 zoom in on the kickdowns and hard braking respectively. For the sake of compactness, the analysis below will only refer to the complete cycle, also where a reference to the kickdown

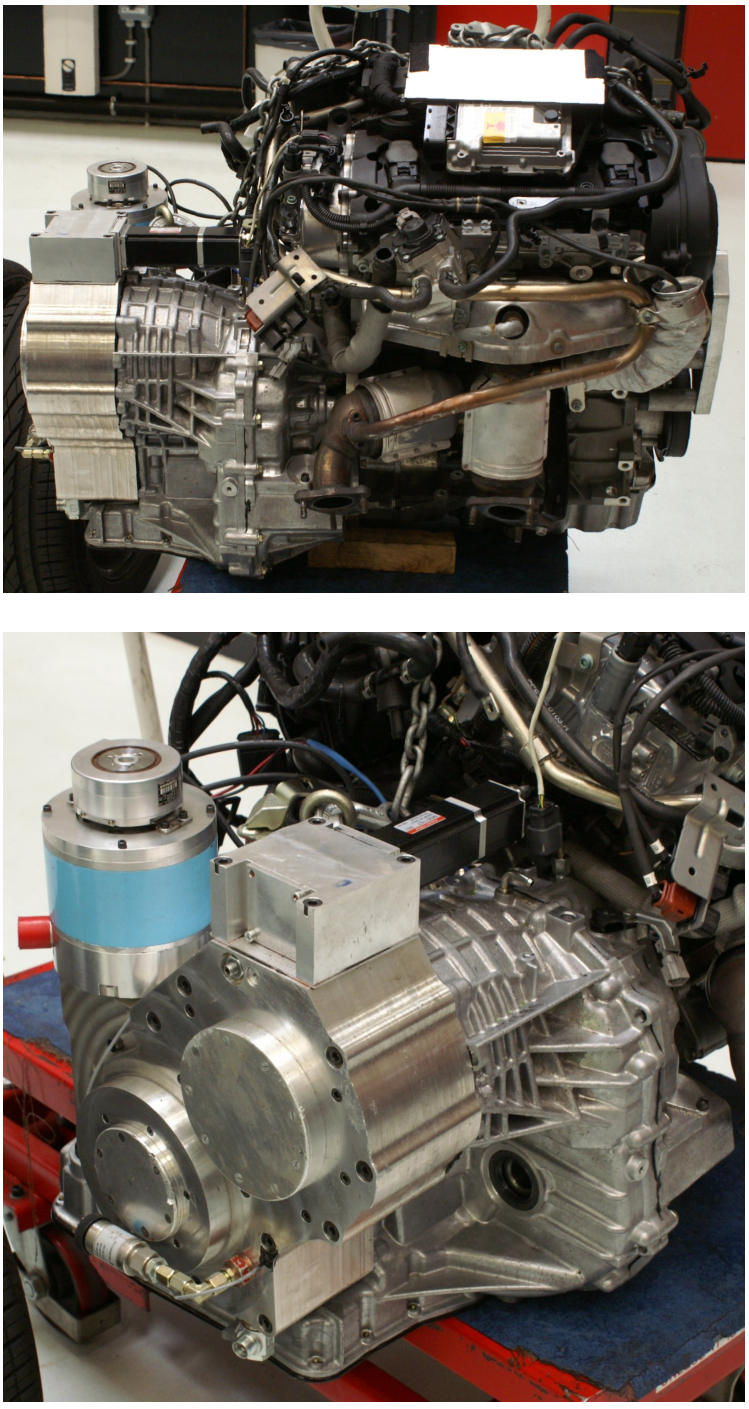

Figure 7.6: The Empact CVT attached to the Audi A3 engine

and emergency stop is applicable.
Due to the more nervous driving behavior compared to the test rig environment, the ratio tracking error $e_{\theta_{mp}}$ (Figure 7.7(c)) shows some peaks to approximately 3 [rad]. This results in a maximum tracking error of the engine speed of 30 [rpm] during these large peaks and less than 1 [rpm] during stationary driving, which is more than sufficient. The slip tracking, depicted in Figure 7.7(b), shows very good response. Some small error peaks are visible when a relatively fast change in shifting speed occurs ($|\ddot{x}_p| > 0$). These are however not troublesome and can be minimized by filtering the pulley speed reference. The switching of the controller K_3 and its integrator state is depicted in Figure 7.7(f). It can be seen that at low engine torques (Figure 7.7(d)) the integrator is switched off and at low vehicle speeds (Figure 7.7(h)) the complete controller is switched off. During the kickdowns the controller and integrator are switched on and it can be seen that the slip tracks the reference. The total power consumed by the servomotors is shown in Figure 7.7(e). It can be seen that the average consumed power is again small. During relatively fast shifting, the primary servo power P_{mp} shows peaks up to 600 [W], see also Figure 7.8(e). During the emergency brake the power exceeds 1150 [W] for a short time (Figure 7.9(e). Although this has very small effect on the total fuel consumption during ordinary driving, the effect on the size of the required servomotor is large. Reducing the secondary actuation torque (clamping force) and allowing more slip during this manoeuvre could reduce the required servo power significantly.
The efficiency of the Empact CVT can not be estimated accurately at the chassis dyno, because no direct measurements of the variator input and output torques are available. Since the ratio and slip tracking performance and the consumed servo power are comparable to the results from the test rig setup, it can be expected that the efficiency will also show comparable results.

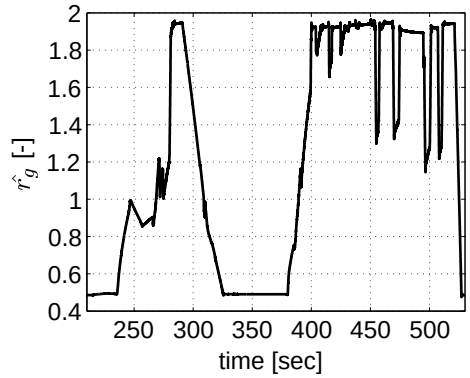

(a) CVT ratio

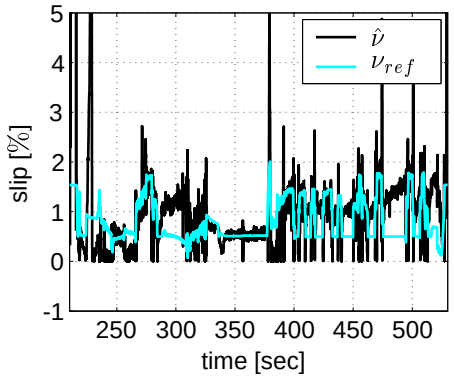

(b) Slip

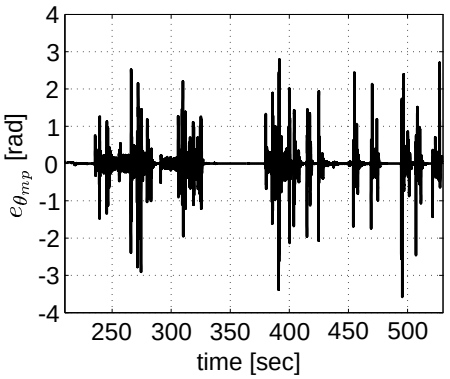

(c) θ_{mp} tracking error

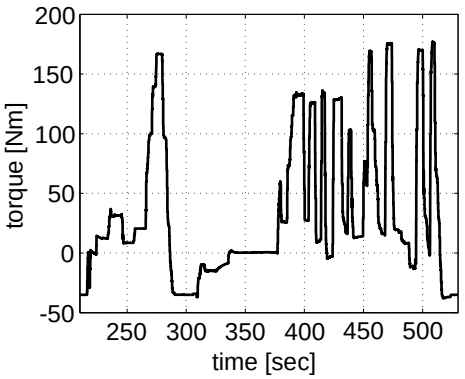

(d) Engine torque

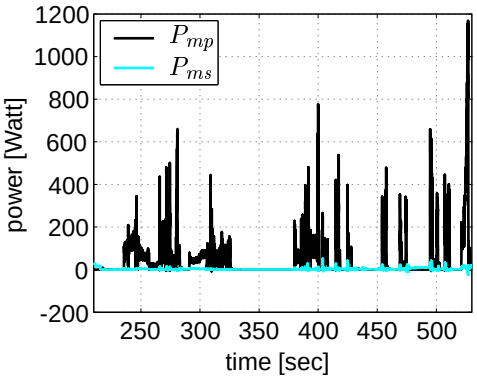

(e) Total servo power

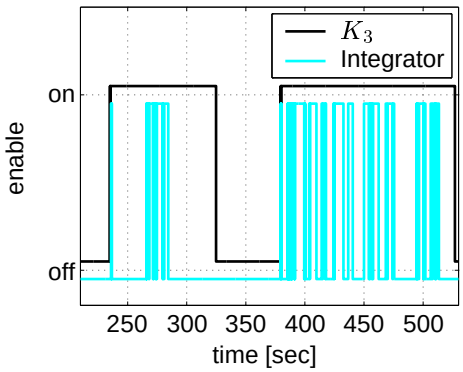

(f) Controller switching

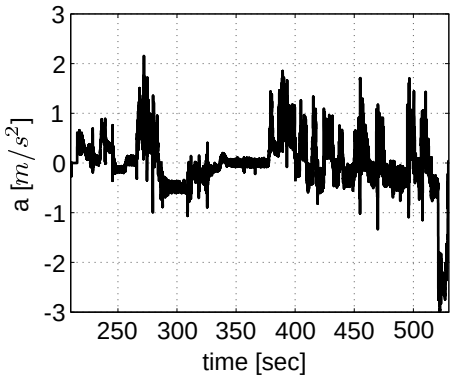

(g) Car acceleration

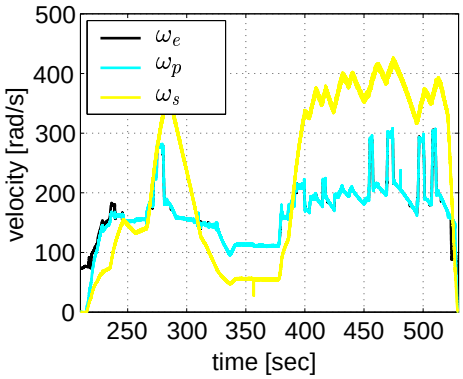

(h) Engine, input and output velocity

Figure 7.7: Audi A3 Empact performance

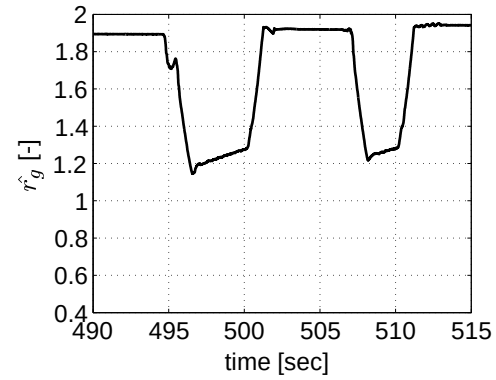

(a) CVT ratio

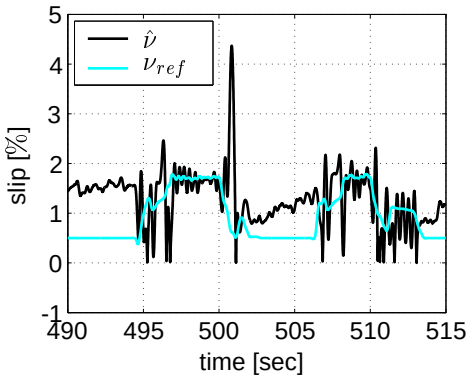

(b) Slip

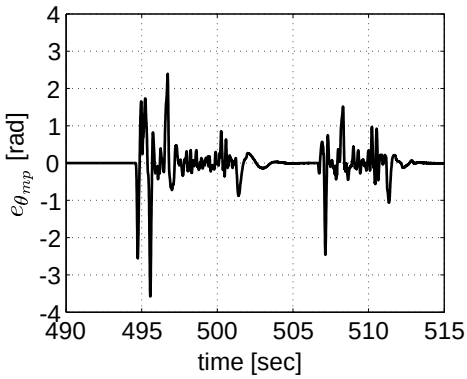

(c) θ_{mp} tracking error

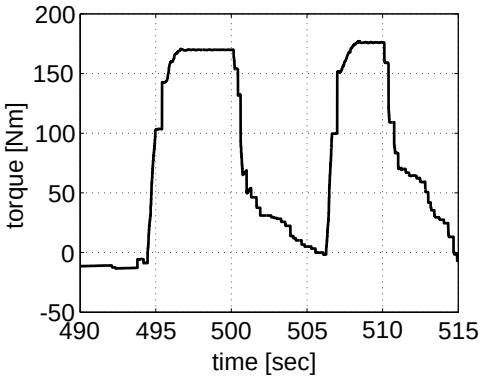

(d) Engine torque

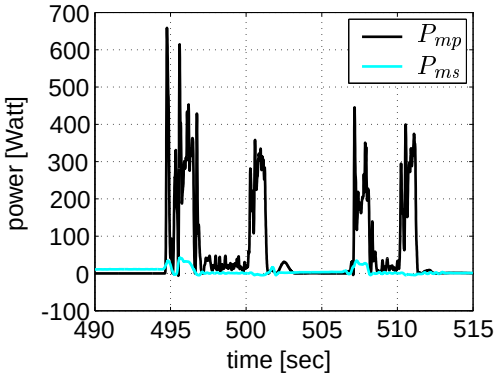

(e) Total servo power

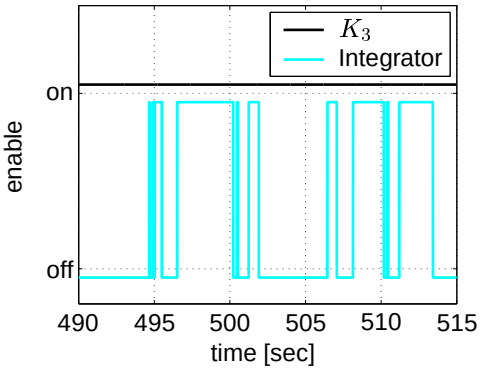

(f) Controller switching

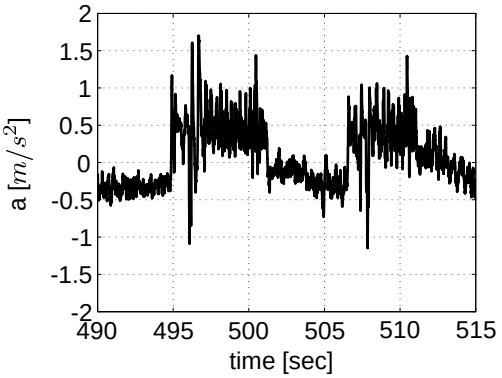

(g) Car acceleration

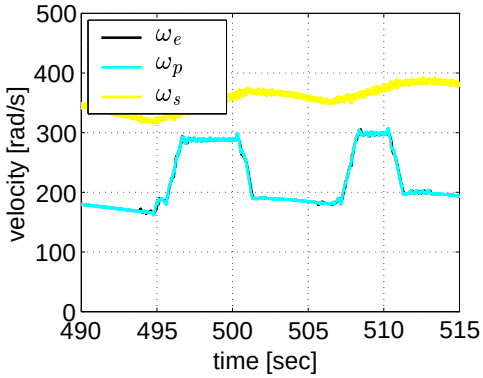

(h) Engine, input and output velocity

Figure 7.8: Audi A3 Empact performance during kickdown

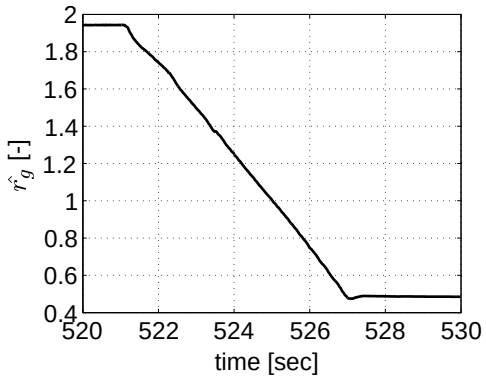

(a) CVT ratio

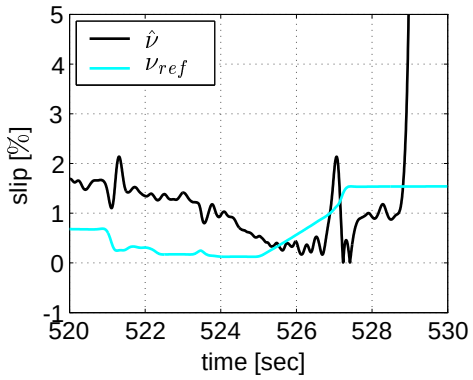

(b) Slip

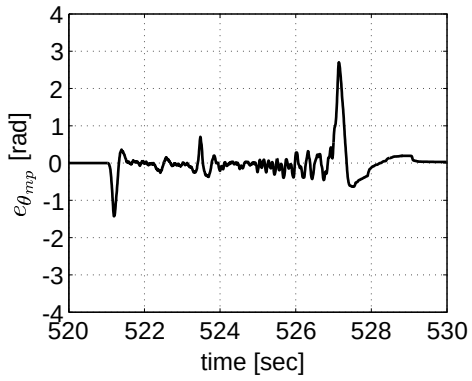

(c) θ_{mp} tracking error

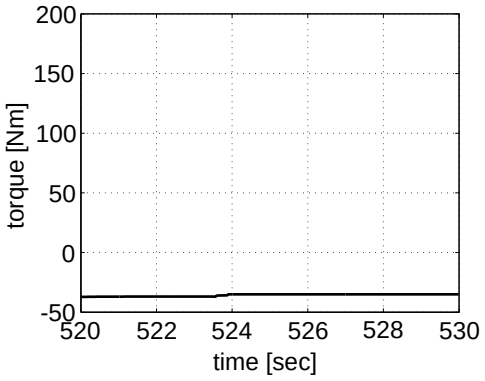

(d) Engine torque

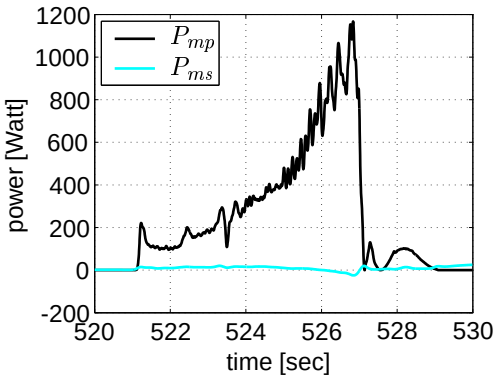

(e) Total servo power

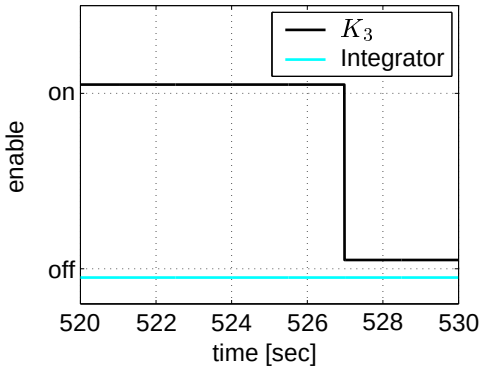

(f) Controller switching

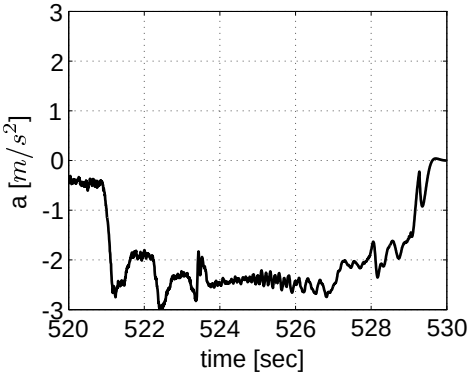

(g) Car acceleration

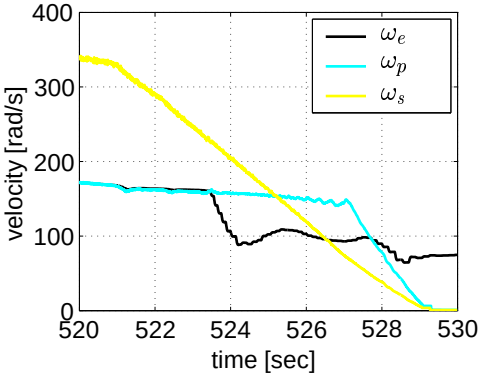

(h) Engine, input and output velocity

Figure 7.9: Audi A3 Empact performance during a hard brake

Chapter 8

Conclusions and recommendations

The large ratio coverage of CVTs combined with the possibility to choose the engine speed in a wide range independently of the vehicle speed, enables the ICE to operate at more fuel economic operating points, making the vehicle potentially more fuel efficient. Unfortunately, because the energy dissipation of the CVT itself is higher than that of a manual transmission, this efficiency improvement is partly lost. The main power losses in the CVT are due to the inefficient hydraulic actuation system and the excessive clamping forces used to prevent the belt from excessive slippage. Direct control of the slip can significantly increase the efficiency. Due to the low actuation stiffness at low hydraulic pressures, the hydraulically actuated CVT is not well suited for slip control.
In Chapter 1, the basic hypothesis of this thesis was formulated as:

> **Electromechanical actuation systems can increase the efficiency of metal V-belt CVTs, while maintaining functionality specifications.**

The Empact CVT, developed at the TU/e, has a high stiffness at low clamping forces and is suitable for slip control. This system furthermore reduces the steady-state losses, which are dominantly present in a hydraulic system.
The research objectives were formulated as:

- gain insight in the behavior of the Empact CVT by developing simulation models and by performing experiments,
- achieve optimal efficiency of the Empact CVT for steady-state and transient operation,
- track the CVT ratio reference signal, prescribed by the coordinated driveline

controller,

- prevent the pushbelt from slipping excessively under all driving conditions,
- experimentally validate the above objectives.

Based on these objectives, this chapter presents the main findings and conclusions of this research, addresses some open issues and gives some possible directions for future research.

8.1 Conclusions

The Empact CVT uses two servomotors to actuate the moveable pulley sheaves. To decouple the rotation of the input and output shaft from the servomotor rotations, a double epicyclic set is used at each shaft. Due to the direct meshing of the primary and secondary ring gear, energy can be exchanged between the moveable pulley sheaves. The system is designed, such that one (primary) actuator accounts for the ratio changes and one (secondary) actuator sets the clamping forces in the variator. In stationary situations, the consumed power is limited to electrical losses in these servomotors. Therefore, servomotors with high resistance windings are preferred. These motors have a high torque constant, resulting in a small required electrical current.

To optimally use the efficiency potential of the Empact system, the slip in the variator must be controlled. In this way, the clamping forces reduce to small values, thereby reducing the friction forces in the epicyclic sets and spindles. Efficiency improvements of up to 20 [%] can then be reached at partial load (during 75 [%] of the duration of the FTP72 cycle) compared to a conventionally controlled CK2 transmission and efficiency gains of up to 10 [%] compared to an optimally, slip controlled CK2. These results confirm the basic hypothesis.

A multi-body model of the Empact CVT is developed, which incorporates a dynamical description of all major components of the test setup. The forces between the belt and the pulleys are estimated using a continuous belt model, which gives insight in the tension and compression forces in the pushbelt. This model normally requires an iterative procedure to find the solution. Here, an explicit formulation is found, which significantly decreases the processing time. The torque exerted by the belt on the pulleys is estimated using a relation between the clamping forces, the geometrical CVT ratio and the slip dependent traction between the belt and the pulleys. Transient losses are described by a (shift direction dependent) damping on both pulleys, which represents the losses in the Shafai model. The friction losses in the Empact CVT are estimated using the LuGre friction model. Results show a realistic behavior of the system for both stationary and transient situations.

An important constraint for the controlled system is that slip cannot be controlled

under all operating conditions. At low variator speeds and low loads, the slip controller must be switched off. When slip is not controlled, the actuation system shows stick-slip behavior, which affects the driveability. To avoid this problem, the velocity of the secondary actuator is controlled. A decentralized control structure is chosen. Pairing of the in- and outputs is based on the mechanical design of the Empact CVT. The controllers are designed using a sequential loop closing procedure, in which the ratio and secondary actuator velocity loop are closed before the slip loop, such that stability of these loops is guaranteed independent of the switching of the slip controller.

A disturbance analysis showed that the desired closed loop bandwidth for slip control is 10 [Hz]. With this bandwidth large slip peaks can still be present in the variator, but these are reduced to allowable values within 0.2 [sec]. These short duration slip peaks will not result in damage of the variator and belt. A driveability study showed that good disturbance reduction of the ratio and slip controller leads to better driveability, however the ratio reference must not have spectral content above 1 [Hz]. A closed loop bandwidth of 10 [Hz] is chosen for the ratio controller, whereas a closed loop bandwidth of 20 [Hz] is chosen for the secondary actuator velocity controller.

Although the nonlinear simulation model gives a basis for control design and yields a realistic description of the closed loop system, for the actual control design an approximate, linear plant model that describes the frequency domain behavior of the system is required. These linearized descriptions are obtained from the simulation model using approximate realization from pulse response data. The pulse excitation is used, because it requires significantly less processing time than a noise or other persistently exciting signals. Furthermore, a relatively high amplitude of the signal can be used without overheating the servomotors, thereby achieving a good signal to noise ratio and reducing the effects of stick-slip due to friction. An iterative model identification and control design procedure is used, such that the plant is estimated in closed loop. In this way, the uncertainty in the frequency range of importance for the design of the controllers is reduced, which leads to less conservative control designs. Firstly, the ratio loop is closed and a plant description is obtained to design the secondary actuator velocity controller. Secondly, this control loop is closed and a plant description is obtained to design a stabilizing slip controller. Finally, the slip loop is closed and, using an iterative procedure, the plant is estimated and the slip controller is optimized, such that plant approximations are obtained for a satisfactory broad operating range. The resulting plant transfer function matrices show to be dependent on the slip and ratio. This dependency reduces when slip is controlled close to the level where optimal efficiency is reached. An interaction analysis shows diagonal dominance and provided a proper choice of input-output pairing. The mechanical design of the Empact CVT decouples the in- and outputs of the variator by the meshing of the ring gears.

Parallel to the identification and control design with the simulation model, this procedure is also applied for the test setup. Due to high measurement noise and excessive friction in the system, the quality of the approximated plants at the test setup is relatively low. The time responses are however comparable to the results from the simulation model.
In a final control design step, the ratio and slip controllers are further optimized. Using manual loop-shaping, decentralized lead-lag controllers are designed. Nominal stability and performance can be guaranteed. To obtain robust performance, gain scheduling of the slip controller is implemented. Although robust stability can not be guaranteed, it is assumed that the reference trajectory varies relatively slowly and does not excite unmodelled dynamics, such that stability is not influenced by the gain adaptation. Furthermore, thorough experimental evaluation shows a robustly stable system. Resulting closed loop bandwidth is 8-10 [Hz] for both the ratio and slip control loops. Because the slip dynamics is not well defined at low or zero variator speeds, the slip controller is switched off below 2 [km/h]. Furthermore, because the relatively high friction at low actuation torques could lead to control problems, the integrator state is switched off at low driveline torques and relatively fast downshifts. Achieving optimal efficiency at these low speeds and torques is not particularly interesting, because the effective power loss is very small.
Both the simulation model and the experimental setup show very good results for disturbance rejection and tracking performance. Torque disturbances of up to 100 [Nm], applied at the secondary variator shaft, can be suppressed within 0.2 [sec] for all ratios. The ratio tracking error is very small, below 2 [rad] for fast ratio changes, which corresponds to 0.05 [mm] in pulley position and a maximum ICE speed tracking error of less than 30 [rpm].
Experimental evaluation of the Empact CVT at the test rig showed that the average power consumption of the servomotors on the FTP72 cycle is 35 [W]. To operate the TC and DNR clutches and for lubrication, an additional 120 [W] is required. Efficiencies of 90 [%], which is close to the maximum efficiency of the Empact CVT, are reached during these experiments. Evaluation of the Empact CVT in an Audi A3 2.0 FSI shows similar performance. The required power for the servomotors during a fast deceleration exceeds 1150 [W] for a short time. Although this has a very small effect on the total fuel consumption during ordinary driving, this has large effect on the size of the required servomotor. These results prove the basic hypothesis to be correct.

8.2 Recommendations

This section gives a point by point overview of directions for further research, which can extend the knowledge gained in this project and can contribute to the research and development of fuel economic drivelines.

- The validation results from the simulation model showed a difference between estimated and measured slip. Because the chosen slip reference is based on efficiency measurements, this is not a problem in achieving optimal transmission efficiency. An investigation in the traction and slip behavior of the Empact CVT could however be of interest to match the simulation results to the measurement results.
- It is assumed that the traction coefficient is valid for both stationary and transient behavior. However, during a ratio change, the slip is resolved into a tangential and a radial component. The influence of this radial slip should be studied and incorporated in the variator models.
- A direct slip measurement could lead to better insight in the slip and ratio change dynamics and could improve the closed slip-loop performance.
- The identification and control design approach in this work is aimed at finding a control solution for the Empact CVT. Although both the identification and control design are relatively simple, fast and easy to apply methods, these show to be very effective for highly non-linear systems and systems under friction, as well as for linear systems. The approximate realization technique therefore forms a good basis for the identification and control designs for many applications.
- Optimization of the test setup, such that the noise and disturbances on the slip are minimized, could result in better identification results. In this perspective, also other identification techniques should be explored.
- The gain scheduling as proposed in this thesis should be extended to LPV control. For this reason also appropriate LPV models have to be developed.
- The long-term effects of short duration, large slip peaks on wear and damage of the belt and variator should be investigated to support the application of a slip controlled metal V-belt CVT.
- The study of the actuation system requirements for slip and ratio control should be extended with a thorough practical evaluation.
- The Empact CVT is very suitable to be used in a geared neutral transmission, because the high accuracy ratio tracking and the capability to decrease the clamping forces to minimal values. In this perspective, it is also interesting to study torque fuse capabilities of the system.

- Although the Empact CVT increases the efficiency of metal V-belt CVTs, while maintaining functionality specification, no effort is put in a cost-effective design. It is now the challenge to find a cost-effective realization that achieves performance comparable to the Empact CVT.
- To control slip in a hydraulically actuated CVT, an actuation system has to be developed using high oil pressures to obtain a stiff actuation system at low clamping forces.
- For 75 [%] of an ordinary driving cycle, the required clamping forces are relatively low. The direct support of the clamping forces by thrust bearings could become lucrative, because of the relatively low power losses at low thrust forces and low costs in comparison with the four planetary gears as used in the Empact CVT.
- Test rig measurements show an optimized efficiency of the Empact CVT with respect to the CK2, but direct fuel measurements in the test vehicle would give more insight.
- A cooperation of the engine control unit and the transmission controller is required to fully benefit from the fuel consumption reduction potential of the CVT.
- Research should be continued to address other powertrain losses, such as engine, torque converter and pushbelt losses.

Given the results from this study, as well as [9], we believe that active slip control and electromechanical actuation will make a significant and inevitable contribution to the efficiency and driving comfort of CVT based drivetrains, such that these drivetrains will outperform AT and MT based drivetrains.

Appendix A

Measurement setup

This appendix first gives a description of the Empact prototype P1 and P2 in Section A.1. The test rig measurement setup on which both prototypes are tested is described in Section A.2. Finally, Section A.3 describes the Audi A3 (with prototype P2) and chassis dyno measurement setup. Figures A.1 and A.2 schematically represent the test rig and chassis dyno setup respectively, including all measurement and command signals.

A.1 Empact prototypes

Servomotors and amplifiers

Table A.1 show a list of the servo and amplifier specifications. The primary and secondary servo for prototype P1 are of the same type. Prototype P2 uses different servo types for both actuators. The servomotor used for the oil pump is similar for both prototypes.
The oil pump servo amplifier is used in velocity mode, such that the velocity of the servo is controlled using the feedback of the Hall signals from the servo. The amplifier command input is used to prescribe the reference of the velocity of this servo. All other servo amplifiers are used in current mode, such that the amplifier controls the current to the servo. The command input of these amplifiers are used to prescribe the desired current. Current monitors are available to monitor the actual current output to the servos.
Figure A.3 shows the power supply setup for both prototypes at the test rig and in the Audi A3.

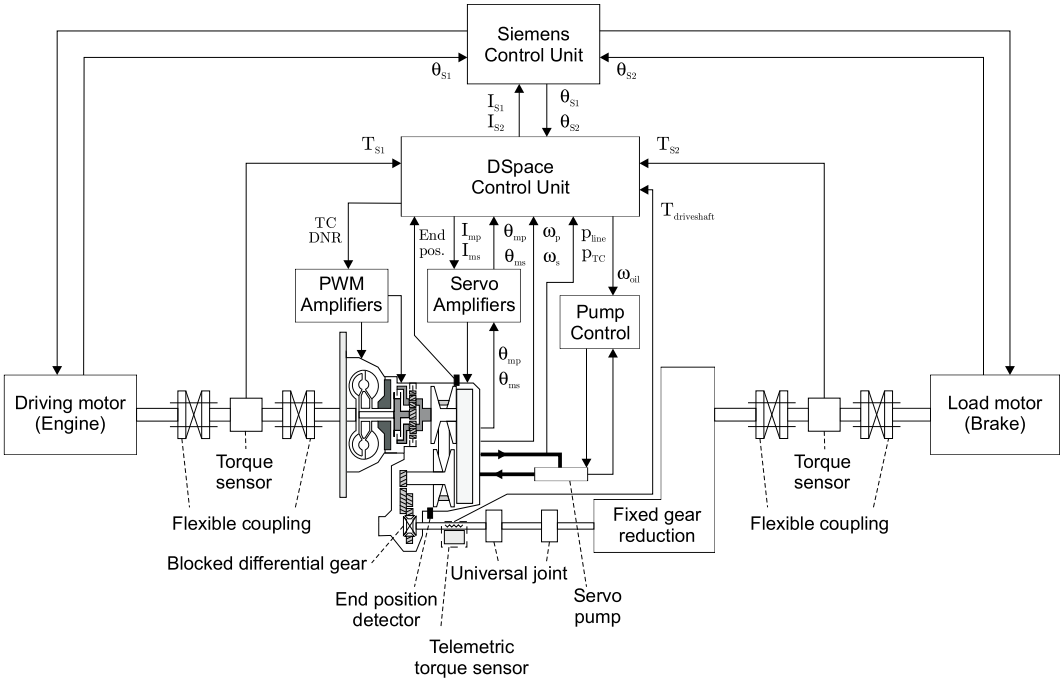

Figure A.1: Test rig measurement setup

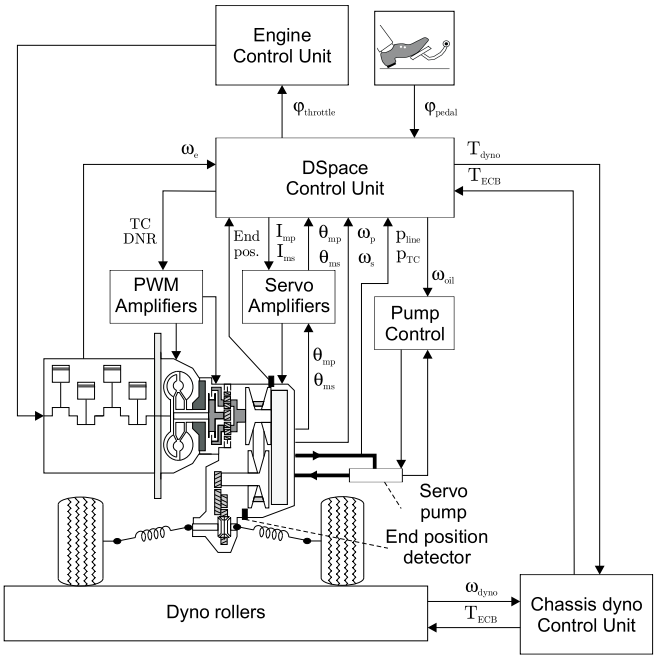

Figure A.2: Audi A3 and chassis dyno measurement setup

Table A.1: Servo and amplifier specifications

Servo	P1	P2 primary	P2 secondary	Oil pump
Manufacturer	Kollmorgen	Pacific Scientific	Maxon	Maxon
Series number	M-408-F	55NM82	EC45	EC60
Servo type	Brushless AC	Brushed DC	Brushless DC	Brushless DC
Operating Voltage	330VAC	48VDC	48VDC	48VDC
Torque Constant [Nm/A]	0.727	3.757	0.114	0.147
Voltage Constant [V/krpm]	44	17.73	8.85	15.38
Resistance of Winding [Ω]	2.61	0.65	0.659	1.12
Moment of Inertia [kgm^2]	$0.16{\cdot}10^{-3}$	$7.1{\cdot}10^{-5}$	$3.68{\cdot}10^{-5}$	$8.31{\cdot}10^{-5}$
Continuous Torque [Nm]	4.2	3.757	0.515	0.687
Max Torque [Nm]	12.9	13.2	0.829	1.0
Continuous Current [A]	4.2	23.2	4.98	5.3
Max Current [A]	20	55	7.27	13
Rated power output [W]	792	614	300	400
Number of poles	6	-	4	2
Overloading capacity [-]	3.24	3.5	1.46	1.46
Feedback signal	Resolver	-	Encoder & Hall	Hall
Amplifier	P1	P2 primary	P2 secondary	Oil pump
Manufacturer	Kollmorgen	Elmo MC	Elmo MC	Elmo MC
Series number	Servostar S610	Cello	Trumpet	Violin
Supply voltage	480VAC	56VDC	56VDC	56VDC
Rated output current [A]	10	25	15	15
Maximum output current [A]	20	50	30	30
Operating mode	Current	Current	Current	Velocity

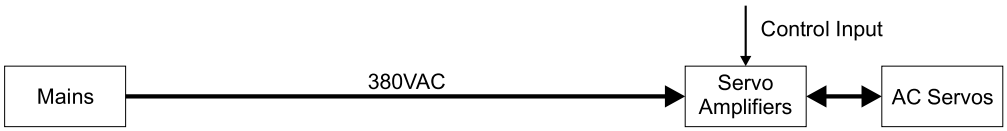

(a) P1 at test rig

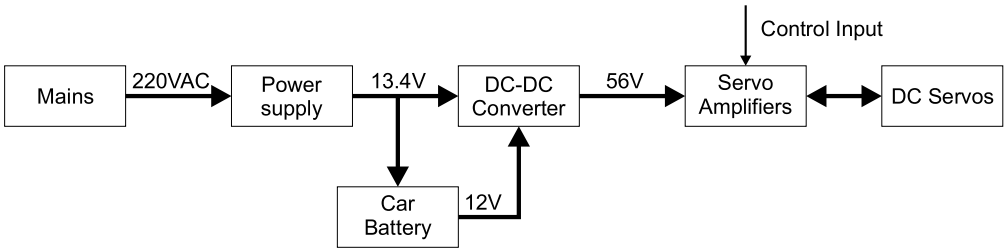

(b) P2 at test rig

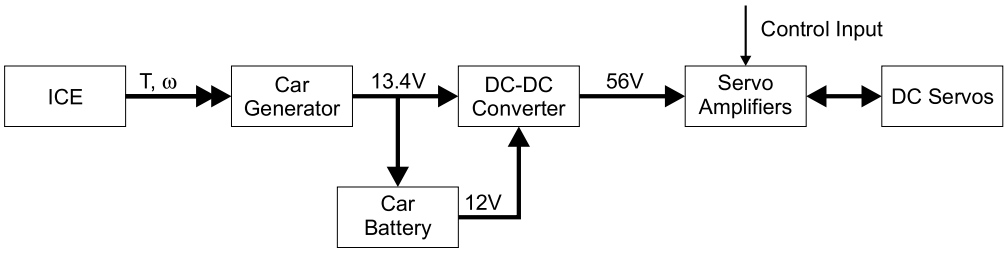

(c) P2 in Audi A3

Figure A.3: Servo Power supply

Position and velocity measurements

The Servostar S610 amplifier have a ROD encoder simulation, which converts the resolver signal used for commutation into a 2048 lines per revolution incremental encoder signal. In this way, both the primary and secondary servo position, θ_{mp} and θ_{ms} respectively, are measured in prototype P1. For commutation purposes, the secondary servomotor of P2 is equipped with a (Maxon RCM 15) rotary encoder with 2048 increments per revolution. This encoder signal is also used to measure the position θ_{ms} of the secondary servo. The primary servomotor position θ_{mp} is measured using a Heidenhain ERN 120 incremental encoder with 2048 pulses per revolution.
The primary pulley speed ω_p and the secondary pulley speed ω_s are estimated using Hall sensors, which detect the teeth of gears with 24 and 35 teeth respectively.

Miscellaneous measurements

The primary and secondary pulley are detected at their end position using inductive sensors (Baumer IFRD 08P17A1/S35L).
The line and torque converter oil pressures are measure using PTX/PMP1400 pressure sensor with a range from 1-40 [bar].
The torque converter and DNR clutch solenoids are controlled with an PWM amplifier, which translates a PWM reference signal into a PWM signal.

A.2 Test rig measurement setup

Electric Motors

The drive and load motor are Siemens asynchronous three-phase electric motors (type 1PA6184-4NL00-0GA03) with a maximum output power of 78 [kW]. The maximum power level is reached at a speed of 2900 [rpm] and can be maintained until the maximum speed of 5000 [rpm]. Up to 2900 [rpm] the maximum torque of 267 [Nm] can be supplied. Both motors are controlled by a Siemens Motion Controller. This controller feeds the power that is generated by one motor back to the other. The torque setpoints for the electric motors are supplied to the Siemens controller as analogue signals between -10 and +10 [V]. Both motors are equipped with a Heidenhain ERN 120 encoder with 1024 count per revolution.

Torque measurements

The torque between the driving motor and the torque converter is measured using a HBM T20WN torque sensor with a nominal range of -200 to 200 [Nm]. This sensor is also used to measure the torque between the load motor and the fixed gear reduction. The torque at the driveshaft is measured using strain gauges and transported

telemetrically using Astech Rotary Telemetric transmitter (TX31D/1/IFM) and receiver/decoder (RE2D/IFM/1). The nominal range of this torque measurement is -2500 to +2500 [Nm].

DSpace

A DSpace real-time data acquisition system is used, consisting of processor board DS1003, multi-channel A/D board DS2002 and DS2003, multi-channel D/A board DS2103, incremental encoder interface board DS301 and digital I/O board DS4002. The sensor signals are filtered using anti-aliasing filter with a cutoff frequency of 500 [Hz] and then acquired at a 4 [kHz] sample rate. The control program runs at a sampling frequency of 1000 [Hz]. Matlab Simulink, in combination with the real-time toolbox, is used to programm the DSpace system.

Miscellaneous equipment

The fixed gear reduction is a Nissan Primara (1997) 5-gear transmission with blocked differential gear. Depending on the speed and torque requirements of the experiment, the transmission is used in 3th gear (reduction $r_{GB} = 5.36$) or in 5th gear ($r_{GB} = 3.15$).

A.3 Audi A3 and chassis dyno measurement setup

Audi A3 2.0 FSI

The Audi A3 has a 2.0 FSI 4-cylinder engine, with a maximum power of 110 [kW] at 6000 [rpm] and a maximum torque of 210 [Nm] at 3500 [rpm]. The engine specifications are shown in Figure 7.1. The Audi A3 was originally equipped with a 6-gear manual transmission. The original configuration reaches a speed of 211 [km/h] and accelerates from 0-100 [km/h] within 9.1 [sec]. The net-weight of the car is 1275 [kg]. The engine speed ω_e is estimated by measuring frequency of the sparking plug voltage with the DSpace frequency counter.

DSpace

A DSpace Autobox real-time data acquisition system is used, consisting of processor board DS1005, multi-channel A/D board DS2002 and DS2003, multi-channel D/A board DS2103, incremental encoder interface board DS301 and digital I/O board DS4002. The sensor signals are filtered using anti-aliasing filter with a cutoff frequency of 500 [Hz] and then acquired at a 4 [kHz] sample rate. The control program runs at a sampling frequency of 1000 [Hz]. Matlab Simulink, in combination with the real-time toolbox, is used to programm the DSpace system.

Chassis dyno

The chassis dyno simulates a vehicle of 1360 [kg] with rolling resistance and air drag by applying a brake torque using an Eddy Current brake. This brake has a maximum brake power of 235 [kW] at a maximum speed of 200 [km/h]. The brake torque setpoint is supplied to the chassis dyno control unit as an analogue signal between 0 and +10 [V]. This control unit also gives an estimate of the realized brake torque.
The driver manually controls both the accelerator and the brake pedal of the car.

Miscellaneous measurements

The Audi has an electronic accelerator pedal. This signal is de-routed via the DSpace system, such that some safety precautions can be implemented. The brake pedal, ignition and DNR signals are measured.

Appendix B

Capita selecta

This appendix discusses some selected problems, to deepen the understanding of the behavior of the Empact CVT. Section B.1 presents the relation between the servomotor torques and the pulley thrust ratio, which is, amongst others, used in transient variator models. Section B.2 shows that low shaft speeds cause the slip to be uncontrollable. Inherent non-minimum phase behavior of the Empact actuation system is described in Section B.3. Finally, to study the eigenfrequencies of the system, a simplified linear model of the Empact test rig is presented in Section B.4.

B.1 Pulley thrust ratio

The stationary pulley thrust ratio is defined as

$$\kappa = \frac{F_p^*}{F_s} \tag{B.1}$$

where F_p^* is the clamping force needed to maintain a stationary CVT ratio. The pulley thrust ratio is often used as a characteristic variator property in CVT evaluation and (ratio) control design [59], [28], [81], [17], [2], [114].
In the Empact CVT, with neglected friction, κ can be expressed as a function of the primary and secondary servomotor torques according to

$$\kappa = \frac{T_{ms} r_s - T_{mp} r_p}{T_{ms} r_s} \quad ; \quad r_p = \frac{r_w}{sz} \quad ; \quad r_s = \frac{r_r r_c}{sz} \tag{B.2}$$

where r_p is the reduction from primary servo to the primary pulley and r_s is the reduction from secondary servo to the secondary pulley. T_{mp} can then be expressed as a function of T_{ms} according to

$$T_{mp} = (\kappa - 1)\, T_{ms} \frac{r_s}{r_p} \tag{B.3}$$

If $\kappa = 1$ (*i.e.* if the primary and secondary thrust force are in balance), the secondary actuation torque is completely supported by the meshing gears and as a result $T_{mp} =$

0 [Nm]. In the variator of the CK2 transmission $0.5 < \kappa < 2$. For the chosen reduction r_s and r_p in the Empact prototype, the torque to maintain a certain stationary CVT ratio is then limited to $|T_{mp}| = 2$ [Nm] at $T_{ms} = 0.6$ [Nm]. This actuation force corresponds to a clamping force of $F_s = 30$ [kN], for which an engine torque of $T_e = 260$ [Nm] can be transmitted in OD.

B.2 Slip dynamics

The slip dynamics is given by

$$\dot{\nu} = -\frac{\dot{r}_s r_g - r_s \dot{r}_g}{r_g^2} \tag{B.4}$$

where the rate of change of the speed ratio is given by

$$\dot{r}_s = \frac{\dot{\omega}_s \omega_p - \omega_s \dot{\omega}_p}{\omega_p^2} \tag{B.5}$$

and the rate of change of the geometric ratio $\dot{r}_g$ is given by the Shafai transient variator model [88], [9]. By substituting (B.5) into (B.4), the slip dynamics are given by

$$\dot{\nu} = \frac{(\dot{\omega}_p \omega_s - \omega_p \dot{\omega}_s)}{\omega_p^2 r_g} + \frac{\omega_s \dot{r}_g}{\omega_p r_g^2} \tag{B.6}$$

As can be seen from this relation, for small velocity $\dot{\nu} \simeq 1/\omega_p$, hence for $\omega_p \to 0$, the slip dynamics becomes infinitely fast with infinite high-frequency gain. This leads to a loss of controllability and the slip controller must be switched off for small ω_p. This will be an important requirement for the control system, as will be described in Chapter 4. Petersen [76] describes the same situation for wheel slip control in ABS systems.
If an absolute measure for slip is used, the slip dynamics would not be inversely proportional to ω_p and would not become infinitely fast at low speeds. Switching of the slip controller would then still have to be applied, considering the fact that the relative error of the velocity measurements at low speeds is high and therefore quality of the slip estimation would be poor.

B.3 Inverse response of slip during ratio changes

An important property of the variator is that, while shifting, the displacements x_p and x_s of the moveable pulley sheaves are not equal. By combining (3.9) and (3.10), the difference $\Delta_x = x_p - x_s$ in translation between both pulleys can be written as

$$\Delta_x = 2a \sin(\varphi) \tan(\beta) \tag{B.7}$$

where $\Delta_x = x_p - x_s$. This means that if the variator shifts from low to medium ratio $\Delta_x > 0$, whereas for ratio shifts from medium to overdrive $\Delta_x < 0$.

Now consider the situation when the secondary servo actuation position is constant. If the ratio is changed by means of only rotating the primary servo, the translation of both pulleys would be equal. However, when shifting from low to medium $\Delta_x > 0$. As a result the length of the belt ((3.7)) decreases, and with that, according to the clamping force model, the clamping force in the system decreases. This can be seen from (3.12) and the derivation of the clamping forces thereafter. As a result, the slip in the system would increase. If the ratio is changed from medium to overdrive, $\Delta_x < 0$, L and F_s increase, hence the slip decreases. Of course when shifting from overdrive to low the opposite is true.
If a small ratio change is applied and a constant torque T_{ms} is applied at the secondary servo, the slip would first change as described above and then stabilize at a constant value. Hence, with respect to the relation between T_{mp} and ν, this phenomenon results in an inverse response if $\Delta_x < 0$.

B.4 Linear system analysis

For better understanding of the dynamics of the actuation system, this section presents a simplified linear model of the Empact CVT and the test rig. The main difference with the earlier presented simulation model, is the implementation of the variator model. The clamping force model presented in Section 3.2.2 is not used in this analysis. Now the pushbelt is represented by a linear spring with stiffness k_{bt}. This approximation only holds for small perturbations of the moveable pulley sheaves around a certain operating point. This furthermore implies that the inverse response behavior is neglected in this model, because $\Delta_x = 0$. The elongation of the spring is given by (3.10).
The rotational coupling of the primary and secondary pulley in the simulation model is based on (3.24) and (3.25), *i.e.* the transmitted belt torque. Linearization of (3.24) with respect to the rotational shaft velocities ω_p and ω_s around a certain operating point, defined by a given geometric ratio r_{g_0}, a nominal slip ν_0 and a nominal clamping force F_{s_0}, results in

$$\tilde{T}_{s,i} = c_{br}\left(\frac{\omega_{s_0}}{\omega_{p_0}}\tilde{\omega}_p - \tilde{\omega}_s\right) \quad ; \quad c_{br} = \frac{2\mu'(\nu_0, r_{g_0})F_{s_0}R_{p_0}}{\omega_{p_0}\cos(\beta)r_{g_0}} \tag{B.8}$$

where $\mu'(\nu_0, r_{g_0})$ is the slope of the traction curve at the corresponding slip value ν_0 and ratio r_{g_0}, $\tilde{\omega_p}$ and $\tilde{\omega_s}$ are small perturbation around the nominal shaft speeds ω_{p_0} and ω_{p_0}. The speed ratio in this relation is given by $r_{s_0} = \frac{\omega_{s_0}}{\omega_{p_0}}$. F_{s_0} results from the nominal slip value ν_0 and constant ratio r_{g_0} for a given T_{s_0}. Hence, the rotational coupling between the primary and secondary shaft can be modeled as a linear damper with damping constant c_{br} [Ns/rad]. As a result, the system is stable for positive μ', however at negative μ' the damping constant also becomes negative, which could lead to unstable behavior.
The linear model presented in this section further incorporates all linear elements

of the simulation model. The kinetic energy is the summation of the individual contribution of all masses and inertias in the Empact test rig. The potential energy in the system consists of the contributions of the torsional spring between the primary servo and the primary worm gear, the spring at the secondary side of the actuation system (representing the chain reduction), the springs that represent the thrust bearings, the torque converter spring, the spring between the final drive reduction and the fixed gear reduction and the spring that accounts for the elasticity of the pushbelt. Viscous friction is modeled using the Rayleigh damping description [5], [21]. In the non-conservative energy also the (linear) Shafai damping from (3.27) and the linear belt damping ((B.8)) is incorporated. The vector of generalized coordinates is given by

$$\underline{q}^T = [\theta_p \quad \theta_{mp} \quad \theta_{arp} \quad x_p \quad \theta_s \quad \theta_{ms} \quad \theta_{ars} \quad x_s \quad \theta_d \quad \theta_l] \tag{B.9}$$

where θ_d and θ_l are the rotational positions of the driving motor and load motor respectively. Furthermore, a vector of external non-conservative forces is defined according to

$$\underline{F}_{ext}^T = [0 \quad T_{mp} \quad 0 \quad 0 \quad 0 \quad T_{ms} \quad 0 \quad 0 \quad T_d \quad -T_l] \tag{B.10}$$

where T_d is the torque of the driving motor and T_l is the torque of load motor. By applying Lagrange equations to the kinetic energy function, the potential energy function and the non-conservative energy function, the resulting equation of motion which describes the complete system can be given by

$$M\ddot{\underline{q}} + D\dot{\underline{q}} + K\underline{q} = \underline{F}_{ext} \tag{B.11}$$

where M is the symmetric, positive, constant mass matrix, K is the symmetric, semi-positive stiffness matrix and D is the symmetric, semi-positive damping matrix.

Undamped eigenmodes

Using the mass matrix M and the stiffness matrix K and neglecting the damping matrix D, the undamped eigenfrequencies f_r and corresponding eigenvectors can be

f_r #	LOW [Hz]	MED [Hz]	OD [Hz]
1	8.7	7.7	7.3
2	21.1	21.0	21.1
3	25.0	24.9	24.9
4	48.9	49.0	49.1
5	77.5	76.8	76.0

Table B.1: Undamped eigenfrequencies

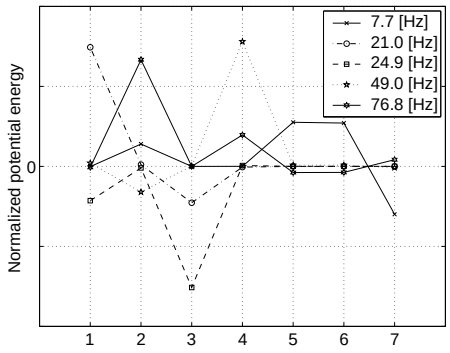

Figure B.1: Normalized potential energy of spring elements at $r_g = 1$. #1 = worm, #2 = chain, #3 = TC, #4 = driveshaft, #5 = variator belt, #6 = primary thrust bearing and #7 = secondary thrust bearing spring element

calculated. Due to the fact that in the calculation of the undamped eigenmodes no power dissipation is present, there is no coupling between the primary and secondary shaft ($c_{br} = 0$). In this case three rigid body modes are present, *i.e.* a rotation of the primary shaft, a rotation of the secondary shaft and a rigid body mode of the actuation system where the rotation of the primary servo results in a translation of both moveable pulley sheaves. Furthermore five low frequency (f_r <100 [Hz]) and four high frequency modes are present. These eigenfrequencies depend slightly on the CVT ratio. Table B.1 shows the eigenfrequencies for LOW, MED and OD. To get an impression of these mode shapes, Figure B.1 shows the normalized potential energy of the nine elastic elements in each of the first five modes. The sign of the energy shows whether the corresponding spring is elongated or shortened.
The lowest eigenfrequency at $f_r = 7.7$ [Hz] originates from the deformation of the chain transmission in the secondary actuation, in combination with the deformation of thrust bearings and the belt and with the bending of the pulleys. The bearings, belt and pulleys themselves are fairly stiff, but due to the large reductions in the system, they greatly contribute to the flexibility. The second eigenfrequency at $f_r = 21.0$ [Hz] originates mainly from the flexibility of the worm transmission at the primary actuator. This mode is also influenced by the torque converter stiffness. The third mode at $f_r = 24.9$ [Hz] is the rotating mode of driving motor, torque converter stiffness and primary shaft. The fourth resonance at $f_r = 49.0$ [Hz] is the rotating mode of the secondary shaft, driveshaft and load motor. The sixth mode in the relevant frequency range at $f_r = 76.8$ [Hz] originates from the deformation of the chain in the secondary actuation. The high frequency eigenmodes result from the translating parts of the actuation system. These modes are beyond the frequency range of interest and are left out of consideration in this thesis.

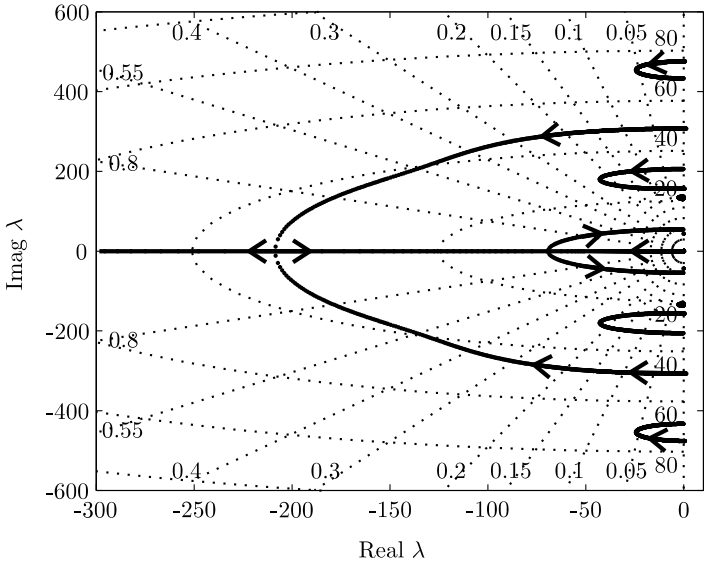

Figure B.2: Root locus of poles for $\nu = 4$ [%] to $\nu = 0$ [%] at $r_{g_0} = 1$

Effect of belt coupling on the eigenfrequencies

Physically speaking, when $c_{br} = 0$, the system operates at the top of the traction curve ($\mu' = 0$). No rotational coupling between the primary and secondary shaft is present in this situation. If the clamping force is increased at this point, slip is decreased and the damping constant is increased. A rotational coupling between the primary and secondary shaft arises.

Figure B.2 shows the root locus of the low frequency poles of the system for decreasing slip, from 4 [%] to 0 [%] at $r_{g_0} = 1$, $\omega_{p_0} = 100$ [rad/s] and a nominal belt torque of $T_{s_0} = 200$ [Nm]. The damping coefficient c_{b_r} increases from small negative values for $\nu = 4$ [%] to positive values. One could expect the poles of the system to be located in the right half plane for negative c_{br}, resulting in an open loop unstable system. However due to viscous friction in the system, the eigenvalues are damped such that they turn to the stable left half plane. It can be seen that the damping of the complex pole pair at 49.0 [Hz] increases as it turns back towards the real axis. At the real axis, one of these poles moves to $-\infty$, whereas the other tends towards the imaginary axis. Due to the increasing coupling between the primary and secondary shaft, one of the rigid body mode poles moves from 0 towards negative real values. At approximately 11 [Hz], these two real poles become one complex pair. A further increase of the damping makes this pole pair turns towards the imaginary axis. The primary and secondary shaft are coupled in this case. From the two rigid body modes of the driveline, only one remains. The mode of the primary shaft is also influenced by the belt coupling and shifts from 24.9 [Hz] to 32.7 [Hz]. The modes at 6.0 [Hz] and at 21.0 [Hz] hardly are influenced by the belt coupling. The resonance from the secondary actuator and chain stiffness shifts from 75.7 [Hz] to 68.9 [Hz].

Bibliography

[1] K. Abo, M. Kobayashi, and M. Kurosawa. Development of a metal belt-drive CVT incorporating a torque converter for use with 2-liter class engines. *SAE Technical Paper 980823*, 1998.

[2] S. Akehurst, N.D. Vaughan, D.A. Parker, and D. Simner. Modelling of loss mechanisms in a pushing metal V-belt continuously variable transmission. part 1: torque losses due to band friction. *Proc. Instn Mech. Engrs Vol. 218 Part D: J. Automobile Engineering*, pages 1269–1281, 2004.

[3] P. Albertos and A. Sala. *Multivariable Control Systems*. Springer-Verlag, 2004.

[4] Audi. www.audi.com. Website, 2005.

[5] H. Benaroya and B. Benaroya. *Mechanical Vibrations*. CRC Press, 2004.

[6] G.H. Benedict and B.W. Kelley. Instantaneous coefficients of gear tooth friction. *ASLE Transactions*, 4:59–70, 1961.

[7] B. Bertsche, H. Naunheimer, and G. Lechner. *Fahrzeuggetriebe*. Springer-Verlag, 1994.

[8] I.J.M. Besselink and A.J.C. Schmeitz. The mf-swift tyre model: extending the magic formula with rigid ring dynamics and an enveloping model. *JSAE review*, 26(2):245–252, 2005.

[9] B. Bonsen. *Efficiency optimization of the push-belt* CVT *by variator slip control*. PhD thesis, Technische Universiteit Eindhoven, 2006.

[10] B. Bonsen, T.W.G.L. Klaassen, R.J. Pulles, S.W.H. Simons, M. Steinbuch, and P.A. Veenhuizen. Performance optimization of the push-belt CVT by variator slip control. *Int. J. of Vehicle Design*, 39:232–256, 2005.

[11] B. Bonsen, T.W.G.L. Klaassen, K.G.O. van de Meerakker, M. Steinbuch, and P.A. Veenhuizen. Measurement and control of slip in a continuously variable transmission. In *Proceedings of IFAC Mechatronics*, Sydney, Australia, 2004.

[12] B. Bonsen, T.W.G.L. Klaassen, K.G.O. van de Meerakker, P.A. Veenhuizen, and M. Steinbuch. Analysis of slip in a continuously variable transmission. In *Proceedings of Imece*, number 41360, 2003.

[13] B. Bonsen, P.A. Veenhuizen, and M. Steinbuch. CVT ratio control strategy optimization. *Proceedings of the Conference on Vehicle Power and Propulsion (VPP'05)*, 2005.

[14] O.H. Bosgra. Physical modelling for systems and control. *Lecture Notes for the Eindhoven University of Technology, Department of Mechanical Engineering*, 2004.

[15] T.H. Bradley and A.A. Frank. Servo-pump hydraulic control system performance and evaluation for CVT pressure and ratio control. *Proc. of VDI* CVT *2002 Congress*, (VDI-Berichte 1709):35–41, 2002.

[16] C. Canudas de Wit, P. Tsiotras, X. Claeys, J. Yi, and R. Horowitz. *Nonlinear and Hybrid Systems in Automotive Control*, chapter Friction Tire/Road Modeling, Estimation and Optimal Braking Control, pages 147–210. Springer, 2003.

[17] G. Carbone, L. Mangialardi, and G. Mantriota. Theoretical model of metal v-belt drives during rapid ratio changing. *Journal of Mechanical Design*, 123:111–117, mar 2001.

[18] G. Carbone, L. Mangialardi, and G. Mantriota. The influence of pulley deformations on the shifting mechanism of metal belt CVT. *Journal of Mechanical Design*, 127:103–113, 2004.

[19] C. Chan, D. Yang, T. Volz, D. Breitweiser, F.S. Jamzadeh, A. Frank, and T. Omitsu. System design and control considerations of automotive continuously transmissions. *SAE Paper 840048*, 1984.

[20] G.A. Commissaris. Validation of clamping force models using the power loop test rig. Master's thesis, Technische Universiteit Eindhoven, DCT-2005.111, 2005.

[21] B. de Kraker and D.H. van Campen. *Mechanical Vibrations*. Shaker Publishing, 2001.

[22] M. Deacon. *The control of a passenger car diesel engine and* CVT. PhD thesis, University of Bath, 1996.

[23] M. Deacon, C.J. Brace, M. Guebeli, N.D. Vaughan, C.R. Burrows, and R.E. Dorey. A modular approach to the computer simulation of a passenger car powertrain incorporating a diesel engine and continuously variable transmission. *IEE International conference on control*, 1994.

[24] Van Doorne. *dr. Hub J. van Doorne*. VDT, 2000.

[25] H. Faust, M. Homm, and M. Reuschel. Efficiency-optimised CVT hydraulic and clamping system. In *Proc. of VDI* CVT *2002 Congress*, number VDI-Berichte 1709, pages 43–58, 2002.

[26] J. Freudenberg and R. Middleton. Design rules for multivariable feedback systems. In *Proc. of the 35th Conference on Decision and Control*, Kobe, Japan, December 1996.

[27] J. Freudenberg, R. Middleton, and Anna Stefanopoulou. A survey of inherent design limitations. In *Proc. of the American Control Conference*, Chicago, Illinois, U.S.A., December 2000.

[28] T. Fujii, T. Kurokawa, and S. Kanehara. Study of a metal pushing v-belt type CVT, part 1: Relationship between transmitted torque and pulley thrust. *SAE transactions*, 930666, 1993.

[29] J. Gebert and F. Kuecuekay. Schaltkomfort als neue regelgroesse bei pkw-automaten-getrieben. *Symposium: Steuerungssysteme fuer den Antriebsstrang*, 1997.

[30] G. Gerbert. Mechanism of a metal V-belt. *ASME paper no. 84-DET-227*, 1984.

[31] M. Gevers, B.D.O. Anderson, and B. Codrons. Issues in modeling for control. In *Proc. of the American Control Conference*, Philadelphia, Pennsylvania, U.S.A., June 1998.

[32] P. Grosdidier and M. Morari. Interaction measures for systems under decentralized control. *Automatica*, 22(3):309–320, 1986.

[33] J. Lee H. Kim. Analysis of belt behavior and slip characteristics for a metal V-belt CVT. *Mechanics and Machine Theory, Vol 29, No 6*, 1994.

[34] T.A. Harris. *Rolling Bearing Analysis*. John Wiley & Sons, Inc., 2001.

[35] R.H.A. Hensen. *Controlled Mechanical Systems with Friction*. PhD thesis, Technische Universiteit Eindhoven, 2002.

[36] B.L. Ho. *An effective Construction of Realizations from Input/Output Descriptions*. PhD thesis, Standford University, California, 1966.

[37] C.H. Houpis and S.J. Rasmussen. *Quantitative Feedback Theory*. Marcel Dekker Inc., 1999.

[38] M. Hovd and S. Skogestad. Sequential design of decentralized controllers. *Automatica*, 30(10):1601–1607, 1994.

[39] T. Ide. Effect of power losses of metal V-belt CVT components on the fuel economy. *Int. Congress on Continuously Variable Power Transmimssion* CVT *'99*, pages 93–98, 1999.

[40] T. Ide, A. Udagawa, and R. Kataoka. A dynamic response analysis of a vehicle with a metal v-belt CVT. In *Proceedings of the 2nd Internat. Symp. on Advanced Vehicle Control*, pages 230 – 235, 1994.

[41] N. Indlekofer, U. Wagner, A. Fidlin, and A. Teubert. Latest results in the CVT development. *7th LuK Symposium*, pages 51–60, 2002.

[42] R. Joumard and E. Sérié. Modelling of cold start emissions for passenger cars. Technical Report LTE 9931, INRETS, 1999.

[43] A. Kahraman, D.R. Houser, and H. Xu. Development of a generalized mechanical efficiency prediction methodology for gear pairs. Technical report, The Ohio State University, Department of Mechanical Engineering, 2005.

[44] I. Kamwa and L. Gérin-Lajoie. State-space system identification - toward mimo models for modal analysis and optimization of bulk power systems. *IEEE Transactions on Power Systems*, 15(1):326–335, February 2000.

[45] K. Kanokogi and H. Hoshino. Simulation of metal pushing type v-belt for CVT. In *Proceedings of the 15th ADAMS European User Conference*, 2000.

[46] B.W. Kelley and A.J. Lemanski. Lubrication of involute gearing. In *Proc. ImechE Conf. on Lubrication and Wear*, volume 182, pages 173–184, 1967.

[47] T.W.G.L. Klaassen, B. Bonsen, K.G.O. van de Meerakker, M. Steinbuch, P.A. Veenhuizen, and F.E. Veldpaus. Nonlinear stabilization of slip in a continuously variable transmission. In *Proceedings of CCA*, Taipei, Taiwan, 2004.

[48] T.W.G.L. Klaassen, B. Bonsen, K.G.O. van de Meerakker, B.G. Vroemen, P.A. Veenhuizen, and M. Steinbuch. Dynamic analysis of the Empact CVT. In VDI, editor, *Dynamik und Regelung von Automatischen Getrieben*, Leonberg bei Stuttgart, Germany, 2005.

[49] T.W.G.L. Klaassen, B. Bonsen, K.G.O. van de Meerakker, B.G. Vroemen, P.A. Veenhuizen, and M. Steinbuch. Control-oriented identification of an electromechanically actuated pushbelt type CVT. In Frank, editor, *Proceedings of International Continuously Variable and Hybrid Transmission Congress*, pages CD–ROM, Davis, CA, United States, 2004.

[50] T.W.G.L. Klaassen, B. Bonsen, K.G.O. van de Meerakker, B.G. Vroemen, P.A. Veenhuizen, F.E. Veldpaus, and M. Steinbuch. The empact CVT: Modeling, simulation and experiments. *Accepted for publication in Int. Journal*

of Modelling, Identification and Control, Special Issue on Advanced Control Systems in Automotive Applications, 2006.

[51] T.W.G.L. Klaassen and M. Steinbuch. Identification and control of the empact CVT. *Accepted for publication in IEEE Transactions on Control Systems Technology*, 2007.

[52] T.W.G.L. Klaassen, B.G. Vroemen, B. Bonsen, K.G.O. van de Meerakker, M. Steinbuch, and P.A. Veenhuizen. Modelling and simulation of an electromechanically actuated pushbelt type continuously variable transmission. In *Proceedings of IFAC Mechatronics*, number 95, Sydney, Australia, 2004.

[53] T.W.G.L. Klaassen, B.G. Vroemen, B. Bonsen, K.G.O. van de Meerakker, M. Steinbuch, and P.A. Veenhuizen. Modelling and control of an electromechanically actuated pushbelt type continuously variable transmission. In *Proceedings of AVEC*, Arnhem, the Netherlands, 2004.

[54] D. Kobayashi, Y. Mabuchi, and Y. Katoh. A study on the torque capacity of a metal pushing v-belt for CVTs. *SAE Technical papers*, (980822), 1998.

[55] D. Kostić. *Data-driven robot motion control*. PhD thesis, Eindhoven University of Technology, 2004.

[56] S.Y. Kung. A new identification and model reduction algorithm via singular value decomposition. In *Proceedings of the* 12*th Asilomar Conference on Circuits, Systems and Computers*, pages p. 705 – 714, California, USA, 1978.

[57] W. Lebrecht, H. Ulbrich, H. Seckler, and U. Duhr. Transiente verstelldynamik von CVT-keilkettengetrieben. In *Proc. of Dynamik und Regelung von automatischen Getrieben*, number VDI-Berichte 1917, pages 247–268, 2005.

[58] G. Lechner and H. Naunheimer. *Automotive Transmissions*. Springer-Verlag, 1999.

[59] H. Lee and H. KIM. Analysis of primary and secondary thrusts for a metal-belt CVT-part 1: New formula for speed ratio-torque-thrust relationship considering band tension and block compression. *SAE transactions*, 109(6):1240–1248, 2000.

[60] D.J. Leith and W.E. Leithead. Comments on the prevalence of linear parameter varying systems. Technical report, Department Electronic and Electrical Engineering, University of Strathclyde, Glasgow, Scotland, 1999.

[61] D.J. Leith and W.E. Leithead. Survey of gain-scheduling analysis and design. *Int. Journal of Control*, 73(11):1001–1025, 2000.

[62] S. Liu and B. Paden. A survey of today's CVT controls. *Proc. of the 36th CDC conference, San Diego, USA*, 1997.

[63] L. Ljung, editor. *System identification (2nd ed.): theory for the user*. Prentice Hall PTR, Upper Saddle River, NJ, USA, 1999.

[64] LuK. www.luk.com. Website, 2005.

[65] T. McKelvey. *Identification of State-Space Models from Time and Frequency Data*. PhD thesis, Dept. of Electrical Engineering, Linköping University, 1995.

[66] M. Montazeri-Gh and M. Naghizadeh. Development of car drive cycle for simulation of emissions and fuel economy. In *Proceedings 15th European Simulation Symposium*, Delft, The Netherlands, October 2003.

[67] D.H. Müller. *Kettengetriebe*. BIK, Bremer Intitut für Konstruktionstechnick, Universität Bremen, 2000.

[68] H. Olsson, K.J. Åström C. Canudas de Wit, M. Gäfvert, and P. Lischinsky. Friction models and friction compensation. *European Journal of Control*, 4(3):176–195, 1998.

[69] H. Olsson, K.J. Åström, C. Canudas de Wit, M. Gäfvert, and P. Lischinsky. Friction models and friction compensation. Technical report, Lund University, 1997.

[70] H. Olsson, K.J. Åström, C. Canudas de Wit, M. Gafvert, and P. Lischinsky. Friction models and friction compensation. Technical report, Lund Institute of Technology, 1997.

[71] M. Osawa. Basic analysis towards further development of continuously variable transmissions (overview). *R&D Review of Toyota CRDL*, 2005.

[72] A. Palmgren. *Ball and roller bearing engineering*. Philadelphia: SKF Industries Inc., 1959, 1959.

[73] L.H.P.G. Peeters. Actuation system design specifications for a variator slip controlled CVT. Master's thesis, Technische Universiteit Eindhoven, DCT-2006.130, 2006.

[74] E. Pennestrí and P.P. Valentini. A review of formulas for the mechanical efficiency analysis of two degrees-of-freedom epicyclic gear trains. *Journal of Mechanical Design*, 125:602–608, 2003.

[75] B. Pennings, M.D. Tran, M. Derks, J. Feijtel, J.v. Lith, A. Brandsma, and M.v. Schaik. New CVT pushbelt design to cover all front wheel drive powertrains. *Internationales CTI Symposium*, 2005.

[76] I. Petersen, T.A. Johansen, J. Kalkkuhl, and J. Lüdemann. Wheel slip control in abs brakes using gain scheduled constrained LQR. In *Proceedings of European Control Conference*, Porto, Portugal, 2001.

[77] I. Petersen, T.A. Johansen, J. Kalkkuhl, and J. Lüdemann. *Nonlinear and Hybrid Systems in Automotive Control*, chapter Wheel Slip Control in ABS Brakes using Gain-scheduled Constrained LQR, pages 125–146. Springer, 2003.

[78] I. Petersen, T.A. Johansen, J. Kalkkuhl, and J. Lüdemann. Wheel slip control using gain-scheduled LQ - LPV/LMI analysis and experimental results. In *Proceedings of European Control Conference*, Cambridge, UK, 2003.

[79] R. Pfiffner and L. Guzella. Optimal operation of CVT-based powertrains. *Int. J. Robust nonlinear control*, 2001.

[80] J.E. Rijnsdorp. Interaction in two-variable control distillation columns - i. *Automatica*, 1:15–28, 1965.

[81] W. Ryu, J. Nam, Y. Lee, and H. Kim. Model based control for a pressure control type CVT. *Int. J. Vehicle Design*, 39(3):175–188, 2005.

[82] H. Sattler. Efficiency of metal chain and v-belt CVT. In *Int. Congress on Continuously Variable Power Transmission (*CVT*'99)*, Eindhoven, The Netherlands, 1999.

[83] A.J.C. Schmeitz. *A Semi-Empirical Three-Deminesional Model of the Pneumatic Tyre Rolling over Arbitrarily Uneven Road Surfaces.* PhD thesis, TU Delft, 2004.

[84] P. Schoeggl and E. Ramschak. Vehicle driveability assessment using neural networks for development, calibration and quality tests. *SAE 2000 World Congress Detroit, Michigan March 6-9, 2000, SAE Technical Papers 2000-01-0702.*, 2000.

[85] B. De Schutter. Minimal state-space realization in linear system theory: an overview, special issue on numerical analysis in the 20th century: Vol. i, approximation theory. *Journal of Computational and Aplied Mathematics*, vol. 121(1-2):pp. 331–354, January 2000.

[86] L.F. Schwab. Development of a shift quality metric for an automatic transmission. *SAE, paper no. 941009*, 1994.

[87] A. Serrarens. *Coordinated control of the ZI Powertrain.* PhD thesis, Technische Universiteit Eindhoven, 2001.

[88] E. Shafai, M. Simons, U. Neff, and H.P. Geering. Model of a continuously variable transmission. *JSAE no 9636330*, (9636330), 1995.

[89] J. Shamma and M. Athans. Guaranteed properties for nonlinear gain scheduled control systems. In *Proceedings of the 27th IEEE Conference on Decision and Control*, pages 2202–2208, Austin, Texas USA, December 1988.

[90] S. Shastri and A.A. Frank. Comparison of energy consumption and power losses of a conventionally controlled CVT with a servo-hydraulic controlled CVT and with a belt and chain as the torque transmitting element. *Proceedings of the International* CVT *and Hybrid Transmission Congress*, 2004.

[91] S. Skogestad and I. Postlethwaite. *Multivariable Feedback Control, analysis and design*. John Wiley & Sons, 2005.

[92] J. Srnik and F. Pfeiffer. Dynamics of CVT chain drives. *Int. J. of Vehicle Design*, 22:54–72, 1999.

[93] D.J. Stilwell and W.J. Rugh. Stability preserving interpolation methods for the synthesis of gain scheduled controllers. *Automatica*, 36:665–671, 2000.

[94] K. Suzuki and K. Tanaka. Torque converter with lock-up cluths by bond graphs. In *2003 International Conference on Bond Graph Modeling and Simulation*, 2003.

[95] M. Takahashi, R. Kido, K. Nonaka, M. Takayama, and T. Fujii. Design and development of a dry hybrid belt (BANDO AVANCE) for CVT vehicles. *International Congress on Continuously Variable Power Transmission Proceedings*, 1999.

[96] D.J. Trudnowski, J.R. Smith, T.A. Short, and D.A. Pierre. An application of prony methods in pss design for multimachine systems. *IEEE Transactions on Power Systems*, 6(1):118–126, February 1991.

[97] M.C. Tsangarides and W.E. Tobler. Dynamic behavior of a torque converter with centrifugal bypass clutch. *SAE transactions*, 94:490–504, 1985.

[98] H. Vahabzadeh and S.M. Linzell. Modeling, simulating and control implementation for a split-torque, geared neutral,infinitely variable transmission. *SAE Paper 910409*, 1991.

[99] K.G.O. van de Meerakker. *Design of the Empact* CVT. PhD thesis, Technische Universiteit Eindhoven, To appear.

[100] K.G.O. van de Meerakker and P.C.J.N. Rosielle. Continuously variable transmission. *Patent: WO2004057215*, 2004.

[101] K.G.O. van de Meerakker, P.C.J.N. Rosielle, B. Bonsen, T.W.G.L. Klaassen, and N.J.J. Liebrand. Mechanism proposed for ratio and clamping force control in a CVT. In *Proceedings of Fisita, Barcelona, Spain*, number F2004F108, 2004.

[102] M. van der Laan, M. van Drogen, and A. Brandsma. Improving push belt CVT efficiency by control strategies based on new variator wear insight. In *Proceedings of CVHT*, Davis, CA, USA, 2004.

[103] M. van Drogen and M. van der Laan. Determination of variator robustness under macroslip conditions for a pushbelt CVT. In *Proceedings of SAE World congress*, number 41360, Detroit, USA, 2004.

[104] J.B. van Helmont, A.J.J. van der Weiden, and H. Anneveld. Design of optimal controllers for a coal fired benson boiler based on a modified approximate realization algorithm. In *Proceedings of Application of Multivariable System Techniques*, pages 313 – 320, London, UK, 1990. Elsevier.

[105] P. van Overschee and B. de Moor. Closed loop subspace system identification. In *Proc. of the 36th Conference on Decision and Control*, San Diego, California, U.S.A., December 1997.

[106] P. van Overschee, B. de Moor, W. Dehandschutter, and J. Swevers. A subspace algorithm for the identification of discrete time frequency domain power spectra. *Automatice*, 33(12):2147–2157, 1997.

[107] J. van Rooij and A.A. Frank. Development of a 700 nm chain-CVT for a parallel hybrid driveline. *Proceedings of the* CVT *2002 Congress*, 2002.

[108] VDT. www.bosch.com. Website, 2006.

[109] P.A. Veenhuizen, B. Bonsen, T.W.G.L. Klaassen, and P.H.W.M. Albers. Pushbelt CVT efficiency improvement potential of servo-electromechanical actuation and slip control. In Frank, editor, *Proceedings of International Continuously Variable and Hybrid Transmission Congress*, pages CD–ROM, Davis, CA, United States, 2004.

[110] P. Velex and V. Cahouet. Experimental and numerical investigations on the influence of tooth friction in spur and helical gear dynamics. *Journal of Mechanical Design*, 122:515–522, dec 2000.

[111] B.G. Vroemen. *Component Control for the Zero Inertia powertrain.* PhD thesis, Eindhoven University of Technology, 2001.

[112] V. Wicke. *Driveability and control aspects of vehicles with continuously variable transmissions.* PhD thesis, 2001.

[113] H. Xu, A. Kahraman, and D.R. Houser. A model to predict friction losses of hypoid gears. *American Gear Manufacturers Association*, (05FTM06), 2005.

[114] M. Yamamoto, T. Wakahara, H. Okahara, and H. Oshita. Hydraulic system, shift and lockup clutch controls developed for a large torque capacity CVT. In *Proceedings of CVHT*, Davis, CA, USA, 2004.

[115] O. Yaniv. *Quantitative Feedback Design of Linear and Nonlinear Control Systems*. Kluwer Academic Publishers, 1999.

[116] T. Yuki, M. Takayama, and H. Kato. Development of dry hybrid belt CVT. *JSAE Review*, 16:251–256, 1995.

[117] Y. Zhu. *Multivariable System Identification*. Pergamon (Elsevier Science), 2001.

Nomenclature

Symbol	*Description*	*Unit*
a	shaft distance	[m]
b_s	Shafai damping constant	[Nms/mm]
b_{tc}	TC capacity factor	[Nms^2/rad^2]
$c_{pump,CK2}$	flow per rotation constant of the CK2 oil pump	[m^3/rad]
F_B, F_C	centrifugal force of bands, blocks	[N]
$F_{act,p}$, $F_{act,s}$	primary, secondary actuation force	[N]
F_p, F_s	primary, secondary clamping force	[N]
i_{FDR}	Final Drive Reduction ratio	[-]
k_{mp}, k_{ms}	primary, secondary servo torque constant	[Nm/A]
L	belt length	[m]
L_0	nominal belt length	[m]
m_s	mass of moveable pulley sheave	[kg]
P_{acc}	hydraulic power to operate the accessories	[W]
$P_{act,CK2}$	total actuation power in the CK2	[W]
$P_{act,Empact}$	total actuation power in the Empact	[W]
$P_{act,min}$	minimally required mechanical power	[W]
P_{in}, P_{out}	transmission input, output power	[W]
$p_{line,CK2}$	Line pressure of the CK2	[Pa]
$P_{mp,elec}$, $P_{ms,elec}$	primary, secondary electrical servo power	[W]
$P_{mp,mech}$, $P_{ms,mech}$	primary, secondary mechanical servo power	[W]
P_{mp}, P_{ms}	primary, secondary servo power	[W]
P_{Shafai}	Shafai shifting power	[W]
Q, Q^p, Q^s	belt compression force	[N]
Q_0	maximum compression force	[N]

R_0	nominal running radius	[m]
r_c, r_r, r_w	chain, reduction gear, worm transmission ratio	[-]
r_g	geometric ratio	[-]
R_p, R_s	primary, secondary running radius	[m]
r_s	speed ratio	[-]
R_{mp}, R_{ms}	primary, secondary servo winding resistance	[Ω]
r_{tc}	TC speed ratio	[-]
s	screw pitch	[rad/m]
S	tension force	[N]
S^p, S^s	belt tension force along primary, secondary pulley	[N]
S_0, S_1	lower, upper tension force	[N]
T_{LuGre}	friction torque	[Nm]
T_{mp}, T_{ms}	primary, secondary servo torque	[Nm]
$T_{p,i}$, $T_{s,i}$	internal primary, secondary variator shaft torque	[Nm]
T_p, T_s	primary, secondary shaft torque	[Nm]
$T_{tc,out}$	TC output torque	[Nm]
v_{belt}	belt speed	[m/s]
x_p, x_s	primary, secondary pulley position	[m]
$x_{n,p}$, $x_{n,s}$	primary, secondary nut position	[m]
z	average bristle deflection	[rad]
z	ratio of annulus and sun gear radii	[-]
α_{tc}	TC torque amplification factor	[-]
β	pulley wedge angle	[rad]
ΔL	belt elongation	[m]
η	variator efficiency	[%]
η_{CK2}	C2 efficiency	[%]
η_{Empact}	Empact efficiency	[%]
κ	pulley thrust ratio	[-]
μ	traction coefficient	[-]
μ_1	friction coefficient between bands and blocks	[-]
μ_2	friction coefficient between blocks and pulleys	[-]
ν	slip	[%]
ω_e	engine speed	[rad/s]
ω_{mp}, ω_{ms}	primary, secondary servo speed	[rad/s]
ω_p, ω_s	primary, secondary shaft speed	[rad/s]
$\omega_{tc,in}$, $\omega_{tc,out}$	TC input, output speed	[rad/s]
σ_0	bristle stiffness	[Nm/rad]

σ_1	bristle damping	[Nms/rad]
σ_2	viscous damping	[Nms/rad]
θ	coordinate along angle of wrap	[rad]
$\theta_{\alpha,\beta,\gamma}$	rotation of Empact gear	[rad]
φ	$(\pi - \varphi_p)/2$	[rad]
φ_1, φ_2	active primary, secondary compression arc	[rad]
φ_p, φ_s	primary, secondary angle of wrap	[rad]

Subscripts and superscripts

Symbol	*Description*
act	actuation
mp	primary servo
ms	secondary servo
$mech$	mechanical part
$elec$	electrical part
p	primary
s	secondary
$\alpha = \{a, c, p, s\}$	annulus, carrier, planet, sun
$\beta = \{l, r\}$	left, right
$\gamma = \{p, s\}$	primary, secondary

Acronyms

Symbol	*Description*
AMT	Automated Manual Transmission
AT	Automatic Transmission
BSFC	Brake Specific Fuel Consumption
BTS	Bedrijfs Technologische Samenwerking
CK2	Jatco CVT ransmission
CVT	Continuously Variable Transmission
DC	Direct Current
DNR	Drive Neutral Reverse gear
ECM	Engine Control Module
FDR	Final Drive Reduction
FTP	Federal Testing Procedure
LOW	Lowest transmission ratio
MED	Transmission ratio one
MT	Manual Transmission

NEDC	New European Driving Cycle
OD	Highest transmission ratio (Overdrive)
OR	Overdrive Reverse
OOL	Optimal Operation Line
TC	Torque Converter
TCM	Transmission Control Module
UD	Underdrive
UR	Underdrive Reverse
WOT	Wide Open Throttle

Summary

The large ratio coverage of a CVT and the possibility to choose the engine speed in a wide range independently of the vehicle speed enables the ICE to operate at more fuel economic operating points, making the vehicle potentially more fuel efficient. Unfortunately, because the energy dissipation of the CVT itself is higher than that of a manual transmission, this efficiency improvement is partly lost. The main power losses in the CVT are due to the inefficient hydraulic actuation system and the excessive clamping forces used to prevent the belt from excessive slippage. Direct control of the slip can significantly increase the efficiency. Due to the low actuation stiffness at low hydraulic pressures, the hydraulically actuated CVT is not well suited for slip control.

The Empact CVT, developed at the TU/e, is an electromechanically actuated pushbelt type CVT, which has a high stiffness at low clamping forces and is suitable for slip control. This system reduces the steady-state losses, which are dominantly present in a hydraulic system.

The goals of this research are to achieve optimal efficiency of this system, to obtain good tracking performance and to prevent the pushbelt from slipping excessively. These objectives are experimentally validated at a Empact prototype, which is tested at a test rig and implemented in an Audi A3 2.0 FSI.

The Empact CVT uses two servomotors to actuate the moveable pulley sheaves. To decouple the rotation of the input and output shaft from the servomotor rotations, a double epicyclic set is used at each shaft. The system is designed, such that one (primary) actuator accounts for the ratio changes and one (secondary) actuator sets the clamping forces in the variator.

To optimally use the efficiency potential of the Empact system, the slip in the variator must be controlled. In this way, the clamping forces reduce to small values, thereby reducing the friction forces in the gears, spindles and bearings. Efficiency improvements of up to 20 [%] can then be reached at partial load (during 75 [%] of the duration of the FTP72 cycle) compared to a conventionally controlled CK2

transmission and efficiency gains of up to 10 [%] compared to an optimally, slip controlled CK2.

To gain insight in the physical behavior of the Empact CVT, a multi-body model of the system has been developed, which incorporates a dynamical description of all major components of the test setup. Results show a realistic behavior of the system for both stationary and transient situations. Although this nonlinear simulation model gives a basis for control design and yields a realistic description of the closed loop system, for the actual control design an approximate, linear plant model that describes the frequency domain behavior of the system is estimated. These linearized descriptions are obtained from the simulation model using approximate realization from pulse response data. An iterative model identification and control design procedure is used, such that the plant is estimated in closed loop. In this way, the uncertainty in the frequency range of importance for the design of the controllers is reduced, which leads to less conservative control designs.

Parallel to the identification and control design with the simulation model, this procedure is also applied for the test setup. Due to high measurement noise and excessive friction in the system, the quality of the approximated plants at the test setup is relatively low. The time responses are however comparable to the results from the simulation model.

An important constraint for the controlled system is that slip cannot be controlled under all operating conditions. At low variator speeds and low loads, the slip controller must be switched off. A decentralized control structure is chosen. Pairing of the in- and outputs is primarily based on the mechanical design of the Empact CVT and are supported by a interaction analysis. The controllers are designed using a sequential loop closing procedure, in which the slip loop is closed last, such that stability of other loops is guaranteed independent of the switching of the slip controller. Using manual loop-shaping, decentralized lead-lag controllers are designed. Nominal stability and performance can be guaranteed. To obtain robust performance, gain scheduling of the slip controller is implemented. Resulting closed loop bandwidth is 8-10 [Hz] for both the ratio and slip control loops. Because the slip dynamics is not well defined at low or zero variator speeds, the slip controller is partly switched off below 2 [km/h].

Both the simulation model and the experimental setup show very good results for disturbance rejection and tracking performance. Torque disturbances of up to 100 [Nm], applied at the secondary variator shaft, can be suppressed within 0.2 [sec] for all ratios. The ratio tracking error is very small compared to conventional CVT systems.

Experimental evaluation of the Empact CVT at the test rig showed that the average power consumption of the Empact CVT on the FTP72 cycle is 155 [W], whereas conventional hydraulically actuated CVTs consume over 400 [W] on the average at this drive cycle. Efficiencies of 90 [%], which is close to the maximum efficiency of

the Empact CVT, are reached during these experiments. Evaluation of the Empact CVT in an Audi A3 2.0 FSI shows similar performance. Overall, an efficiency improvement of up to 10 [%] is obtained with the Empact CVT compared to a comparable size hydraulically actuated CVT.

Samenvatting

Het grote ratio bereik van een continu variabele transmissie (CVT) en de mogelijkheid om in een groot bereik de snelheid van de verbrandingsmotor onafhankelijke te kiezen van de voertuigsnelheid, maakt het mogelijk om de verbrandingsmotor in meer brandstof efficiënte werkpunten te laten werken. Hierdoor is het voertuig potentieel zuiniger dan met een manuele transmissies (MT) of een automatische transmissies (AT). Echter, omdat het energiegebruik van de CVT zelf hoger is dan dat van een MT, gaat deze energiewinst gedeeltelijk verloren. De grootste vermogensverliezen in de CVT zijn toe te wijden aan de inefficiënte hydraulische actuatie en de excessieve knijpkrachten die gebruikt worden om de duwband van te grote slip te weerhouden. Directe regeling van de slip kan de efficiëntie aanzienlijk verbeteren, doordat er dan veel lagere knijpkrachten toegepast kunnen worden. Door de lage actuatiestijfheid bij lage hydraulische drukken, is de hydraulisch geactueerde CVT echter niet geschikt om slip regeling toe te passen.

De Empact CVT, ontwikkeld op de TU/e, is een elektromechanisch geactueerde duwband type CVT, welke een hoge stijfheid heeft bij lage knijpkrachten en is uitermate geschikt om slipregeling toe te passen. Dit systeem vermindert daarmee de stationaire verliezen, die dominant aanwezig zijn in een hydraulisch systeem.

De doelstellingen van dit onderzoek zijn om optimale efficiëntie met het Empact systeem te behalen, om goed volggedrag van de voorgeschreven CVT ratio te realiseren en om te voorkomen dat de duwband te grote slip vertoont. Deze doelstellingen zijn experimenteel gevalideerd op een prototype van de Empact CVT, welke getest is op een testbank opstelling en geïmplementeerd in een Audi A3 2.0 FSI.

De Empact CVT gebruikt twee servomotoren om de beweegbare pulleyschijven te actueren. Om de rotatie van deze motoren te ontkoppelen van de ingaande en uitgaande as van de CVT, wordt een dubbele planetaire tandwielset gebruikt op iedere as. Het systeem is zo ontworpen, dat een actuator de ratio verstelling op zich neemt en een actuator de knijpkracht in het systeem bestuurt.

Om optimaal gebruik te kunnen maken van het efficiëntie potentieel van de Empact

CVT, dient de slip in de variator geregeld worden. Op deze manier worden de knijpkrachten verlaagd tot kleine waardes, zodat de wrijvingskrachten in de tandwielen, spindels en lagers worden geminimaliseerd. De efficiëntie kan dan met 20 [%] verhoogd worden bij gedeeltelijke belasting (gedurende 75 [%] van de totale cyclustijd van de FTP72 cyclus) in vergelijking met een conventioneel geregelde CK2 transmissie en met meer dan 10 [%] in vergelijking met een optimale, slip geregelde CK2.
Om inzicht te krijgen in het fysieke gedrag van de Empact CVT is een multi-body model van het systeem ontwikkeld, waarin de dynamische eigenschappen van de gehele testopstelling geïntegreerd zijn. De resultaten laten een realistisch gedrag van het systeem zien, voor zowel stationaire als transiënte situaties. Hoewel dit niet-lineaire simulatiemodel een basis legt voor regelaar ontwerp en een realistische beschrijving geeft van het geregelde gedrag, is voor het werkelijke regelaar ontwerpproces een benaderde, lineaire systeembeschrijving benodigd, welke het dynamische gedrag van het systeem beschrijft in het frequentiedomein. Deze gelineariseerde beschrijvingen zijn verkregen vanuit het simulatiemodel door het toepassen van benaderde realisatie op pulsresponsies van het systeem. Een iteratieve identificatie en regelaarontwerp procedure is toegepast, zodat het systeem is benaderd in gesloten lus. Op deze manier wordt de onzekerheid van de benadering geminimaliseerd in het relevante frequentiegebied voor het ontwerp van de regelaars.
Parallel aan de identificatie en regelaarontwerp op het simulatiemodel is deze methode ook toegepast op de testopstelling. Door de hoge meetruis en grote wrijvingsverliezen in het systeem, is de kwaliteit van de benaderde systemen op de opstelling relatief laag. De tijdsresponsies laten echter zeer overeenkomende resultaten zien in vergelijking met de tijdsresponsies van het simulatiemodel.
Een belangrijke beperking voor het geregelde systeem, is dat de slip niet onder alle operationele condities geregeld kan worden. Bij lage CVT snelheid en lage belas-ting moet de slipregeling uitgeschakeld worden. Er is voor een gedecentraliseerde regeling gekozen. Keuze van de in- en uitgangen is primair gebaseerd op het mechanische ontwerp van de Empact CVT, maar wordt onderbouwd door een interactie analyse. De regelaars zijn ontworpen met een sequential loop closing procedure. Hierin is de slip regellus het laatst gesloten, zodat de stabiliteit van de andere regellussen gegarandeerd kan worden, onafhankelijk van het schakelen van de slip regeling. De gedecentraliseerde lead-lag regelaars zijn ontworpen met manual loop-shaping. Nominale stabiliteit en performance kunnen worden gegarandeerd. Om robuuste performance te krijgen wordt er gain-scheduling van de slipregeling toegepast. De resulterende bandbreedte is tussen 8-10 [Hz] voor zowel de ratio en slip regellussen. Omdat de slipdynamica niet goed gedefinieerd is voor lage snelheden, wordt de slipregeling gedeeltelijk uitgeschakeld onder 2 [km/h].
Zowel het simulatiemodel als de experimentele opstelling laten zeer goede resultaten zien met betrekking tot verstoringonderdrukking en volggedrag. Koppelverstoringen tot 100 [Nm] op de secundaire as van de variator worden binnen 0.2 [sec] onderdrukt

voor alle CVT ratio's. De ratio volgfout is zeer klein in vergelijking met conventionele CVT systemen.
Experimentele evaluatie van de Empact CVT op de testopstelling toont aan dat het gemiddelde verbruikte actuatievermogen op de FTP72 cyclus 155 [W] bedraagt. Op deze cyclus verbruikt een conventioneel hydraulisch geactueerde CVT meer dan 400 [W] gemiddeld. Een efficiëntie van 90 [%] wordt bij deze cyclus gehaald. De evaluatie van de Empact CVT in de Audi A3 2.0 FSI toont gelijkwaardige resultaten. In totaal is er een efficiëntie verbetering van 10 [%] gerealiseerd met de Empact CVT in vergelijking met een hydraulisch geactueerde CVT van vergelijkbare grootte.

Dankwoord

De meeste promovendi vinden dit het makkelijkste van promoveren, maar hoe kun je van je hele promotie, voor mij bijna vijf jaar, iedereen bedanken die je geholpen en gesteund heeft? Zoals iedere promotie kende ook deze een aantal moeilijke, maar gelukkig veel meer leuke periodes. Daaronder vielen natuurlijk alle 'zaken'reizen die ik heb mogen maken. Ik begin het bedanken dan ook met de laatste regel van de aftiteling die ik bij iedere film van deze reizen gebruikte: "Maarten, bedankt!"
Ik kreeg de kans om te promoveren, omdat Maarten Steinbuch mij die heeft gegeven. Het begin was een moeilijke periode voor mij, omdat m'n afstuderen getekend was door het verlies van m'n moeder. Maar ik werd door Maarten's enthousiasme over de streep getrokken en dat enthousiasme heeft me tot het laatst geholpen.
Samen met Bram en Koen ben ik aan dit project begonnen, drie totaal verschillende personen. Ik denk dat we juist door deze verschillen veel van en over elkaar hebben geleerd. In ieder geval hebben we veel steun aan elkaar gehad en nog meer plezier tijdens ruim vier jaar samenwerking. Bedankt hiervoor!
Het project werd gecoördineerd door Bram Veenhuizen. In het begin heeft hij ons een leidraad gegeven, waardoor we gericht onderzoek konden doen. Dat was in dit project, met een vooraf onderschatte omvang, ook wel nodig. Ik wil Bram vooral bedanken, omdat hij altijd geïnteresseerd was in de vooruitgang van het onderzoek en mij daardoor altijd heeft weten te motiveren.
Aan het begin van het project was ook de eerste keer dat Frans Veldpaus erbij betrokken werd. Ik had het geluk dat hij de rol als co-promotor ging vervullen. Helaas was dit slechts voor korte duur, omdat hij met pensioen ging. Gelukkig betekent het pensioen voor Frans niet alleen thuis luieren en heb ik ook bij het tot stand komen van dit proefschrift van zijn kennis en kritische blik gebruik mogen maken. Frans, hartelijk bedankt hiervoor.
De tweede co-promotor, Bas Vroemen, was zelf net klaar met promoveren. Zijn kennis en de ervaring met een soortgelijke promotie was zo vers, dat hij mij hier veel mee heeft kunnen ondersteunen. Ook wil ik hem bedanken voor het kritisch

reviewen van mijn publicaties.
Met alleen bovenstaande geleerde mensen kom je er in zo'n project natuurlijk niet, je hebt ook nog hándige slimme mensen nodig. Vooral bij het realiseren van een prototype transmissie in een auto. Gelukkig hadden wij een aantal van deze mensen rondlopen. Ik wil Toon van Gils bedanken voor alles wat hij uit het niets heeft kunnen realiseren, Wietse Loor voor alles waar een stekker aan zat en Erwin Meinders voor alles wat je van hem verwachtte. Gelukkig was die verwachting niet altijd de kortste weg naar teleurstelling.
Tevens wil ik mijn afstudeerders Jos Meesters, Luuk Peeters en Sjoerd Simons bedanken voor de medewerking die ik van hen heb gehad. Volgens mij vonden zij de samenwerking net zo leuk en leerzaam als ik, want ze zijn er alle drie ruim een jaar mee bezig geweest.
Verder kun je je promotie natuurlijk niet doorstaan zonder goede collega's. Ik denk dat we dat in de kelder van Whoog wel goed geregeld hebben. Zonder de vele namen te noemen wil ik iedereen bedanken waar ik regelmatig koffie mee gedronken heb, geluncht heb, een biertje (of sherry) mee gedronken heb, of zelfs een leuk reisje mee ondernomen heb.
Ook al leek het er de afgelopen maanden niet meer op, er was ook nog een leven buiten het promoveren. Ik wil mijn vrienden bedanken voor de nodige afleiding die zij mij daarin gaven en mijn familie voor alle liefde en steun die ik van hen heb gekregen, en dan wil ik speciaal noemen mijn nichtje en neefjes Romy, Robin en Luco en mijn allerliefste vriendin Marjolein.

Tim

Curriculum Vitae

Tim Klaassen was born in 1977 in Nieuw-Bergen, The Netherlands. He received his Master of Science (MSc) degree in Mechanical Engineering from Eindhoven University of Technology (TU/e) in March 2002. During his MSc project he studied the motion control of industrial printers at Stork Digital Imaging, Boxmeer, The Netherlands. In April 2002 he started his PhD project at Eindhoven University of Technology. In this project he has been working on the dynamics and control of an electromechanically actuated metal V-belt CVT, the Empact CVT. From August 2006 he is working within the Research & Development department of Océ Technologies B.V., Venlo, The Netherlands.